SPONTANEOUS RAMAN AND COHERENT ANTI-STOKES RAMAN SPECTROSCOPY OF INFRARED MULTIPHOTON EXCITED MOLECULES

A thesis presented

by

Kuei-Hsien Chen

to

The Division of Applied Sciences

in partial fullfillment of the requirements

for the degree of
Doctor of Philosophy
in the subject of
Applied Physics

Harvard University
Cambridge, Massachusetts
September, 1989

To Taiwan, my beloved homeland!

ACKNOWLEDGMENTS

Without the scientific, technical, and moral supports of many other people this thesis as well as a wonderful graduate study at Harvard would be impossible.

First and foremost, I owe an enormous debt to my thesis advisor, Professor Eric Mazur. Under his supervision I have learned to appreciate and enjoy fundamental research. His patience in teaching and enthusiasm about science always inspired me to explore for the truth .

I would like to thank Professor Nicolaas Bloembergen for the enlightening discussions that usually brought me to a much clearer view of my research. His lectures in Electrodynamics and Modern Optics equipped me with the ability and confidence for my research.

A special thanks goes to Dr. Cheng-Zai Lü for the wonderful time during our collaboration. We did most of the measurements and analysis together. The most important lesson he has taught me is to employ sincerity and rigorousness in scientific research. It has been a pleasure to collaborate with Professor Mary Shultz. Her theoretical contribution to the understanding of our experimental results was invaluable.

Other members in the Harvard QEMP group have contributed greatly to my study: Dr. Maarten Buijs always gave candid advice, Jyhpyng Wang did the spontaneous Raman experiments with me, Doo-Soo Chung helped solve the toughest mathematical problems, Peter Saeta the Mac expert, Juan-Kai Wang took good care of all the documentation, Kai-Yee Lee always kept the group happy, and Jay Goldman helped me in my thesis writing.

I will always remember Joe Bell and Paulin Mitchel. They were always there when I needed help. Especially Joe's cheerful attitude was better that any advice when I was lost in the dark of research.

Special thanks to Michael Kong, who has taken good care of my 79 Subaru. He gave me a fuel injector which turned out to be a key to the supersonic molecular beam machine in the laboratory.

The love from my neighbors at Eliot Street, Somerville was indispensable during the past five years. My landlady Margaret Waller taught me how to drive and from A to Z about maintaining a house *free*! Mrs. Jardim, Mr. and Mrs. Griffin, and the Borges family all have made the life at Harvard bearable.

My wife Li-Chyong deserves my deepest appreciation. It is she who accompanied me through all the adversities. Let me not forget my daughter Cynthia, who brought us all joy in the past three years. Finally, it is my parents, who work barefoot in Taiwan, who encouraged me and made what I am.

ABSTRACT

This thesis is a study of infrared multiphoton excitation using spontaneous and coherent anti-Stokes Raman spectroscopy. The spontaneous Raman measurements provide information on the intramolecular vibrational energy distribution over the different modes. This information is complemented by the CARS measurements which make it possible to perform state-specific studies of the vibrational and rotational distribution.

For SF_6, the time-resolved spontaneous Raman measurements show complete equilibration of energy from the pump mode to other vibrational modes. In contrast, for smaller molecules such as CF_2Cl_2, a nonthermal energy distribution is observed after excitation. These measurements therefore disprove the general belief that the intramolecular energy distribution in infrared multiphoton molecules is always in equilibrium.

The CARS measurements on bulk OCS provide values for the anharmonicities and for the energy transfer rates between modes. In addition the spectra show a very fast relaxation of the vibrational energy within the ν_2 mode. For SO_2, the CARS measurements show that it is the ν_1 symmetric stretching mode and not the overtone excitation of the ν_2 bending mode that is pumped by the CO_2 laser. Moreover, it is shown that the hot bands of SO_2 have been incorrectly assigned up to now. Corrected values for the anharmonicities are given.

In the second half of the thesis, a pulsed supersonic molecular beam is added to the infrared multiphoton excitation study. Combined with the state-specific CARS technique,

the collisionless and internally cooled molecules in the beam open the door to a more detailed study of the excitation process.

Pure rotational CARS is used to study the change in rotational distribution of ethylene due to infrared excitation in the beam. The appearance of rotational holes reveal which rotational states are pumped by the CO_2 laser. For OCS the evolution of the overtone population into a thermal distribution is studied, providing a value for the intramode relaxation rate.

Finally, the study of SF_6 in the supersonic beam sheds new light on the energy distribution in SF_6 after infrared multiphoton excitation. It is shown that the two-ensemble population distribution observed by other investigators after infrared multiphoton excitation involves a considerable amount of collisional relaxation.

TABLE OF CONTENTS

LIST OF FIGURES

CHAPTER 1

INTRODUCTION

1.1 Laser chemistry

The invention of the laser has created many new opportunities for scientific research in the past two decades, in particular in the field of laser spectroscopy. Due to the narrow linewidth of lasers it is possible to perform high resolution spectroscopy and obtain more detailed information about atoms and molecules. The high intensity of lasers also contributed to the development of nonlinear optical techniques, which further improve the signal-to-noise ratio and spectral resolution by many orders of magnitude.

This thesis deals with infrared multiple-photon excitation of molecules,[1,2,3,4,5] which relates to the interaction of molecular vibrations with strong infrared lasers. While the phenomenon of infrared multiple-photon excitation was discovered almost twenty years ago, the details of the excitation mechanism are still not completely clear.

In 1971 Isenor *et al.* discovered a fast dissociation process after nanosecond pulse CO_2 laser excitation.[6] Although it was not clear at that time what role collisional heating and laser induced breakdown played in this experiment, it has now been well established

that collisionless infrared multiphoton excitation is a universal phenomenon for polyatomic molecules.

The discovery by Ambartzumian *et al.*[7] and Lyman *et al.*[8] that infrared laser induced unimolecular dissociation can be isotope selective gave tremendous impetus to the study of infrared multiphoton excitation. The selectivity of infrared excitation and the success of laser isotope separation motivated both physicists and chemists to further explore intramolecular selectivity, a process that could make possible laser controlled chemical reactions and 'bond-selective' chemical synthesis.

So far, experiments aimed at achieving intramolecular selectivity by infrared excitation have not been successful. This is because the energy deposited in the pumped vibrational mode is rapidly distributed among other vibrational modes due to the coupling between modes and the high density of rotational and vibrational states at high excitation. In fact, results of infrared multiphoton dissociation experiments suggest that the distribution of energy is completely statistical after dissociation leading to a complete loss of selectivity.[4] Studies of the intramolecular vibrational energy relaxation show that relaxation processes take place on a subpicosecond time scale.[9] Since the dissociation time for molecules above the dissociation limit can be longer than the intramolecular vibrational relaxation time, bond-selective dissociation may not happen even if it were possible to excite molecules on a femtosecond time scale. So, while intermolecular selectivity, *e.g.* isotope separation, is achievable, it is unlikely that intramolecular selectivity by infrared multiphoton excitation will be realized.[10]

Notwithstanding this, the understanding of the mechanism of infrared multiple excitation remains limited mostly to qualitative models. More quantitative experimental data are required to further the understanding of intramolecular processes. This thesis reports on time-resolved Raman and coherent anti-Stokes Raman experiments on infrared

multiphoton excited molecules in a supersonic molecular jet. The results lead to new insights into the dynamics of the excitation and relaxation processes.

1.2 Infrared multiphoton excitation and dissociation

Vibrational electric dipole transitions typically fall in the range of infrared radiation from 100 to 4000 cm^{-1}. To calculate the coherent excitation of a vibrational degree of freedom by monochromatic infrared radiation, one can as a first step approximate the molecular vibration by a simple harmonic oscillator. This harmonic model leads to a Poisson distribution over the vibrational degrees of freedom.

Let v be the vibrational quantum number, ω_o the eigenenergy of the harmonic oscillator, and ω the laser frequency. If the oscillator is initially at $v = 0$ at $t = 0$, it will at time t reach an average excitation

$$\langle v(t) \rangle = \left(\frac{\omega_R}{\omega - \omega_o} \right)^2 sin^2 \frac{1}{2}(\omega - \omega_o)t, \tag{1-1}$$

with the Rabi frequency $\omega_R = \frac{1}{\hbar} |\mu| \, |E|$, where μ the electric dipole moment and E the electric field. Thus, at resonance the oscillator will reach an average excitation of $\langle v(t_p) \rangle = \frac{1}{4} (\omega_R t_p)^2$ after a laser pulse of duration t_p. Typically, for a pulse of 100 ns, and $\omega_R \approx 0.1$ cm^{-1}, this yields an excitation of $v = 250$ which is far beyond the dissociation threshold of most molecules.

The simple harmonic approximation fails because it neglects the anharmonicity of the molecular vibrations. A more realistic representation of the vibrational energy of a polyatomic molecule with vibrational degrees of freedom or modes v_1, v_2, v_3,…, is given by

$$E(v_1,v_2,v_{3,\ ...}) = (v_1+\frac{g_1}{2})\,\omega_1 + (v_2+\frac{g_2}{2})\,\omega_2 + (v_3+\frac{g_3}{2})\,\omega_3 + ...$$

$$+ x_{11}(v_1+\frac{g_1}{2})^2 + x_{22}(v_2+\frac{g_2}{2})^2 + x_{33}(v_3+\frac{g_3}{2})^2 + ... \qquad (1\text{-}2)$$

$$+ x_{12}(v_1+\frac{g_1}{2})(v_2+\frac{g_2}{2}) + x_{13}(v_1+\frac{g_1}{2})(v_3+\frac{g_3}{2}) + x_{23}(v_2+\frac{g_2}{2})(v_3+\frac{g_3}{2})$$

$$+ \text{vibrational angular momentum terms} + \text{Coriolis splitting terms...}\ ,$$

where the energy is given in wavenumbers (cm^{-1}), and where v_i is the vibrational quantum number of the v_i mode, ω_i the vibrational energy of the v_i mode, g_i the degeneracy of the v_i mode, x_{ii} the anharmonicity, and x_{ij} the cross-anharmonicity. Thus, the energy for the transition from the (v_1=0) to the (v_1=1) state can be expressed as

$$\Delta E_{(1,v_2,v_{3,\ ...})\rightarrow(0,v_2,v_{3,\ ...})} = E(v_1{=}1,v_2,v_{3,\ ...}) - E(v_1{=}0,v_2,v_{3,\ ...})\ . \qquad (1\text{-}3)$$

If all other modes are in the ground state, one obtains

$$\Delta E_{(1,0,0,\ ...)\rightarrow(0,0,0,\ ...)} = E(v_1{=}1,0,0_{,\ ...}) - E(v_1{=}0,0,0_{,\ ...})$$

$$= \omega_1 + x_{11}(1+g_1) + x_{12}\frac{g_2}{2} + x_{13}\frac{g_3}{2}\ . \qquad (1\text{-}4)$$

Similarly, one has

$$\Delta E_{(2,0,0,\ ...)\rightarrow(1,0,0,\ ...)} = \omega_1 + x_{11}(3+g_1) + x_{12}\frac{g_2}{2} + x_{13}\frac{g_3}{2}$$

$$= \Delta E_{(1,0,0,\ ...)\rightarrow(0,0,0,\ ...)} + 2\,x_{11}\ . \qquad (1\text{-}5)$$

Notice that there is an energy difference of $2x_{11}$ between the first two transitions because of the anharmonicity of the mode.

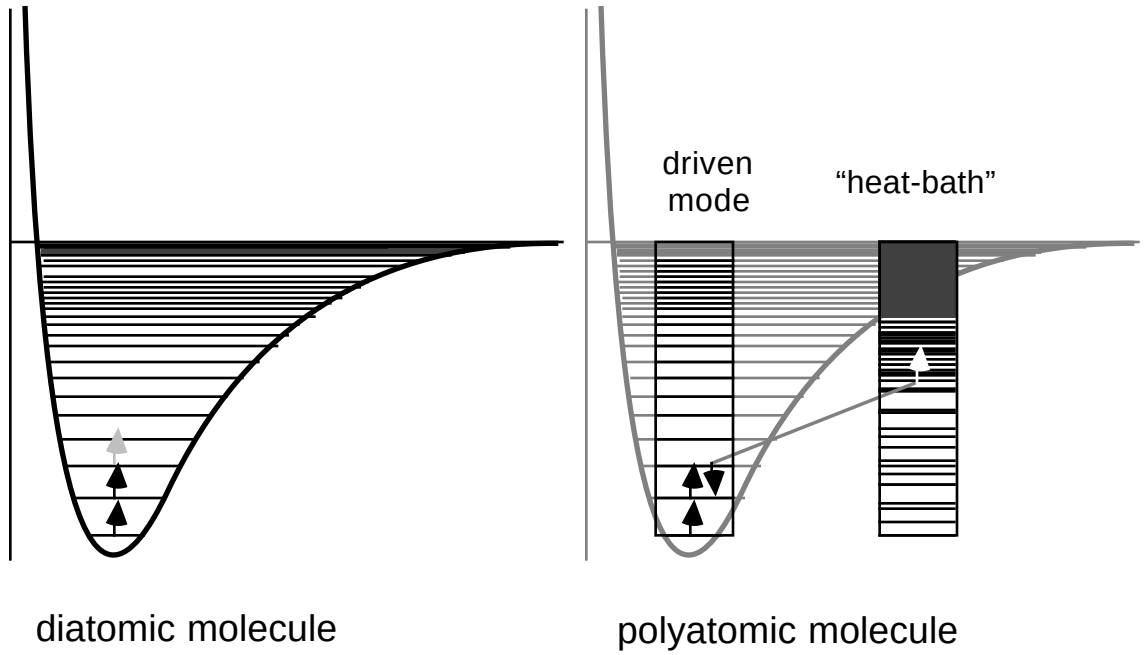

Fig. 1.1. Infrared multiphoton excitation of diatomic molecules is impossible due to the anharmonicity of the vibrational modes. In polyatomic molecules, modes which are not in resonance with the CO_2 laser can also participate in the infrared multiphoton excitation process through intermode coupling.

For $v_1 = v$ the excitation energy is

$$\Delta E_{(v+1,0,0,\ldots)\rightarrow(v,0,0,\ldots)} = \Delta E_{(1,0,0,\ldots)\rightarrow(0,0,0,\ldots)} + 2\,x_{11}\,v \quad . \tag{1-6}$$

Notice the linear relation between the anharmonic shift $2x_{11}v$ and the vibrational quantum number v. Equations (1-5) and (1-6) show that the anharmonicity will bring the vibration out of resonance with the field after excitation to the first excited state. Figure 1.1a illustrates this for diatomic molecules, which have only one vibrational degree of freedom.

Table 1.1 shows a number of mechanisms that can help overcome the anharmonic shift. For example, for a high radiation field intensity, power broadening of the transition occurs. This broadening is equal to the Rabi frequency and can be expressed as[11]

$$\omega_R = \frac{(\mu E)}{\hbar}$$

$$= \frac{(\mu_{0,1} E)}{\hbar}\sqrt{v+1}\,, \qquad (1\text{-}7)$$

where $\mu_{0,1}$ is the electric dipole moment of the $0 \rightarrow 1$ transition. As one can see the power broadening is proportional to $\sqrt{v+1}$ while, as we have seen in (1-6), the anharmonic shift increases linearly with v. In practice therefore power broadening can only compensate the anharmonic shift for the first few steps.

The anharmonic shift can also be compensated for by simultaneous rotational transitions of the molecules. For linear molecules, which have only one rotational degree of freedom, the vibrational and rotational quantum numbers v and J must satisfy the selection rules $\Delta v = \pm 1$ and $\Delta J = 0, \pm 1$, respectively. This gives rise to the P (ΔJ=-1), Q (ΔJ=0), and R-branch (ΔJ=+1) in the vibrational spectrum of the molecule. In addition to the change in vibrational energy, the transition energy has to be corrected for the rotational energy changes. For a molecule with rotational constant B, this rotational correction is $-2JB$, 0, and $2(J+1)B$ for the P, Q, and R-branch respectively. So, if the anharmonicity $2x_{11}$ is close to $-2JB$ the rotational transition can compensate the anharmonic shift for the first three steps by a succession of P, Q and R transitions. The molecule first undergoes a P transition with $\omega = \omega_o - 2JB$ (ω is the laser frequency; ω_o the eigenfrequency of the oscillator), then a Q transition with $\omega = \omega_o + 2x_{11}$, and then an R transition with $\omega = \omega_o + 2JB + 4x_{11}$. Note that each of these transition remains resonant with the laser because $2x_{11} = -2JB$.

Collisions also play an important role in infrared multiphoton excitation. First of all, collisional broadening of the transition can compensate the energy mismatch and assist the excitation. Second, if a rotational hole is created in the rotational spectrum during the excitation, it can be refilled by collisions provided that the collisional relaxation of the rotations is faster than the excitation. If this happens the pumped rotational levels will not be depleted and effectively more rotational levels can contribute to the excitation. So even for transitions in the tail of the rotational spectrum which involve rotational states with a very small population, strong absorption can occur due to this collisional hole-filling effect.

On the other hand, collisions also cause a relaxation of the final excited state which in turn modifies the energy distribution and makes interpretation more difficult. Therefore, it is in general of great importance to achieve so-called collisionless conditions in the study of infrared multiphoton excitation.

TYPE	ORIGIN	LINE WIDTH	MAGNITUDE
Natural line width	Spontaneous decay of the excited state	$\frac{1}{2\pi\tau}$ τ = natural lifetime	10^5~10^7 Hz (atom) 10~10^3 Hz (molecule)
Doppler broadening	Doppler effect due to thermal motion	$k v_D = \nu \frac{v_D}{c}$ v_D = FWHM of the velocity distribution ν = transition frequency c = speed of light	10^8 ~ 10^{10} Hz
Power broadening	Saturation effect from high intensity laser beam	$\frac{\mu E}{\hbar}$ = Rabi frequency μ = transition dipole moment E = laser field strength	~ 10^4 Hz for 1 mW/cm^2
Collision broadening	Collision between molecules	$\frac{1}{\pi\tau_{coll}}$	~ 10^7 Hz at 1 Torr
Line width of a CO_2 laser	Combination of the above effects in laser cavity		$\approx$ 0.01 cm^{-1} $\approx$ 10^8 Hz

TABLE 1.1. List of various line broadening mechanisms of importance for infrared multiphoton excitation.

1.3 The quasicontinuum model

Despite all the possible mechanisms that can compensate for the anharmonicity of a vibrational mode within a molecule, infrared multiphoton dissociation has never been observed for diatomic molecules. For polyatomic molecules, which have more than one vibrational mode, the situation is quite different. When one mode is resonant with an incident infrared laser field, the other modes can form a so-called 'heat-bath.' The coupling between the driven mode and the modes in the heat-bath induces cross-anharmonic shifts of the energy levels and Fermi resonances.[12] Fermi resonances shift the energy levels which may cause new accidental resonances with the laser frequency. In addition Fermi resonances mix the states in the driven mode with states in other modes, causing a rapid energy transfer between these modes. In this case energy is rapidly removed from the driven mode and further excitation can occur. Obviously the laser field then no longer pumps a single driven mode and loss of selectivity occurs.

The effects of mode coupling are particularly important as the energy in the driven mode increases, since the density of states grows rapidly with increasing quantum number. This is clearly visible in Fig. 1.2; for the ν_3 mode of SF_6 the Whitten-Rabinovitch estimate[13] of the density of states increases by about six orders of magnitude as the molecule is excited from the ground state to $v = 5$. These considerations have led to the formulation of the quasicontinuum model,[14] which postulates that the resonance condition is automatically satisfied because of the high-density of states, and that the process is mainly an incoherent step-wise excitation.

According to the quasicontinuum model, the excitation scheme can be explained as progressing through three different regions of excitation (see Fig. 1.3). In region I, just above the ground state, the molecule undergoes selective coherent excitation between the

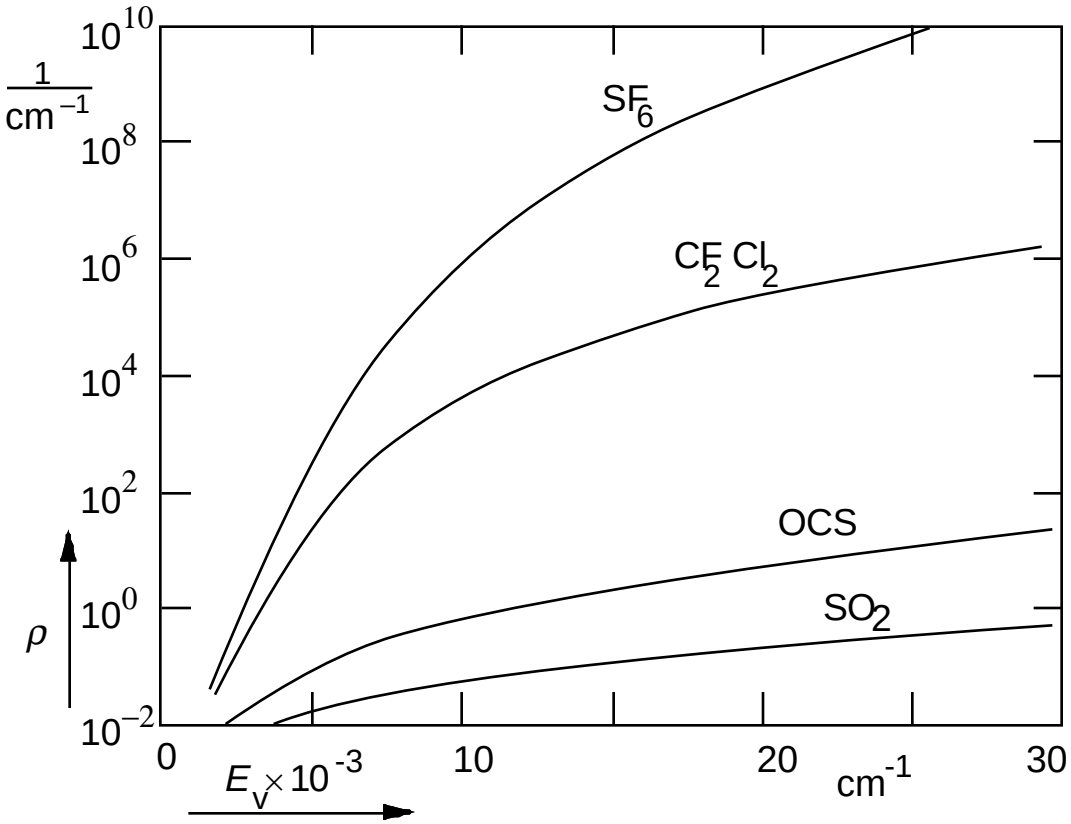

Fig. 1.2. Whitten-Rabinovitch calculation of the density of states of SF_6, CF_2Cl_2, SO_2, and OCS.

(discrete) levels of the driven mode. The excitation proceeds in the same way as in diatomic molecules; true multiphoton processes, rotational compensation and power broadening help overcome the anharmonicities in this low lying discrete region. Since the excitation is mostly coherent in this region, a strong intensity dependence and a high frequency selectivity are to be expected. If molecules do not have a resonant pathway to higher excited states in this region they remain trapped near the ground state, in which case the excitation stops. This is frequently referred to as the bottleneck effect.[15]

In region II, the quasicontinuum, the density of states is so high that the transition rate can be determined by Fermi's golden rule.[16] More specifically, when

$$\hbar\rho(E) \gg \frac{1}{K} \gg T_2 , \tag{1-8}$$

where $\rho(E)$ is the density of states, K the transition rate, and T_2 the intramolecular relaxation time, the transition rate depends linearly on the density of final states and is constant in time. Thus, the excitation through the quasicontinuum can be described by a rate equation

$$\frac{dP_n}{dt} = K_n^a I P_{n-1} + K_n^e I P_{n+1} - (K_{n-1}^a + K_{n+1}^a) I P_n \tag{1-9}$$

where P_n is the probability that the molecule is in the nth excited state, I the laser intensity, K_n^a the absorption coefficient, and K_n^e the stimulated emission coefficient. The intensity can be factored out of the right hand side of Eq. (1.9) from which it follows that the probability P_n is a function of the *fluence* $\phi = \int I(t)dt$ (incident energy per unit area). Therefore, once the molecule is excited into region II, it will undergo resonant step-wise incoherent excitation and the fluence, not the intensity, of the laser determines the excitation through the quasicontinuum.

Finally, when the excitation energy exceeds the dissociation energy E_d of the molecule, $E > E_d$, the molecules reach a true continuum (region III). Molecules in this region need not dissociate instantaneously. If the excitation rate exceeds the dissociation rate, the molecules can continue to be excited above the dissociation limit, E_d. The dissociation rate, however, increases rapidly with increasing excess energy $E–E_d$, and the dissociation rate eventually catches up with the excitation rate. Since the excitation rate is

proportional to the laser intensity (see 1-9), the excess energy depends on the intensity of the laser. After dissociation, this excess energy ends up in the dissociation fragments.

Molecules excited above the dissociation limit will dissociate into fragments that contain the excess energy $E–E_d$. Typically molecules may dissociate via a number of different dissociation channels. It has been reported[4] that the excitation energy in the molecule is completely randomized and statistically distributed among the internal degrees of freedom before or during the dissociation process, in agreement with statistical descriptions of unimolecular dissociation. A well-known example of such a description is the RRKM theory,[13] which assumes equal probability for every accessible state.

The quasicontinuum model provides a qualitative understanding of infrared multiphoton excitation and confirms a number of experimental observations. In particular, since the density of states is lowest for small molecules, region I is expected to play a more important role for small (three to six atom) molecules than for larger ones, where region II extends much closer to the ground level. Indeed, it has been experimentally found that infrared multiphoton excitation is mostly intensity dependent for small molecules and more fluence dependent for large molecules.17

According to the quasicontinuum model the intermolecular selectivity of the excitation is determined by what happens in region I, where coherent excitation occurs, while the intramolecular selectivity depends on the incoherent processes in region II. Despite the insights provided by the quasicontinuum model and statistical unimolecular dissociation theories, it is still not possible to quantitatively describe the dynamics of the infrared multiphoton excitation in region I and region II and many experimental observations remain only partially explained.

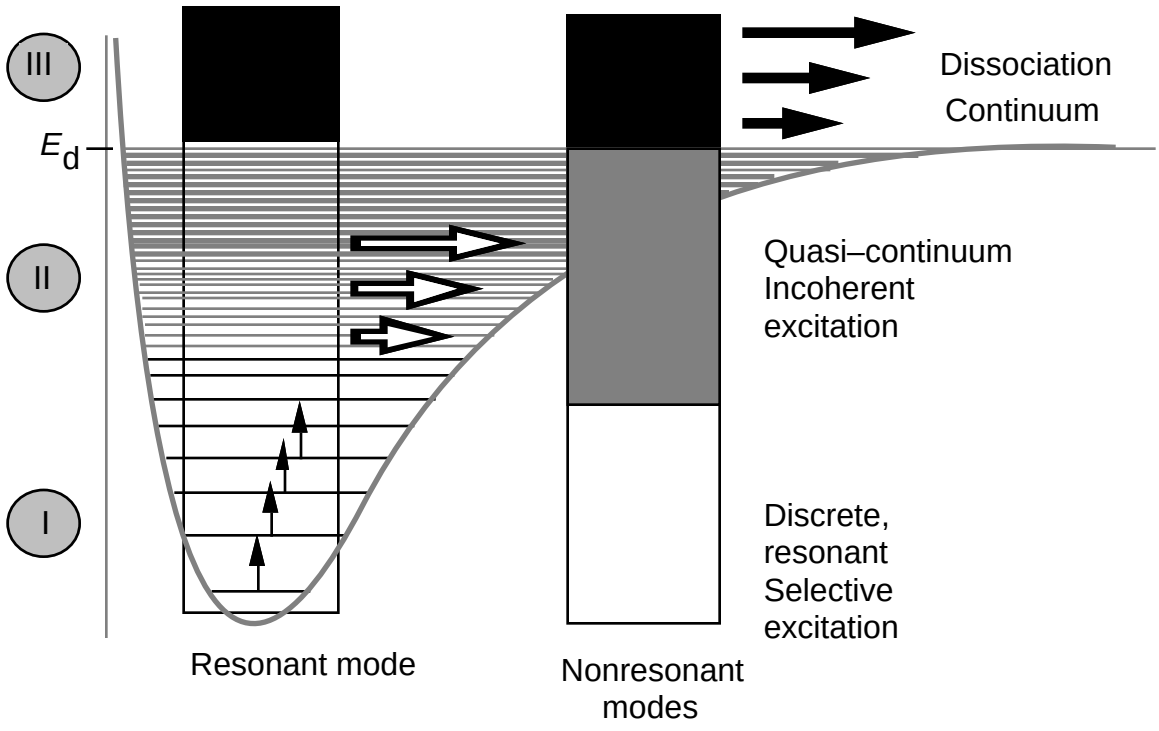

Fig. 1.3. The three regions of infrared multiphoton excitation of polyatomic molecules. Region I is the discrete region where selectivity occurs. Region II is the *Quasicontinuum* region, where step-wise incoherent excitation occurs. The Continuum is indicated as region III, where unimolecular dissociation proceeds.

1.4 Experimental techniques for studying of vibrationally excited molecules

Many different experimental techniques have been used to study infrared multiphoton excitation and dissociation. In the experiment by Isenor and Richardson,[6] fluorescence from SiF_4 fragments was observed after CO_2 laser irradiation. Using a similar technique and temporally resolving the fluorescence signal, Isenor *et al.*[18] and

Letokhov *et al.*[19] found that the fluorescence signal contained two components; an instantaneous and a delayed component, suggesting that dissociation could take place under collisionless conditions.

In contrast to the bulk experiments described above, experiments performed in molecular beams allow one to study infrared multiphoton excitation and dissociation under more ideal collisionless condition. Lee and co-workers,[20] for example, measured the angular and translational energy distributions of dissociation fragments in a molecular beam using a mass spectrometer, and reported a statistical energy distribution consistent with RRKM theory. In other experiments the laser induced fluorescence from dissociation fragments was measured to determine the internal energy distribution of the fragments.[21,22,23]

Another widely used technique to determine the energy absorbed during infrared multiphoton excitation is the photo-acoustic technique.[17,24] Via *V-T* relaxation vibrationally excited molecules will release their energy to translational degrees of freedom and generate acoustic waves which can be picked up with a microphone. If one assumes that the acoustic signal is linearly proportional to the energy absorbed, this technique provides a simple and generally applicable way to study infrared multiphoton excitation. For small molecules, a bottleneck effect and strong intensity dependence were found.

The bottleneck effect was further investigated by Kwok *et al.*[25] using infrared pulses of fixed fluence but varying pulse duration. For SF_6, for fluences below 1 J/cm^2, there is a factor of 30 difference in excitation between pulses of 150 ps and 120 ns. For higher laser fluences the difference decreases as the fluence increases. This result supports the coherent excitation picture in the discrete region.

Time resolved pump-probe experiments make it possible to study the dynamics of the excitation and relaxation processes. The simplest scheme employs a CO_2 laser pulse to excite the molecules, and a second temporally delayed pulse to probe the absorption

spectrum of the excited molecules.[26] For 30 ps CO_2 laser pulses tuned to the ν_3 mode of SF_6 it was found that the intramolecular energy relaxation time is less than 30-ps and that the collisional relaxation time of the vibrational energy in that mode is 13 ns Torr. Because this experiment was limited to a small number of discrete CO_2 laser lines, the information obtained was limited. More detailed information was later obtained by infrared-double-resonance (IRDR). In addition, wth a tunable narrow band diode laser high resolution spectroscopy can be performed.[27]

A complementary technique for IRDR is Raman spectroscopy. Spontaneous Raman scattering for instance, was used to probe the vibrational distribution.[28,29] Using time-resolved spontaneous Raman scattering Bagratashvili *et al.* reported the formation of two vibrational ensembles after infrared multiphoton excitation;[28] one consisting of 'cold' molecules bottlenecked in the lower discrete levels, and one of 'hot' molecules excited into the quasicontinuum. Raman probing has the advantage of making a large number of vibrational modes easily accessible and offering high temporal resolution. On the other hand, the inherently low signal levels of spontaneous Raman scattering limits the applicability of this technique. Subsequent studies involving stimulated Raman spectroscopy[30] and coherent anti-Stokes Raman spectroscopy[31,32] overcome the low signal level problem and offer a higher spectral resolution.

1.5 Inter- and intramolecular vibrational relaxation

If excited molecules do not reach the dissociation threshold, the vibrational energy stored in the molecules will relax to other degrees of freedom. There are two major relaxation processes: inter- and intramolecular relaxation. The intermolecular relaxation is caused by collisions between the molecules. Energy can be transferred from one vibrational mode to another, or from vibrational modes to translational and rotational modes

(these are called *VV*, *VT* and *VR* relaxation, respectively). Because of coupling between vibrational modes, relaxation of vibrational energy from one mode to another within a single molecule can also take place under collisionless conditions. This intramolecular relaxation plays an important role in bond-selective chemistry; if the duration of the infrared pulse is longer than the intramolecular relaxation time, the energy deposited in the molecule will randomize before bond-selective dissociation occurs.

Intermolecular relaxation can be reduced by decreasing the sample gas pressure or the duration of the excitation pulse. When the infrared pulse duration, τ_p, is shorter than the mean free collision time, τ_c, the experiment is frequently called '*collisionless.*' In general, however, this may be misleading since the actual time between excitation and the detection of a signal can be much longer than τ_p. For example, in an infrared multiphoton dissociation experiment, the average dissociation lifetime can be much longer than τ_c, so that even if the excitation is collisionless, collisional effects may still dominate the dissociation process. To verify the role of collisions in an experiment, it is therefore necessary to establish a linear relation between the excitation or dissociation yield and the sample pressure.

Collisional effects can be reduced effectively in a molecular beam system. In addition to reducing the number of collisions, a supersonic beam also lowers the temperature of the sample molecules, in particular for the translational and rotational degrees of freedom. Thus supersonic molecular beams provide a narrower initial distribution of the rotational and vibrational degrees of freedom, and therefore simplify the analysis of infrared multiphoton excitation and relaxation processes.

1.6 Objective of this work

In this thesis both spontaneous and coherent anti-Stokes Raman spectroscopy are applied to study infrared multiphoton excited molecules. The goal of the study is to provide a better understanding of the infrared multiphoton excitation and relaxation processes. More specifically, the focus of this thesis is on the spectral properties of infrared multiphoton excited molecules in regions I and II, and on the dynamics of the vibrational energy transfer in these regions.

With a pulsed supersonic beam, better control of the collisions and a narrower distribution of the rotational levels becomes possible. The combination of CARS and a pulsed supersonic beam enhances the study of infrared multiphoton excitation. Analysis of the experimental data obtained leads to detailed information on the role of collisions during the excitation, the spectra of molecules at high excitation, and the energy distribution after infrared multiphoton excitation.

The following chapter reviews the theoretical framework of Raman scattering. Chapter three reports the experimental results of spontaneous Raman scattering studies of infrared multiphoton excited molecules. In chapter four results of coherent anti-Stokes Raman experiments are discussed. Chapter five discusses theoretical and technical aspects of supersonic molecular jets. Experimental results obtained in a supersonic jet are presented in chapter six. Differences between the results in the bulk and results in the supersonic jet are discussed. Finally, chapter seven concludes this thesis with a summary of the results obtained.

References

1 V.N. Bagratashvili, V.S. Letokhov, A.A. Makarov, E.A. Ryabov, *Multiphoton Infrared Laser Photophysics and Photochemistry* (Harwood Academic Publishers, New York, 1985)

2 D.S. King, *Dynamics of the Excited State*, Ed. K.P. Lawley (Wiley, New York, 1982)

3 W. Fuss and K.L. Kompa, *Prog. Quant. Electr.* **7**, 117 (1981)

4 P.A. Schulz, Aa. S Sudbø, D.J. Krajnovitch, H.S. Kwok, Y.R. Shen, and Y.T. Lee, *Ann. Rev. Phys. Chem.* **30**, 379 (1979)

5 C. D. Cantrell, S. M. Freund, J. L. Lyman, *Laser Handbook*, Vol. 3, Ed. M.L. Stitch (North-Holland, Amsterdam, 1979)

6 N.R. Isenor, M.C. Richardson, *Appl. Phys. Lett.* **18**, 224 (1971)

7 R.V. Ambartzumian, V.S. Letokhov, E.A. Ryabov, and N.V. Chekalin, *JETP Lett.*, **22**, 34 (1975);

R.V. Ambartzumian, Yu.A. Gorokhov, V.S. Letokhov, and G.N. Makarov, *JETP Lett.*, **22**, 34 (1975)

8 J.L. Lyman, R.J. Jensen, J. Rink, C.P. Robinson, S.D. Rockwood, *Appl. Phys. Lett.*, **27**, 87 (1975)

9 M.J. Rosker, M. Dantus, and A.H. Zewail, J. Chem. Phys., ***89***, 6113 (1988)

10 N. Bloembergen and A.H. Zewail, *J. Phys. Chem.*, **88**, 5459 (1984)

11 Y.R. Shen, *The Principles of Nonlinear Optics* (John Wiley & Sons, New York, 1984)

12 F. Albert Cotton, *Chemical Applications of Group Theory*, (Wiley-Interscience, New York, 1971)

13 P.J. Robinson and K.A. Holbrook, *Unimolecular Reactions* (Wiley, New York 1972)

14 N. Bloembergen and E. Yablonovitch, Physics Today **5**, 23 (1978)

15 V.S. Letokhov, *Nonlinear Laser Chemistry*, Springer, New York (1982)

16 Gordon Baym, *Lecture on Quantum Mechanics*, (Benjamin, Massachusetts 1981)

17 J.G. Black, P. Kolodner, M.J. Sshultz, E. Yablonovitch, and N. Bloembergen, *Phys. Rev.* A **19**, 704 (1979)

18 N.R. Isenor, V. Merchant, R.S. Hallsworth and M.C. Richardson, *Can. J. Phys.* **51**, 1281 (1973)

19 R.V. Ambatzumian, N.V. Chekalin, V.S. Doljikov, V.S. Letokhov, and E.A. Ryabov, *Chem. Phys. Lett.* **25**, 515 (1974)

20 Y.T. Lee, Y.R. Shen, *Phys. Today*, November, 52 (1980)

21 J.D. Campbell, M.H. Yu, and C. Wittig, *Appl. Phys. Lett.*, **32**, 413 (1978)

22 D.S. Frankel and T.J. Manuccia, *Chem. Phys. Lett.*, **54**, 451 (1978)

23 J.C. Stephenson, and D.S. King, *J. Chem. Phys.*, **69**, 1458 (1978)

24 V.N. Bagratashvili, I.N. Knyazev, V.S. Letokhov, and V.V. Lobko, *Opt. Commun.* **18**, 525 (1976)

25 H.S. Kwok, E. Yablonovitch, *Phys. Rev. Lett.*, **41**, 745 (1978)

26 H.S. Hwok, Ph.D. Thesis, Harvard, 1978

27 C.C. Jensen, T.G. Anderson, C. Reiser, and J.I. Steinfeld, *J. Chem. Phys.*, **71**, 3648 (1979)

28 V.N. Bagratashvili, Yu.G. Vainer, V.S. Doljikov, V.S. Letokhov, A.A. Makarov, L.P. Malyavkin, E.A. Ryabov, and E.G. Sil'kis, *Opt. Lett*. **6**, 148 (1981)

29 Jyhpyng Wang, Kuei-Hsien Chen and Eric Mazur, *Phys. Rev*. A, **34**, 5 (1986) 3892

30 P. Esherick, A.J. Grimly, and A. Owyoung, *Chem. Phys.*, **73**, 271 (1982)

31 S.S. Alimpiev, A.A. Mokhnatyuk, S.M. Nikiforov, A.M. Prokhorov, B.G. Sartakov, V.V. Smirnov, and V.I. Fabelinskii, *Laser Spectroscopy VIII*, W.Persson and S. Svanberg Eds. (Springer Series in optical sciences, 1987), p. 229

32 K.H. Chen, C.Z. Lü, L. Avilés, E Mazur, N. Bloembergen, and M.J. Shultz, *J. Chem. Phys.* **91**, 1462 (1989)

CHAPTER 2

RAMAN SPECTROSCOPY

2.1 Introduction

Since the discovery of the Raman effect in 1928,[1] Raman scattering has become a widely used technique to study molecular structure and dynamics.[2] The advent of lasers increased the applicability of Raman spectroscopy because of the high intensity, directionality, and monochromaticity of the new light sources. Recent developments in nonlinear optics further provided powerful related spectroscopic techniques such as stimulated Raman spectroscopy, coherent anti-Stokes Raman spectroscopy, and higher order Raman effects.[3] In this chapter, the basic theory of spontaneous and coherent anti-Stokes Raman spectroscopy are reviewed and an outline of the basic experimental techniques is given.

2.2 Spontaneous Raman scattering

Consider the interaction of a radiation field with the vibrational mode of a molecule. Both radiation field and physical system will be treated quantum mechanically.[4] The total Hamiltonian of the system can then be expressed as

$$H = H_{\mathrm{v}} + H_{\mathrm{em}} + H_{\mathrm{int}} , \tag{2.1}$$

where H_{v} represents the kinetic and the potential energy of the vibrational mode, H_{em} the electric and the magnetic energy of the radiation field, and H_{int} the interaction between the molecular system and the field. The vibrational Hamiltonian can be expressed as

$$H_{\mathrm{v}} = \frac{1}{2\mathrm{m}} (\boldsymbol{p}^2 + \omega_{\mathrm{o}}^2 \boldsymbol{q}^2) , \tag{2.2}$$

where ω_{o} is the vibrational frequency of the mode and $\boldsymbol{q}$ the normal mode amplitude. In the simple harmonic approximation, $\boldsymbol{q}$ can be expressed in terms of the creation and annihilation operators of molecular vibration, $\boldsymbol{b}^{\dagger}$ and $\boldsymbol{b}$, as

$$\boldsymbol{q} = (\hbar / 8\pi^2 \mu \nu_R)^{1/2} [\boldsymbol{b}^{\dagger} + \boldsymbol{b}], \tag{2.3}$$

with μ the electric dipole moment and $\nu_R = \omega_{\mathrm{o}}/2\pi$. Therefore the Hamiltonian of the molecular system becomes

$$H_{\mathrm{v}} = \hbar \omega_{\mathrm{o}} (\boldsymbol{b}^{\dagger}\boldsymbol{b} + 1/2) . \tag{2.4}$$

Similarly, we can use creation and annihilation operators for the field, $\boldsymbol{a}^{\dagger}$ and $\boldsymbol{a}$, and quantize the radiation field by

$$\boldsymbol{E}_{\lambda} = \sqrt{\frac{2\pi h \nu_L}{\varepsilon V}} \sum_{k_\lambda} \boldsymbol{e}_{k_\lambda} i [a_{k_\lambda}{}^{\dagger} - a_{k_\lambda}] , \tag{2.5}$$

where $\mathbf{e}_{k_\lambda}$ is the unit vector representing the polarization of the field and V the interaction volume. The field Hamiltonian then becomes

$$H_{\text{em}} = \sum_{k_\lambda} \hbar\omega_{k_\lambda} \left(\boldsymbol{a}_{k_\lambda}^{\dagger}\boldsymbol{a}_{k_\lambda} + 1/2\right) , \tag{2.6}$$

An expression for the interaction Hamiltonian can be obtained from first order perturbation theory using the electric dipole approximation.[4] For Raman scattering, one considers the polarization $\boldsymbol{P} = \alpha\boldsymbol{\cdot E}$ induced by the field and expands the molecular polarizability α as a function of the local coordinate $\boldsymbol{q}$

$$\alpha = \alpha_o + \left(\frac{\partial\alpha}{\partial\boldsymbol{q}}\right)_o \boldsymbol{q} + \ldots . \tag{2.7}$$

The interaction Hamiltonian between the polarization and the field is then

$$\begin{aligned} H_{\text{int}} &= \boldsymbol{E}\cdot\alpha\cdot\boldsymbol{E} \\ &= \boldsymbol{E}\cdot\alpha_o\cdot\boldsymbol{E} + \left(\frac{\partial\alpha}{\partial\boldsymbol{q}}\right)_o \boldsymbol{E}\cdot\boldsymbol{q}\cdot\boldsymbol{E} + \ldots . \end{aligned} \tag{2.8}$$

The first term represents Rayleigh scattering, the second term first order Raman scattering. Higher order terms are neglected in this discussion. For spontaneous Raman scattering, one considers only the first order Raman term in (2.8) and takes into account the laser field, plus the Stokes and anti-Stokes fields $\boldsymbol{E} = \boldsymbol{E}_L + \boldsymbol{E}_S + \boldsymbol{E}_{AS}$. Substituting Eqs. (2.3) and (2.5) in (2.8), one obtains

$$H_{int} \sim \left(\frac{\partial \alpha}{\partial \boldsymbol{q}}\right)_o \sum_{k_S\, k_L} \sqrt{\frac{2\omega_L \omega_S}{\omega_o}}\, (\boldsymbol{e}_{k_L} \cdot \boldsymbol{e}_{k_S})(\boldsymbol{a}^{\dagger}_{k_S} \boldsymbol{b}^{\dagger} \boldsymbol{a}_{k_L} + \boldsymbol{a}_{k_S} \boldsymbol{b}\, \boldsymbol{a}^{\dagger}_{k_L})\, \delta(\boldsymbol{k}_L - \boldsymbol{k}_S - \boldsymbol{k}_v)$$

$$+ \left(\frac{\partial \alpha}{\partial \boldsymbol{q}}\right)_o \sum_{k_{AS}\, k_L} \sqrt{\frac{2\omega_L \omega_{AS}}{\omega_o}}\, (\boldsymbol{e}_{k_L} \cdot \boldsymbol{e}_{k_{AS}})(\boldsymbol{a}^{\dagger}_{k_{AS}} \boldsymbol{b} \boldsymbol{a}_{k_L} + \boldsymbol{a}_{k_{AS}} \boldsymbol{b}^{\dagger}\, \boldsymbol{a}^{\dagger}_{k_L})\, \delta(\boldsymbol{k}_L - \boldsymbol{k}_{AS} + \boldsymbol{k}_v), \quad (2.9)$$

where the subscripts L, S and AS refer to laser, Stokes and anti-Stokes photons, respectively. The delta function comes from the rotating wave approximation.[5] Because of this delta function, only resonant terms that fulfill momentum conservation contribute to the Raman process. The first term in Eq. (2.9) corresponds to the Stokes branch and the second one to the anti-Stokes branch.

According to Fermi's golden rule, the steady state transition rate W can be expressed as:[4]

$$W_{i \to f} = \frac{2\pi}{\hbar} |\langle f | H_{int} | i \rangle|^2\, \rho(\hbar\omega_f) \quad (2.10)$$

where f represents the final and i the initial state. For the eigenstates $| n_v \rangle$ of the harmonic oscillator one has

$$\boldsymbol{b}^{\dagger} | n_v \rangle = (n_v + 1)^{1/2} | n_v + 1 \rangle , \quad (2.11)$$

and

$$\boldsymbol{b} | n_v \rangle = n_v^{1/2} | n_v - 1 \rangle , \quad (2.12)$$

with n_v the vibrational quantum number corresponding to state $| n_v \rangle$. Equations (2.11) and (2.12) are also valid for the operation of the operator $\boldsymbol{a}$ and $\boldsymbol{a}^{\dagger}$ on the field number state $| n \rangle$.

Applying (2.11) and (2.12) to the matrix element in (2.10), one obtains

$$\langle\ n_S{+}1, n_L{-}1,\ n_v{+}1\ |\boldsymbol{a}^{\dagger}_{k_S}\boldsymbol{b}^{\dagger}\boldsymbol{a}_{k_L}\ |\ n_S, n_L, n_v\ \rangle\ \sim\ ((n_S{+}1)n_L(n_v{+}1))^{1/2}\ , \quad (2.14)$$

and

$$\langle\ n_{AS}{=}1, n_L{-}1,\ n_v{-}1\ |\boldsymbol{a}^{\dagger}_{k_{AS}}\boldsymbol{b}\boldsymbol{a}_{k_L}\ |\ n_{AS}{\approx}0, n_L, n_v\ \rangle\ \sim\ \ ((n_{AS}{+}1)n_L n_v)^{1/2}\ . \quad (2.15)$$

Therefore, the Stokes and the anti-Stokes transition rates can be expressed as

$$W_{n_v \to n_v+1} \sim n_v + 1, \qquad W_{n_v \to n_v-1} \sim n_v\ . \quad (2.16)$$

The linear dependence on the excitation quanta n_v provides an easy way to determine n_v from the Raman signal intensity.

By spectrally resolving the Raman signals from each vibrational level one can obtain the population distributions of the vibrational modes. As described in Eq. (1.2), the anharmonicity causes an energy shift for each excited level in the spectrum. This will appear as as a series of peaks, called the 'hot band' of the vibrational mode. Thus the diagonal-anharmonic shift reveals the population in the probed Raman mode and the cross-anharmonic shift reveals the population of the other modes.

In practice, however, the analysis is complicated because the differences in anharmonicity between different modes can be small, so that different hot bands overlap. Therefore the assignment of the spectra for molecules of more than three vibrational modes requires a high spectral resolution to resolve the individual peaks. For a diatomic molecule there is only one hot band and the anharmonic shift is linearly proportional to the quantum number. Therefore even a poorly resolved spectrum of that band will reflect the energy

distribution in the mode. For polyatomic molecules poorly resolved spectra do not provide much information because the anharmonicity of different modes can vary by a factor of ten.

Still, by spectrally integrating the Raman signals, *i.e.* summing the signals over all different vibrational levels, one can obtain information on the average excitation per molecule in the probed Raman mode. This can be seen by taking the sum over all levels of the product of the transition probability and the population $N(n_v)$ in each level n_v, and substituting (2.16):

$$\begin{aligned} I_S \quad &\sim \sum_{n_v=0}^{\infty} W_{n_v \rightarrow n_v+1} N(n_v) \sim \sum_{n_v=0}^{\infty} (n_v+1)\, N(n_v) \\ &= 1 + \sum_{n_v=0}^{\infty} n_v\, N(n_v) = 1 + \langle n_v \rangle \end{aligned} \tag{2.17}$$

$$\begin{aligned} I_{AS} \quad &\sim \sum_{n_v=0}^{\infty} W_{n_v+1 \rightarrow n_v} N(n_v) \\ &\sim \sum_{n_v=1}^{\infty} n_v N(n_v) = \langle n_v \rangle, \end{aligned}$$

where $N(n_v)$ is the population of level n_v, and $\langle n_v \rangle$ the average vibrational quantum number of the mode. Thus the integrated anti-Stokes intensity of a Raman mode is equal to $\langle n_v \rangle$ to within some proportionality constant A which is referred to the Raman cross section

$$I_{AS} = A \left(\frac{E_R}{h \nu_R} \right) = A \langle n_v \rangle. \tag{2.18}$$

To obtain the quantity $\langle n_v \rangle$, we must eliminate the proportionality constant A. This can be done by normalizing the anti-Stokes signal in (2.18) with the room temperature

Stokes signal of that mode. Without infrared pumping at room temperature $\langle n_v \rangle$ can be obtained from the Boltzmann distribution

$$\langle n_v \rangle_o = \frac{E_R^o}{h\nu_R} = \frac{1}{e^{h\nu_R/kT_o} - 1} , \tag{2.19}$$

with E_R^o the energy of the Raman active mode at room temperature T_o. Since for molecular vibrations $h\nu_R$ is generally much larger than kT at room temperature, $\langle n_v \rangle_o \approx 0$. Therefore the normalized anti-Stokes signal, I_{norm}, will be equal to $\langle n_v \rangle$:

$$I_{norm} \equiv \frac{I_{AS}}{I_R^o} = \frac{A \langle n_v \rangle}{A (1 + \langle n_v \rangle_o)} \approx \langle n_v \rangle . \tag{2.20}$$

By comparing I_{norm} for different vibrational modes, one can thus obtain the distribution of vibrational energy over the different modes of the molecules after infrared excitation.

2.3 Nonlinear Raman spectroscopy

At high incident laser intensities the nonlinear response of the molecules to the field become important.[6] A well-known example is the stimulated Raman effect, which generates a coherent signal several orders of magnitude stronger than the spontaneous Raman signal. In liquids and high pressure gases conversion efficiency of more than 20% is possible. Despite the enormous gain in Raman signal strength, stimulated Raman spectroscopy has been of little use in molecular spectroscopy because of the very high laser intensities required.[6] In practice the application has been limited to only the strongest Raman transitions.

Another nonlinear Raman technique known as coherent anti-Stokes Raman spectroscopy (CARS) has been used to obtain a coherent signal with the strength of a stimulated Raman signal, while retaining the general applicability of spontaneous Raman

spectroscopy. As we shall see coherent anti-Stokes Raman spectroscopy, which has a wide spectral range and high temporal and spectral resolution, is a particularly good technique for studying infrared multiphoton excitation. Consequently, most of the work in this thesis is focussed on the application of coherent anti-Stokes Raman spectroscopy to the study of infrared multiphoton excitation.

The main advantages and disadvantages of CARS relative to spontaneous Raman spectroscopy are listed in Table 2.1. The most important benefit is the large gain in Raman signal in a beam of small divergence and high spectral resolution. A detailed discussion of coherent anti-Stokes Raman spectroscopy and an explanation of its advantages and disadvantages as listed above are given in the next section.

2.4 Coherent anti-Stokes Raman spectroscopy

The theoretical descriptions of coherent anti-Stokes Raman spectroscopy (CARS) in this section follow the conventional notation in Gaussian unit in the literature.[5,9] The wave equation which governs the propagation of optical wave $\boldsymbol{E}(\mathbf{r},t)$ in a medium is

$$\nabla\times\nabla\times\boldsymbol{E}(\mathbf{r},t) + \frac{1}{c^2}\frac{\partial^2}{\partial t^2}\boldsymbol{E}(\mathbf{r},t) = -\frac{4\pi}{c^2}\frac{\partial^2}{\partial t^2}\boldsymbol{P}(\mathbf{r},t)\ . \tag{2.21}$$

According to nonlinear optics theory the polarization $\boldsymbol{P}(\mathbf{r},t)$ includes linear and nonlinear terms,

TABLE 2.1 Comparison of CARS to spontaneous Raman spectroscopy

Advantages of CARS	Disadvantages
1. High signal levels ($10^5 \sim 10^7 \times$ spontaneous Raman signal).	1. Samples must be optically transparent, not easily damaged by high power lasers.
2. High spectral resolution (equal to linewidth of a laser for scanning CARS, or to resolution of the monochromator for multiplex CARS).	2. Signals strongly dependent on laser amplitude, wavelength and alignment stability.
3. Small signal beam divergence makes higher collection efficiency possible ($10^{-4} \times$ spontaneous divergence) This also provides excellent spatial discrimination against luminous background.	3. The nonresonant term limits detection of species of low relative concentration.
4. Elimination of fluorescence problem since $\omega_{CARS} > \omega_{Laser}$.	4. Equipment is more complex than that for spontaneous Raman.
5. Folded BOXCARS geometry[7] eliminates nonresonant signals from windows, and provides higher spatial resolution.	5. Not easily tuned over a wide spectral range as in spontaneous Raman spectroscopy.
6. Multiplex CARS[8] allows single shot measurement which eliminates problems associated with dye laser fluctuations.	6. The $(\Delta N)^2$ dependence of the CARS signal make studies of broad distribution difficult.

$$\boldsymbol{P}(\mathbf{r},t) = \chi^{(1)} \bullet \boldsymbol{E} + \chi^{(2)} \bullet \boldsymbol{E}\,\boldsymbol{E} + \chi^{(3)} \bullet \boldsymbol{E}\,\boldsymbol{E}\,\boldsymbol{E} + \ldots$$

$$= \boldsymbol{P}^{(\mathrm{L})}(\mathbf{r},t) + \boldsymbol{P}^{(\mathrm{NL})}(\mathbf{r},t)\ , \tag{2.22}$$

where $\chi^{(i)}$ is the susceptibility tensor of rank $(i + 1)$. The field can be expressed as

$$\boldsymbol{E}_j(\mathbf{r},t) = \frac{1}{2}\boldsymbol{A}_j(\mathbf{r},t)\ e^{i(\boldsymbol{k}_j \bullet \boldsymbol{r} - \omega_j t)} + \text{ c.c.},$$

where $\boldsymbol{A}(\mathbf{r},t)$ represents the slowly varying amplitude of the field and the index j indicates the jth radiation field . Using the vector equality

$$\nabla \times \nabla \times \boldsymbol{E} \ = \ \nabla\ (\nabla \bullet \boldsymbol{E}\ ) - \ \nabla^2 \boldsymbol{E}\ \ , \tag{2.23}$$

and the fact that all laser beams and the signal generated in this coherent process have small divergence $\nabla \bullet \boldsymbol{E}_j \approx 0$, Eq. (2.21) can be reduced to

$$\nabla^2 \boldsymbol{E}\ (\mathbf{r},t) - \frac{1}{c^2}\frac{\partial^2}{\partial t^2}\boldsymbol{E}(\mathbf{r},t) = \ \frac{4\pi}{c^2}\frac{\partial^2}{\partial t^2}\,\boldsymbol{P}(\mathbf{r},t)\ . \tag{2.24}$$

Substituting $\varepsilon \equiv 1 + 4\pi\chi^{(1)}$ into (2.24), the wave equation can be reduced to

$$\nabla^2 \boldsymbol{E}\ (\mathbf{r},t) + \frac{\omega^2 \varepsilon}{c^2}\,\boldsymbol{E}(\mathbf{r},t) = \ \frac{4\pi\omega^2}{c^2}\,\boldsymbol{P}^{\mathrm{NL}}(\mathbf{r},t)\ . \tag{2.25}$$

If the amplitude $\boldsymbol{A}_j(\mathbf{r},t)$ varies slowly compared with the oscillation of the field, one has

$$\left|\frac{\partial^2}{\partial z^2}\boldsymbol{A}_j(\mathbf{r},t)\right| \ << \left| k_j \frac{\partial}{\partial z}\boldsymbol{A}_j(\mathbf{r},t)\right| . \tag{2.26}$$

By this slowly varying amplitude approximation,[10] the second order differential equation (2.25) reduces to a first order one

$$-2ik_j \frac{\partial}{\partial z}\boldsymbol{A}_j(\mathbf{r},t)\ e^{i\boldsymbol{k}_j\cdot\boldsymbol{r}} = \frac{4\pi\omega_j^2}{c^2}\boldsymbol{P}_j^{\mathrm{NL}}(\mathbf{r},t)\ . \tag{2.27}$$

This equation can be used as a master equation for most nonlinear optical processes.

The energy diagram of coherent anti-Stokes Raman scattering is shown in Fig. 2.1. Since the process involves four laser fields, CARS is basically a four wave mixing process. The nonlinear polarization responsible for CARS is

$$\boldsymbol{P}_{\mathrm{CARS}}^{\mathrm{NL}}(\mathbf{r},t) = \chi_{ijkl}^{(\mathrm{CARS})} \cdot \boldsymbol{E}_j\,\boldsymbol{E}_k\,\boldsymbol{E}_l \tag{2.28}$$

$$= \boldsymbol{e}_{\mathrm{CARS}} \left\{ \chi_{ijkl}^{(\mathrm{CARS})}(-\omega_{\mathrm{CARS}},\ \omega_1,\ -\omega_2,\ \omega_1)\ (\boldsymbol{e}_1\ \boldsymbol{e}_2\ \boldsymbol{e}_1) \cdot \boldsymbol{A}_1\boldsymbol{A}_2^*\boldsymbol{A}_1\ e^{i(2\boldsymbol{k}_1-\boldsymbol{k}_2)\cdot r} \right\}$$

,

where $\chi_{ijkl}^{(\mathrm{CARS})}$ is the nonlinear susceptibility tensor associated with the CARS process.

Equation (2.27) can thus be written as

$$\frac{\partial}{\partial z}\boldsymbol{A}_{\mathrm{CARS}}(\mathbf{r}) = \frac{2\pi i\omega^2{}_{\mathrm{CARS}}}{k_{\mathrm{CARS}}c^2}\ \boldsymbol{e}_{\mathrm{CARS}} \left\{ \chi^{(\mathrm{CARS})} \cdot \boldsymbol{e}_1\ \boldsymbol{e}_2\ \boldsymbol{e}_1 \right\}\ \boldsymbol{A}_1\ \boldsymbol{A}_2{}^*\ \boldsymbol{A}_1\ e^{-i\Delta\boldsymbol{k}\cdot\boldsymbol{r}}, \tag{2.29}$$

where $\Delta\boldsymbol{k} = \boldsymbol{k}_{\mathrm{C}} - 2\boldsymbol{k}_1 + \boldsymbol{k}_2$ is the momentum mismatch. With the appropriate boundary conditions and assuming constant intensity of the ω_1 and $\omega_2$beams, we obtain the CARS amplitude after an interaction length l by integrating z over the interaction length

$$\boldsymbol{A}_{\mathrm{CARS}}(\boldsymbol{l}) = \frac{2\pi\omega^2{}_{\mathrm{CARS}}}{k_{\mathrm{CARS}}\,c^2}\ \boldsymbol{e}_{\mathrm{CARS}}\ \chi^{(\mathrm{CARS})}\ \boldsymbol{A}_1{}^2\ \boldsymbol{A}_2{}^* \frac{(e^{-i\Delta\boldsymbol{k}\cdot l} - 1)}{\Delta k}\ . \tag{2.30}$$

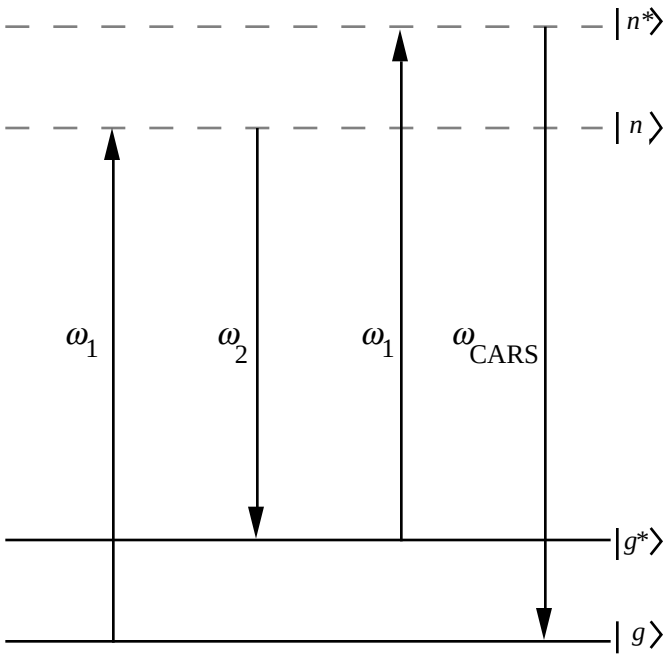

Fig. 2.1 The energy diagram of coherent anti-Stokes Raman spectroscopy. The solid lines represent molecular energy levels and the dashed lines indicate virtual levels.

The time averaged intensity, $I = cn/8\pi\,|\boldsymbol{A}|^2$, of the CARS signal is therefore

$$I_{\mathrm{CARS}}(l) = \frac{256\pi^4\omega^2_{\mathrm{CARS}}}{n_1^2 n_2 n_{\mathrm{CARS}}\, c^4} \left|\chi^{(\mathrm{CARS})}\right|^2 I_1{}^2\, I_2\; l^2 \left(\frac{sin(\Delta k \bullet l/2)-1}{\Delta k l/2}\right)^2, \qquad (2.31)$$

where n_i is the index of refraction at ω_i.

The CARS signal as shown in Eq. (2.31) is proportional to the square of I_1 and linearly proportional to I_2. The signal will be maximum when it satisfies momentum conservation

$$\Delta\boldsymbol{k} = \boldsymbol{k}_{\mathrm{C}} - 2\boldsymbol{k}_1 + \boldsymbol{k}_2 = 0\ , \qquad (2.32)$$

which is the phase matching condition.

Generally the third order nonlinear susceptibility $\chi^{(3)}$ is a fourth rank tensor with 81 elements. The symmetry of the medium, however, greatly reduces the number of independent elements. For an isotropic medium such as a gas, there are only four nonzero elements

$$\chi^{(3)}_{1111}\,,\ \chi^{(3)}_{1122}\,,\ \chi^{(3)}_{1212}\,,\ \text{and}\ \ \chi^{(3)}_{1221}\,,$$

with

$$\chi^{(3)}_{1111} = \chi^{(3)}_{1122} + \chi^{(3)}_{1212} + \chi^{(3)}_{1221}\,. \tag{2.33}$$

Explicit expressions for the remaining three terms can be found in the literature.[11] All of them have three resonant factors in the denominator and are of the following form

$$\chi^{(3)} \sim \frac{N(\rho_{gg}-\rho_{g^*g^*})}{\left\{(\omega_{gg^*}-\omega_1+\omega_2)-i\Gamma^{-1}_{gg^*}\right\}\ \left\{-i(\omega_1-\omega_2)+\Gamma^{-1}_{g^*}\right\}}$$

$$\times\left\{\frac{1}{i(\omega_{gg^*}-\omega_1)+\Gamma^{-1}_{gg^*}}+\frac{1}{i(\omega_{gg^*}-\omega_1)+\Gamma^{-1}_{gg^*}}\right\}\,, \tag{2.34}$$

where $\hbar\omega_{gg^*}$ is the energy difference between the $|g\rangle$ and $|g^*\rangle$ state, $\Gamma^{-1}_{g^*}$ is the relaxation rate of $|g^*\rangle$, and $\Gamma^{-1}_{gg^*}$ is the transverse relaxation rate. In (2.33), Raman type resonances occurs when

$$\omega_{gg^*} = \omega_1 - \omega_2. \tag{2.35}$$

Together with (2.31) the $N(\rho_{gg} - \rho_{g^*g^*})$ dependence in (2.34) indicates that the CARS signal is proportional to the square of the population difference between the $|g\rangle$ and $|g^*\rangle$ states. Therefore the signal will depend quadratically on the density of the sample.

2.5 Practical considerations

For studying gas molecules, colinear CARS is the easiest option. In this case the four beams overlap in the same direction. Since $n_1 \approx n_2 \approx n_{\mathrm{CARS}} \approx 1$, the resonance condition in Eq. (2.35) automatically implies that the phasematching condition in Eq. (2.31) is satisfied. Colinear phasematching can vastly simplify the initial alignment. However, the difficulties in rejecting the incident laser beams from the CARS signal, poor spatial resolution due to the long interaction length, and the presence of nonresonance background from the cell windows can cause serious problems.

One way to solve these problems is to use a folded 'BOXCARS' phase matching geometry as shown in Fig. 2.2. The two beams of frequency ω_1 are in one plane, and a second beam at ω_2 and the CARS signal at ω_C are in another plane perpendicular to the first plane.

The folded BOXCARS scheme has many advantages over the colinear scheme:

1) High spatial resolution because only the small region at the intersection of the three input beams contributes to the CARS signal.
2) There is no problem in separating the signal from the input laser beams.
3) Non-resonant CARS from the cell widows is absent because the laser beams do not overlap at the windows.

On the other hand the alignment of the laser beams is more difficult for the BOXCARS scheme. It is usually done by carefully aligning the three input beams parallel to one another and focusing them through a single lens into the sample. The spacing of the parallel

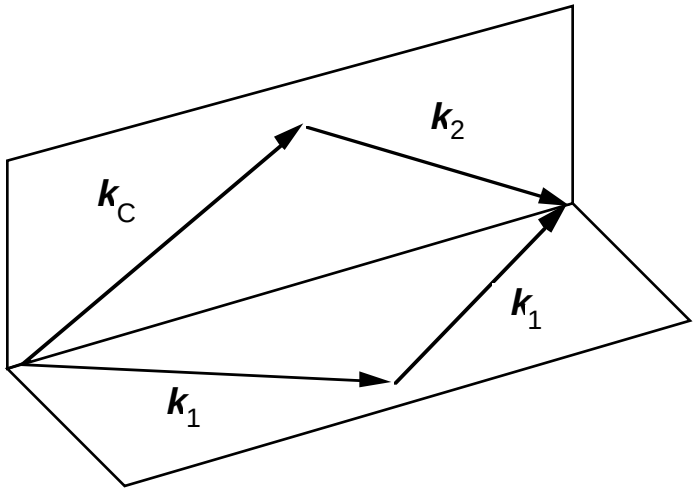

Fig. 2.2 Phase matching diagram of folded BOXCARS. Two laser beams at frequency ω_1 are in one plane and the other two beams at frequencies ω_2 and ω_C are in another plane perpendicular to the first plane.

beams must be adjusted so as to obtain phase matching at the interaction region. The simplest way to achieve this is to calculate the spacing of the beams and to align the parallel beams through four corresponding holes cut in a small card. The configuration of the beams in the interaction region is shown in Fig. 2.3.

Spectra can be obtained in two ways. One is to fix the frequency of one laser (ω_1) while scanning the frequency of the other laser (ω_2). The spectral resolution is then determined by the bandwidths of the lasers, and can be as small as 0.001 cm^{-1}. Since the spectra must be obtained over a large number of shots, an inherent problem associated with this method is the large shot-to-shot fluctuations of the CARS signal due to the fluctuations of the input laser beams. A second method, that does not suffer from this problem, is to replace the tunable scanning laser at ω_2 by a broad band dye laser.

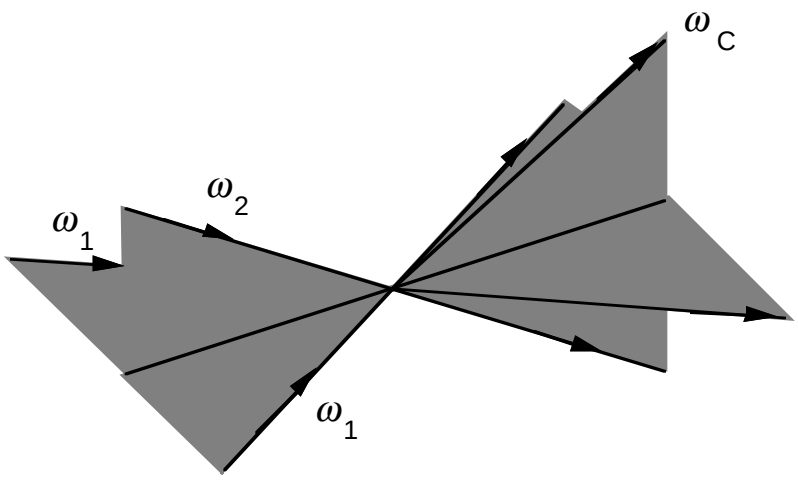

Fig. 2.3 Folded BOXCARS configuration. Since the generated CARS signal is in a different direction from the input laser beams, this configuration provides excellent spatial rejection of the input laser background.

The spectral width of the laser must be sufficient to cover the spectral region of interest. In this method, called multiplex CARS, the CARS spectrum is generated in a single laser shot as shown in Fig. 2.4.. The trade-off is that one needs a spectrograph to resolve the signal and thus the spectral resolution is determined by that of the spectrograph. For a momochromator this typically means a resolution on the order of 0.1 cm^{-1}. With a detector array the entire CARS spectrum can be measured in a single shot, avoiding the problems associated with laser intensity and spectral fluctuations .

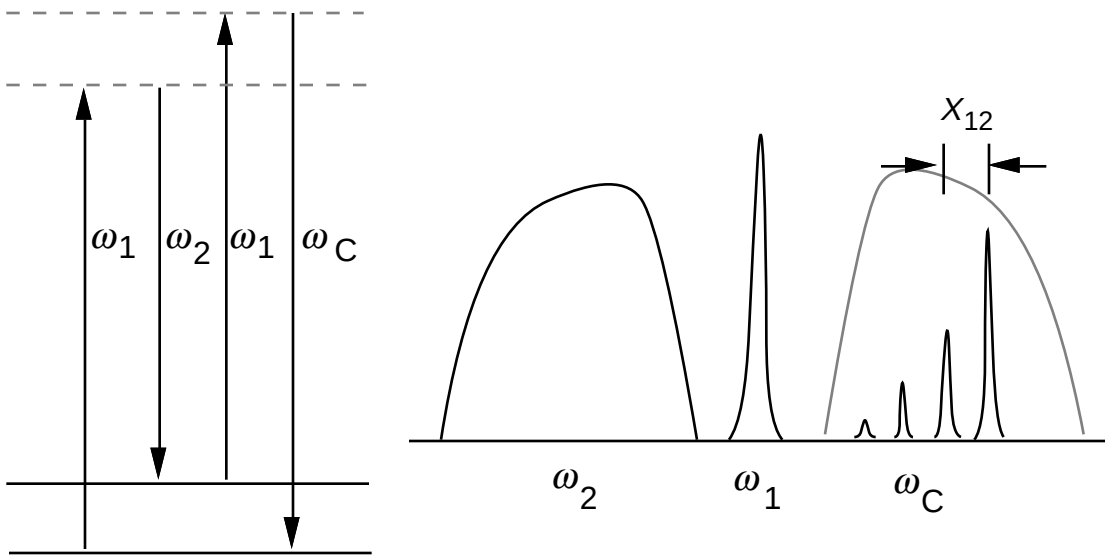

Fig. 2.4 Energy diagram and spectrum of multiplex CARS. The laser at ω_2 laser has a spectral width sufficiently large to cover the entire spectral region of interest. This allows one to obtain the entire CARS spectrum in single laser shot. The figure shows a vibrational spectrum in which the peaks from different levels are separated by a cross-anharmonicity x_{12}.

2.6 Pure rotational CARS

The multiplex CARS scheme described in the previous section provides is well suited to study systems with a Raman shift in the 50 to 3000 cm^{-1} range. This range nicely overlaps with vibrational transitions of molecules. Rotational levels on the other hand, have a Raman shift on the order of one wavenumber. To study such levels with the scheme mentioned above, one would need two lasers with a correspondingly small frequency difference. While this could be achieved with two dye lasers, a small modification of the

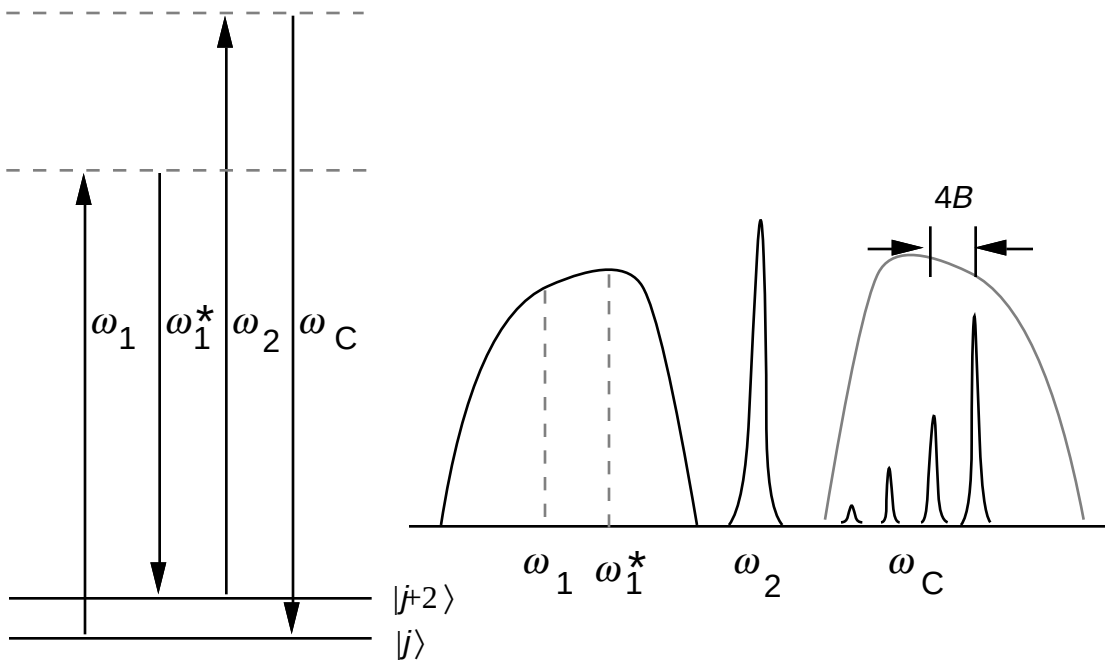

Fig. 2.5 Energy diagram and spectrum of broad band pure rotational CARS. The two pumping lasers at ω_1 and ω_1^* are from a single broadband dye laser. This laser provides pairs of photons with a few wavenumber difference corresponding to the rotational Raman transition. The ω_2 beam is a narrow band laser of any wavelength.

multiplex CARS scheme offers a more convenient method. This method, called pure rotational CARS, is illustrated in Fig. 2.5. Instead of one broadband and two narrowband lasers, this method employs two broadband and one narrowband laser beams. As shown in Fig. 2.5 the rotational transition then selects a set of two frequencies ω_1 and ω_1^* from each of the broadband beams, such that the frequency difference $\omega_1 - \omega_1^*$ equals the frequency of the rotational transition . Since the rotational constants of molecules are small, a dye laser of 60 cm^{-1} bandwidth easily covers the entire rotational spectrum. Note that in this scheme the frequency difference between the two lasers at ω_1 and ω_2 is not determined by any molecular parameters.

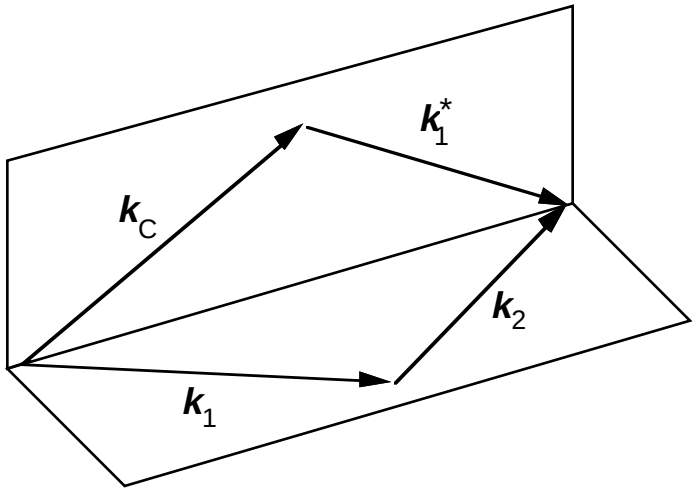

Fig. 2.6 Phase matching diagram of pure rotational CARS.

To fulfill the phase matching condition $k_C = k_1 + k_2 - k_1^*$, the BOXCARS scheme has to be modified as shown in Fig. 2.6 and Fig. 2.7. Both k_1 and k_1^* lasers are derived from a single broadband dye laser, k_2 from a narrowband laser.

This scheme adds a number of advantages to multiplex folded BOXCARS. First, since a photon at any frequency ω_1 within the bandwidth of the broadband laser automatically finds a partner so that $\omega_1 - \omega_1^* = \Delta\omega_{rot}$, *all* photons in the broadband beam are used. This contributes to a stronger CARS signal than in the vibrational scheme where only the resonant frequencies are used. Second, since the frequency difference $\omega_1 - \omega_2$ is arbitrary, one can choose the most efficient dye to improve the signal level. Third, the

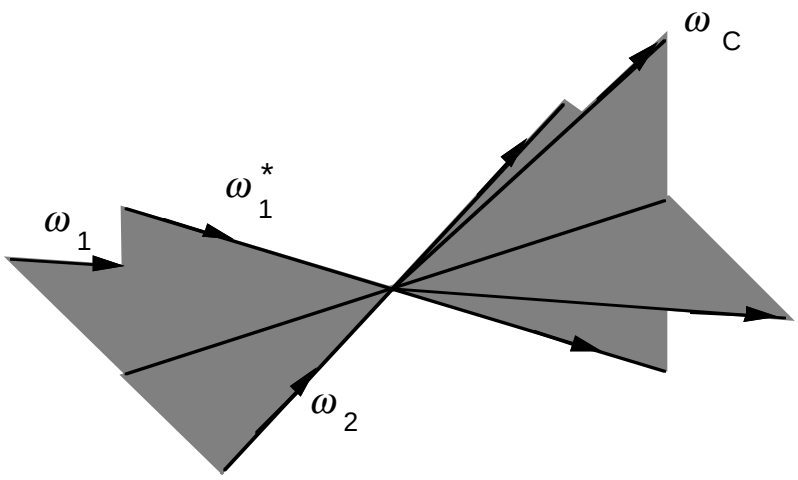

Fig. 2.7 Pure rotational CARS configuration.

alignment is the same for all molecules as long as the rotational Raman spectrum is covered by the broad band dye laser. Once the beams are properly aligned, one can switch from one molecule to another without any change in alignment.

In pure rotational CARS spectra one can easily observe Stokes transtitions in addition to the anti-Stokes transitions (see *e.g.* Fig.6.2). These transitions, which are at the opposite end of the anti-Stokes transitions with respect to the position of the ω_2 laser beam, are referred to as coherent Stokes Raman spectroscopy lines (CSRS). The CSRS spectrum is a mirror image of the CARS spectrum. Since the frequency of these lines is lower than that of the laser beam, fluorescence induced by the probing lasers can cause problems in detecting the CSRS signals. For that reason CARS signals are preferable over CSRS signals.

2.7 Conclusion

In this chapter we reviewed theoretical and experimental aspects of spontaneous and coherent anti-Stokes Raman spectroscopy. As we have seen the normalized and spectrally integrated spontaneous anti-Stokes signal provides information on the average vibrational excitation of the probed Raman mode. The coherent anti-Stokes Raman signals provide high intensity and high resolution spectra, which enables a state-specific study of both the vibrational and rotational distributions. As will be shown in the next few chapters both techniques further the understanding of the dynamics of infrared multiphoton excitation.

References

1 C.V. Raman and K.S. Krishnan, *Nature*, **121**, 501,1928.

2 M.M. Sushchinskii, *Raman Spectra of Molecules and Crystals*, (Isreal Program for Scientific Translations, New York, 1972)

3 A. Penzkofer, A. Laubereau, and W. Kaiser, "*High intensity Raman Interaction*" in *Prog. Quant. Electr.*, **6**, 55 (1979)

4 Gordon Baym, *Lecture on Quantum Mechanics*, (Benjamin, Massachusetts 1981)

5 N. Bloembergen, *Nonlinear Optics*, (Benjamin, New York 1977)

6 W. Keifer and Long, ed., *Non-linear Raman Spectroscopy and Its Chemical Applications*, Proceedings to the NATO Advance Study Institute held at Bad Windsheim, Germany, 1982 (Reidel, Holland, 1982)

7 J.A. Shirley, R.J. Hall, and A.C. Eckbreth, *Opt. Lett.* **5**, 380 (1980)

8 W.B. Roh, P.W. Schreiber, J.P. Taran, *Appl. Phys. Lett.* 29, 174 (1976)

9 M.D. Levenson and Satoru S. Kano *Introduction to Nonlinear Laser Spectroscopy* (Academic Press, 1988 Revised Edition); Y.R. Shen, *The Principles of Nonlinear Optics*, (John Wiley & Sons, 1984)

10 J.A. Armstrong, N. Bloembergen, J. Ducuing, and P.S. Pershen, *Phys. Rev.* **127**, 1918 (1962)

11 N. Bloembergen, H. Lotem, R.T. Lynch Jr., *Indian J. Pure and Appl. Phys.* **16**, 151 (1978)

CHAPTER 3

TIME RESOLVED SPONTANEOUS RAMAN SCATTERING EXPERIMENTS

3.1 Introduction

As discussed in section 2.2, the normalized anti-Stokes Raman signal, I_{norm}, is a good measure of the excitation of the probed Raman-active vibrational mode. From I_{norm} the average quanta $\langle n_v \rangle$ in a vibrational mode is obtained directly. Time-resolved measurements of the Raman spectra thus lead to a better understanding of the dynamics of the infrared multiphoton excitation. This chapter summarizes results obtained using spontaneous Raman scattering to study the vibrational energy distribution after infrared multiphoton excitation of polyatomic molecules. A more detailed description can be found in Refs. 1 and 2.

In the next section the experimental set-up, experimental procedures, and data analysis procedure will be described. The experimental results and their interpretations follow in section 3.3 and 3.4.

3.2 Experimental Setup

A schematic view of the setup is shown in Fig. 3.1. An infrared exciting beam and an ultraviolet probing beam cross inside a scattering cell. By varying the delay between the

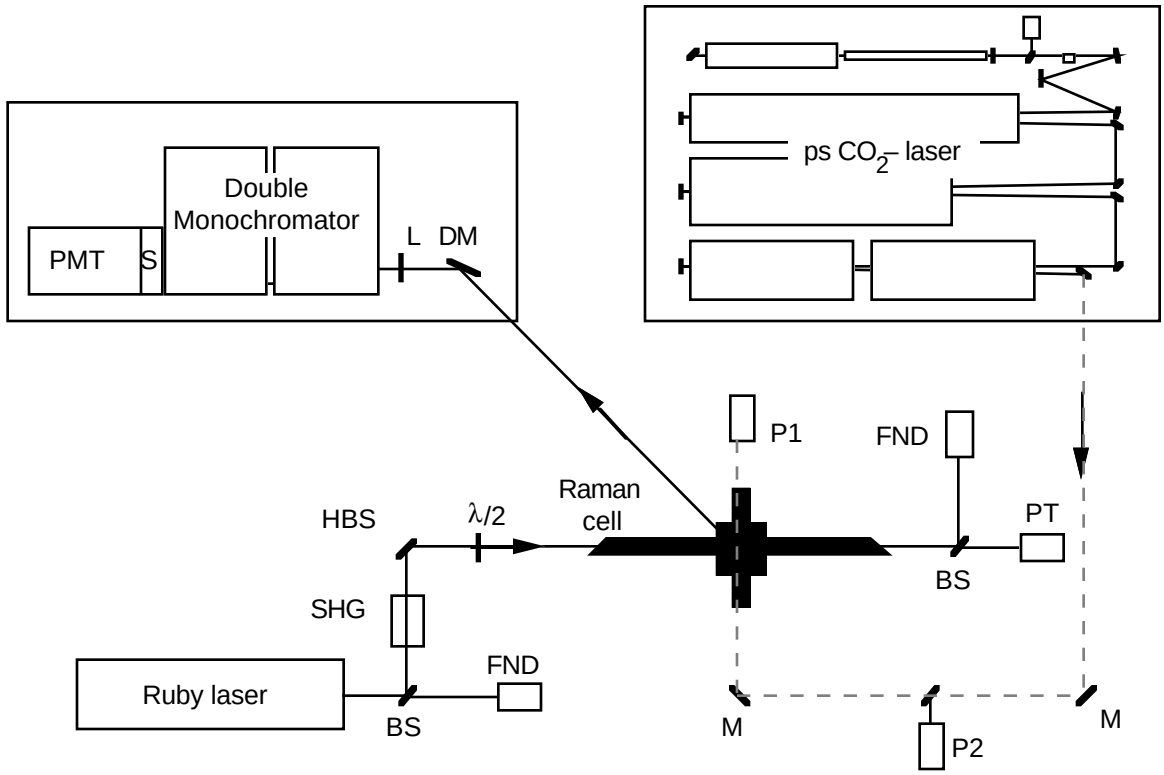

Fig. 3.1 Experimental set-up for the spontaneous Raman scattering study of infrared multiphoton excitation. The dashed line represents the infrared pump beam from the CO_2 laser and the solid line the probe beam from the Ruby laser. BS = beam splitter, SHG = second harmonic generator, HBS = harmonic beam splitter, λ/2 = half wave plate, FND = fast photo-diode, PT = photo-tube, P1, P2 = pyroelectric detector, M = mirror, DM = dichroic mirror, L = quartz lens, S = shutter, PMT = photomultiplier tube.

pump and probe pulse, we can perform time-resolved measurements, allowing the study of the dynamics of the excitation and relaxation process. The spontaneous Raman signal of the molecules studied is detected along the direction perpendicular to the incident beams. The scattering cell consists of two orthogonal arms, that contain a series of black anodized baffles, arranged to trap scattered or diffracted light, see Fig. 3.2. Light scattered in the interaction region is collected over a solid angle of $\pi/16$ sr, and focused onto the entrance slit of a double monochromator of 3-nm resolution. The output from the monochromator is detected by a fast ultraviolet-sensitive photomultiplier.

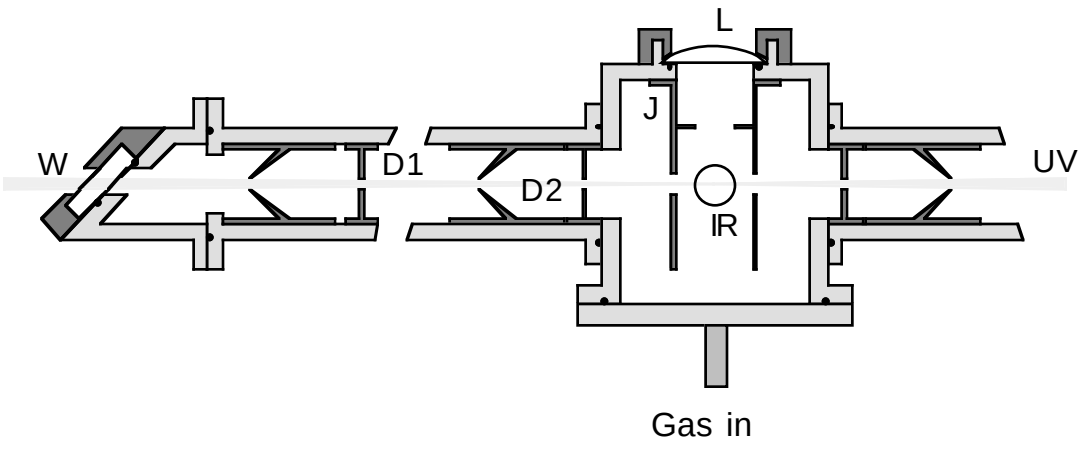

Fig. 3.2. Cross-sectional view of the Raman cell with the window holder rotated by 90° to show the Brewster angle mounting. W = quartz window, D1, D2 = straight and conical baffles, J = stray light jacket, IR = position of IR pump beam, UV = probing UV beam, L = collimating lens.

A short-pulse CO_2 laser system, which generates 30- to 500-ps pulses with an average energy of 100 mJ, is used to generate the infrared pumping pulse.[1] The output

beam is focused into the scattering cell by a cylindrical lens. Depending on the optical arrangement used, the beam waist is 2.2×0.18 mm or 6×0.35 mm.

The probe beam is generated by a Raytheon model SS-420 *Q*-switched ruby laser that is frequency-doubled with a RDA-crystal second harmonic generator. The second harmonic at 347.15 nm is vertically polarized, *i.e.* in the direction of detection. A half-wave plate rotates the polarization by 90^{o} into the plane of the two laser beams to obtain a maximum cross-section for Raman scattering, see Eq. (2.9). The beam is focused into the scattering region, where it crosses the infrared laser beam. The beam waist at the focal point is 500 μm, and the average probing pulse energy is 5 mJ.

A 0.3-Hz pulse generator controls the timing of the lasers and the data-acquisition system. The trigger pulses are optically isolated to prevent feedback of radio-frequency noise from the lasers. The synchronization of lasers and amplifiers is controlled electronically. The accuracy is limited by the 100-ns jitter of the lasers. Since this is inadequate for our measurements, the time-delay between infrared and ultraviolet pulses is measured for each pair of pulses. Two fast detectors provide start and stop pulses for an EG&G model 457 time to pulse-height converter, which measures the time delay between the two laser pulses. Although the resolution of the time to pulse-height converter is better than 100 ps, the time resolution of the setup is limited by the 18-ns duration of the probe beam. The energy of pump and probe pulses are measured by a pyroelectric detector and a phototube, respectively.

For spontaneous Raman measurements, the following signals were recorded: Raman signal intensity, input energy and time-delay of ultraviolet and infrared pulses, ruby laser energy. All signals are collected by a CAMAC and GPIB interface data-acquisition system, which is described in details in Ref. 1.

As we are dealing with small signals, several consistency checks were performed to make sure that no systematic errors occur. It was verified that there is no signal without an

ultraviolet probing pulse, or without gas in the scattering cell, and no anti-Stokes signal for negative time-delay. Reproducibility of the measurements was checked routinely during each measurement and from measurement to measurement.

3.3 SF_6 Results

SF_6 has six vibrational modes as shown in Table 3.1. The triply degenerated ν_3 mode at 965 cm^{-1} is resonant with the 10*P*(20) CO_2 laser line. Spontaneous Raman signals of the spherically symmetric breathing ν_1 mode with a Raman shift of 775 cm^{-1} from the frequency-doubled Ruby laser are obtained to monitor the energy content in this mode.

Mode	k (cm^{-1})	ν (THz)	symmetry	degeneracy	activity
ν_1	775	23.25	A_{1g}	1	Raman (s)
ν_2	644	19.32	E_g	2	Raman (w)
ν_3	965	28.95	F_{1u}	3	infrared
ν_4	617	18.51	F_{1u}	3	infrared
ν_5	524	15.72	F_{2g}	3	Raman (w)
ν_6	363	10.89	F_{2u}	3	inactive

TABLE 3.1 Vibrational modes of SF_6.[3]

3.3.1 Raman Spectrum

Raman spectra of SF_6 with and without infrared excitation are shown in Fig. 3.3. The central peak is due to elastic Rayleigh scattering. At room temperature without infrared

excitation, only about 3% of molecules are in the first excited state. Therefore no anti-Stokes signal is observed. With infrared excitation, both Stokes and anti-Stokes signals

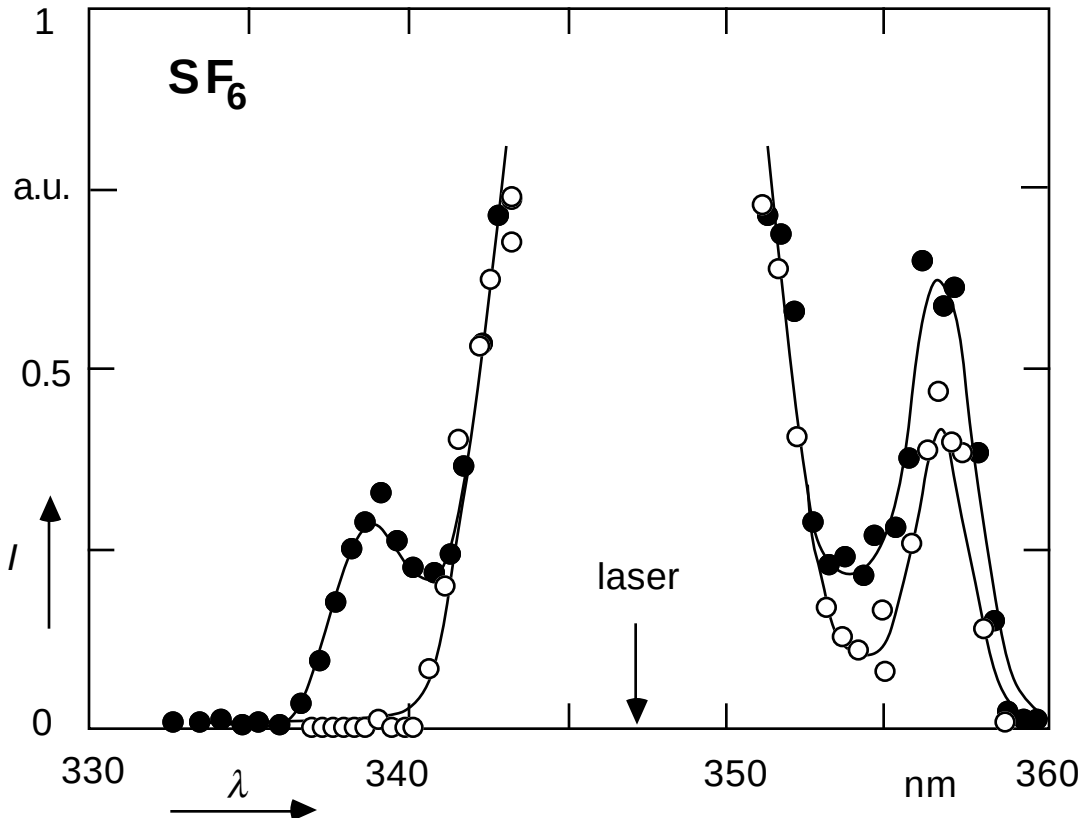

Fig. 3.3. Raman spectrum of SF_6, with (closed symbols) and without (open symbols) infrared multiphoton excitation. Infrared excitation: 10.6 μm P(20) line, 0.5 ns pulse duration, and average fluence 0.6×10^4 J/m^2. The small arrow shows the position of the laser radiation at 347.15 nm.

increase, showing that after pumping the infrared active ν_1 mode the energy distribution of the Raman active ν_3 mode is changed.

As described in Eq. (2.20), the normalized and spectrally integrated anti-Stokes signal represents the number of quanta in the Raman mode. For this reason the rest of

spontaneous Raman data are obtained at fixed frequency with a monochromator slit that covers 3-nm spectral width to integrate the anti-Stokes signals. The anti-Stokes signal is then normalized with the Stokes signal at room temperature to obtain the normalized anti-Stokes signal, I_{norm}. The normalization process is important because it avoids the need to carry out a calibration for every signal monitored.

3.3.2 Time dependence

Figure 3.4 shows the increase of both the normalized Stokes and the normalized anti-Stokes signals as a function of the time delay between the infrared pump and the probe pulse for two infrared pulse durations, 0.5 ns and 15 ns, respectively, at a pressure of 67 Pa and an average infrared fluence of 0.8×10^4 J/m^2. Negative time delay, $t < 0$, means that the molecules are probed before the infrared multiphoton excitation, *i.e.* the molecules are at thermal room temperature equilibrium. Within the 20-ns time resolution of the experiment a collisionless increase of both Stokes and anti-Stokes signals is observed. The increase is consistent with the result obtained in Eq. (2.17), *i.e.* for each pulse duration both Stokes and anti-Stokes signal increase by the same amount. After the initial increase the signals remain constant, even on a time scale on which collisional vibrational energy relaxation starts to play a role (the vibrational relaxation time constant, $\tau_{V\text{-}V}$, is given by $p\tau_{V\text{-}V} \approx 70\,\mu$sPa).[3] Clearly, collisions do not affect the total intensity of the anti-Stokes signal, showing that intramolecular equilibrium is reached on a time scale shorter than the time resolution.

By varying the pressure of the sample gas, the anti-Stokes signal shows a trivial linear dependence on the gas pressure. This ensures that collisions do not contribute to the excitation under these experimental conditions.

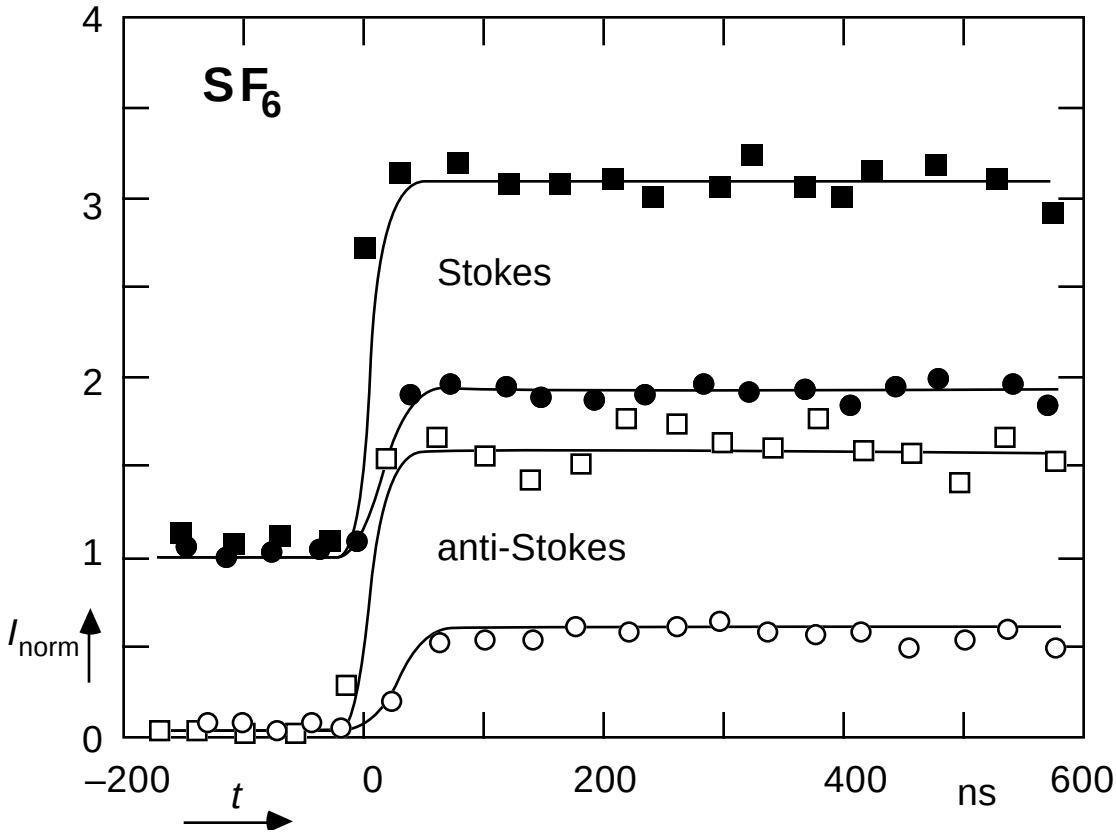

Fig. 3.4. Normalized intensity of Stokes (closed symbols) and anti-Stokes (open symbols) signal as a function of the time delay between pump and probe pulses at a pressure of 67 Pa. Results are shown for two different durations, 0.5 ns (squares) and 15 ns (circles). Infrared excitation at the 10.6 μm P(20) line, with an average fluence of 0.8×10^4 J/m^2.

3.3.3 Fluence dependence

The infrared fluence dependence of the Stokes and anti-Stokes signal is shown in Fig. 3.5 for different pressures and pulse durations. These results were obtained in different runs, each one calibrated individually. The spread in data therefore provides an indication of the absolute accuracy and reproducibility of the experimental data. Figure 3.5

shows that both Stokes and anti-Stokes signals increase by the same amount, in agreement with Eq. (2.20).

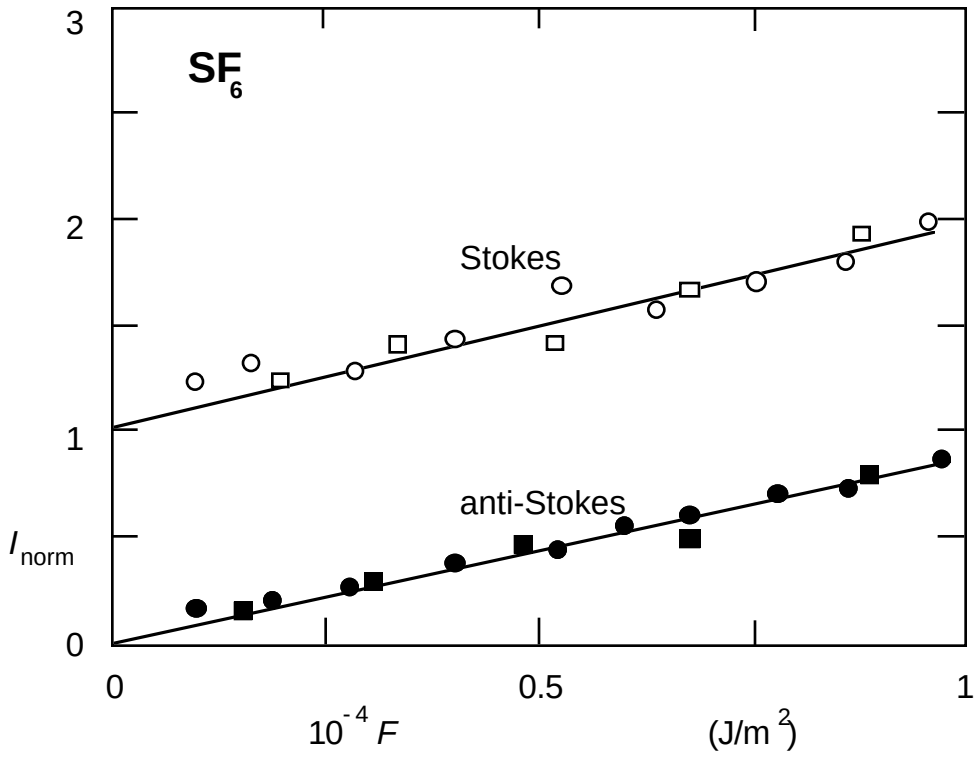

Fig. 3.5. Relative Stokes (open symbols) and anti-Stokes (closed symbols) signal as a function of the infrared pumping fluence at the 10.6 μm P(20) line for 15 ns pulses at two different pressures: p = 27 Pa (squares), and p = 133 Pa (circles)

3.3.4 Discussion

Within the 20 ns time-resolution of the experiment, collisionless increase of the anti-Stokes signal is observed after excitation. Since the Raman signals remain constant (within the 10% experimental accuracy) for 1 μs after infrared multiphoton excitation, this

observation suggests that intramolecular vibrational energy equilibrium is established within the time-resolution of the experiment. If the energy distribution among the different vibrational modes were not in equilibrium, collisions would alter the energy in the Raman active mode, and consequently change the Raman signal intensity.

Further evidence of an intramolecular equilibrium is obtained by comparing the present results with results obtained from photoacoustic measurements.[4] Since the Raman signals are proportional to the energy stored in the Raman active mode, the energy can be obtained from the relative increase in anti-Stokes signal,

$$\begin{aligned} E_{\mathrm{R}} &= h\nu_{\mathrm{R}} \langle n_{\mathrm{v}} \rangle \\ &= h\nu_{\mathrm{R}} I_{\mathrm{norm}} , \end{aligned} \tag{3.1}$$

where I_{norm} is the normalized anti-Stokes signal defined in Eq. (2.20), $\langle n_{\mathrm{v}} \rangle$ the average quantum number, and ν_{R} the vibrational frequency of the Raman mode. If one assumes intramolecular equilibrium among different vibrational modes, the energy distribution of the different modes should correspond to a common temperature. The total increase in vibrational energy of the molecule can thus be calculated from this temperature, and compared to the total absorbed energy, obtained from the photoacoustic measurements. The result of this comparison is shown in Fig. 3.6. The average total energy absorbed per molecule in units of pumping infrared photons is plotted as a function of infrared fluence. The data points are obtained from the current experiments, while the curves show the results of the photoacoustic measurements from Ref. 4. The agreement between the two measurements is remarkable, providing strong evidence for an intramolecular equilibrium.

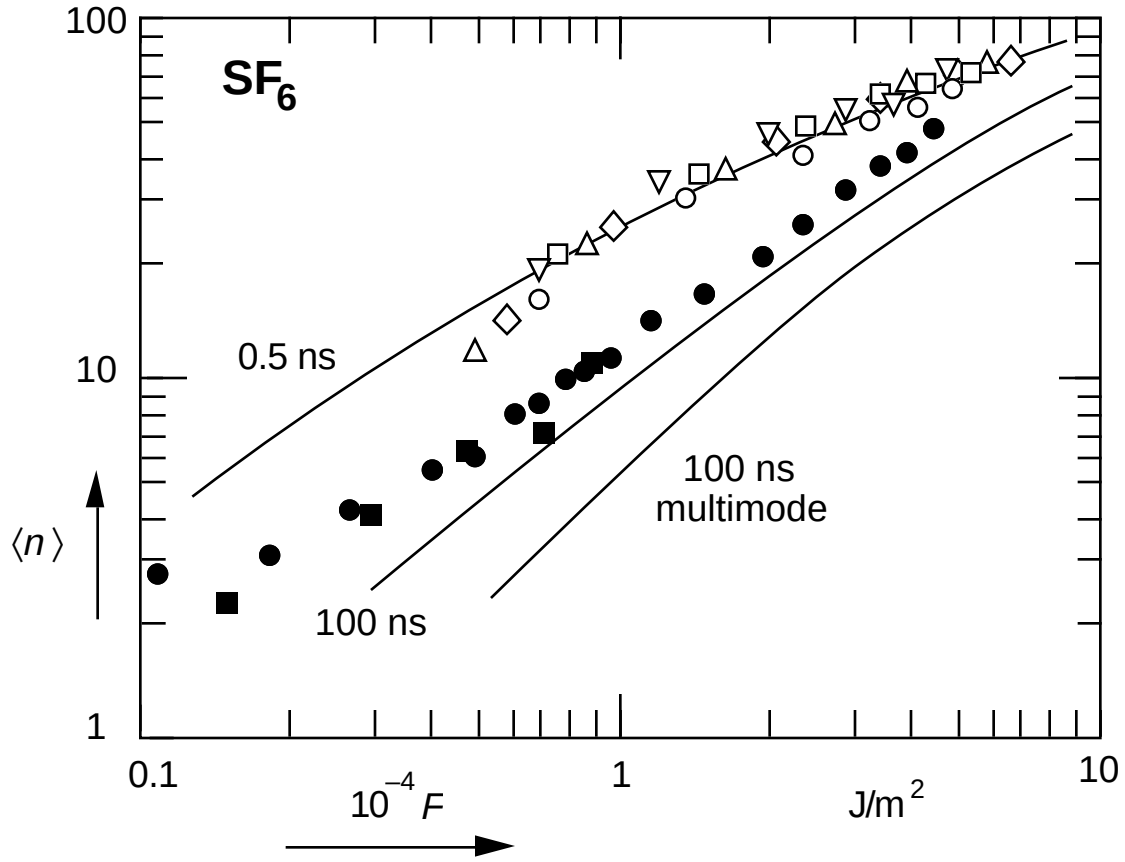

Fig. 3.6. Average number of infrared photons absorbed per molecule as a function of infrared fluence. The data points shown were obtained from the ones shown in Fig. 3.5, assuming thermal equilibrium between all vibrational modes immediately after infrared multiphoton excitation. The solid lines are the average number of infrared photons obtained from the photoacoustic measurements reported in Ref. 4

It should be pointed out that a collisionless increase in anti-Stokes signal within 20 ns can still be observed at infrared fluences as low as 3×10^2 J/m^2,[7] where the average infrared absorption of SF_6 is reported to be below 1 photon per molecule.[1] At these fluences the *inter*molecular vibrational energy distribution—in contrast to the *intra*molecular distribution—is not in equilibrium. Apparently even at low infrared fluence

a small and yet measurable fraction of molecules is excited high enough to show a change in Raman spectrum, while most molecules remain unexcited.

3.4 Results for CF_2Cl_2

Freon-12, CF_2Cl_2, is an interesting molecules because three of its nine vibrational modes[5] at a shift of 667, 923 and 1098 cm^{-1} are accessible to our experimental setup. In addition, two of these three modes can be pumped by a CO_2 laser. This allows one to pump the molecule at two different infrared absorption modes, and also to monitor directly the excitation in the pump mode. In our experiments on CF_2Cl_2, either the ν_8 mode (923 cm^{-1}) or the ν_1 mode (1098 cm^{-1}) was pumped by short CO_2 laser pulses. At the same time the Raman signals of these two modes as well as the signal from the third Raman active mode at 667 cm^{-1} were monitored.

All experiments on CF_2Cl_2 were carried out with 15-ns CO_2-laser pulses. Because the CO_2 laser frequencies employed to pump this molecule are away from the peak of the CO_2 laser gain profile, not enough energy was available to perform experiments with shorter pulses.

3.4.1 Raman Spectrum of CF_2Cl_2

Figure 3.7 shows the Raman spectrum of CF_2Cl_2, obtained with and without infrared pumping on the ν_8 mode. As in the Raman spectrum of SF_6, the large central peak in the spectrum corresponds to elastic scattering. Because of the low population of excited levels at room temperature, only Stokes signals can be detected in the absence of infrared pumping. These room temperature data are shown in the right hand side of the graph; the corresponding anti-Stokes side of the spectrum has been omitted. After excitation large anti-Stokes signals appear. The Stokes and anti-Stokes peaks marked by arrows, at 356.5 nm and 336 nm respectively, correspond to the pumped ν_8 mode. The large differences in the heights of the Stokes peaks in the right hand side of the graph reflect the large variation in Raman scattering cross section of the Raman modes. The peak closest to the central Rayleigh scattering peak belongs to the ν_2 mode which has the largest Raman cross section. The smallest peak, marked by an arrow, belongs to the ν_8 mode which is pumped by the CO_2 laser. One can obtain an indication of the average excitation in each mode from the normalized anti-Stokes intensity as described in Eq. (2.20).

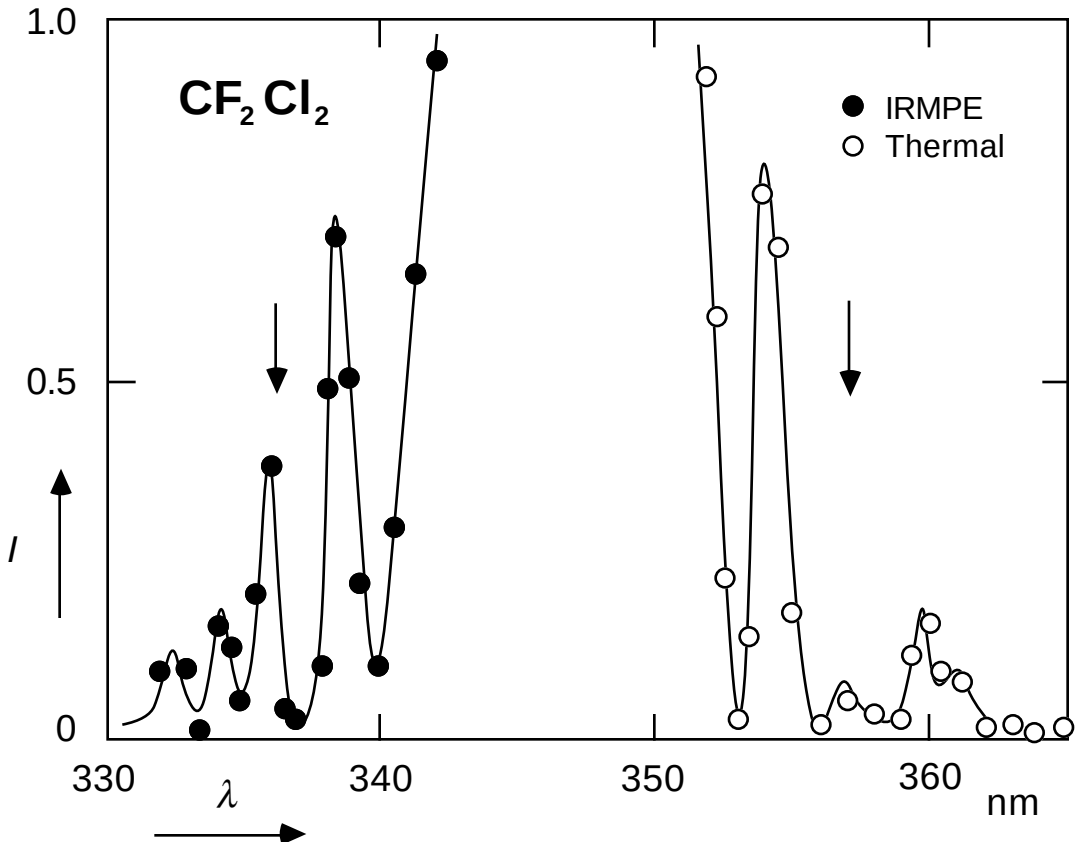

Fig. 3.7. Room temperature Stokes Raman spectrum of CF_2Cl_2 (open circles), and anti-Stokes Raman spectrum after infrared multiphoton excitation (closed circles) with 15 ns pulses at the 10.6 μm P(32) line. The arrows mark the position of the infrared pump mode.

3.4.2 Intramolecular energy distribution

In this experiment the input slit is chosen so as to spectrally integrate over a 1.5-nm width. A comparison between the intramolecular vibrational energy distribution after infrared multiphoton excitation of the ν_8 mode and a thermal distribution is shown in Fig. 3.8. The left graph shows the energy distribution after infrared multiphoton excitation, with and without buffer gas, and the right side the thermal distribution at a

temperature where the total energy in the three modes equals the measured total energy in the three modes in the multiphoton excitation case. The difference between the thermal distribution and the one after infrared multiphoton excitation clearly shows that this

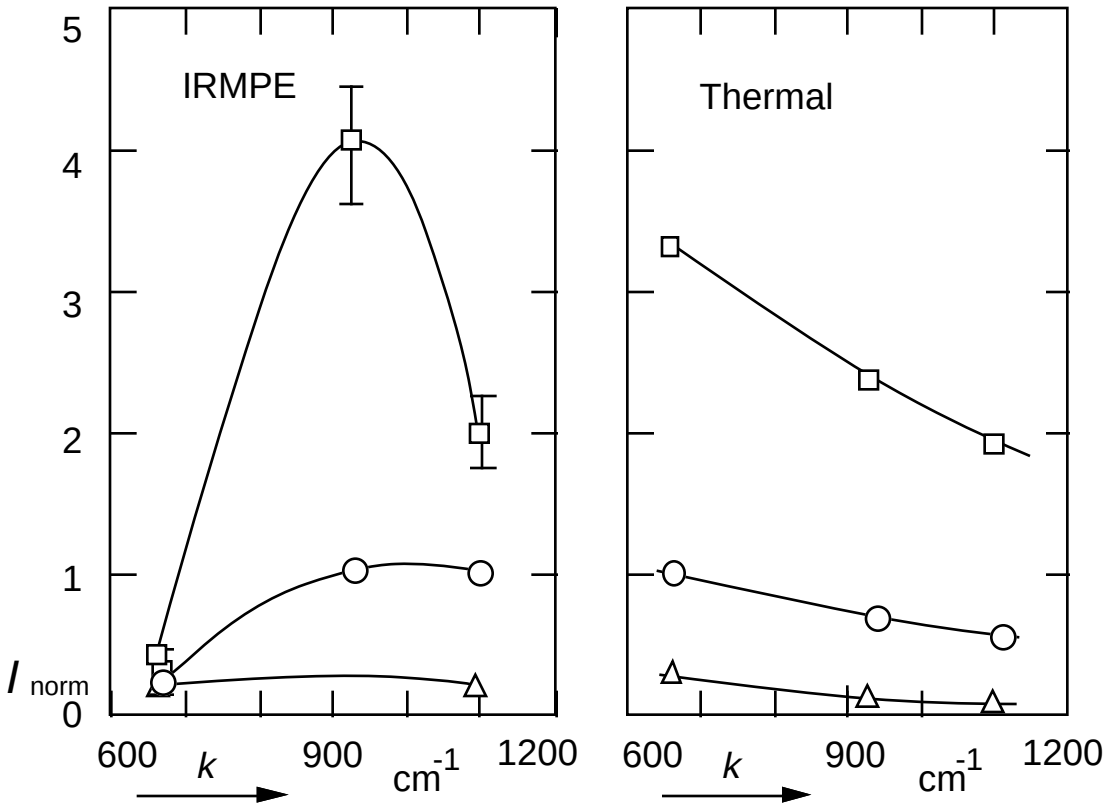

Fig. 3.8. Comparison of the observed normalized anti-Stokes signals of CF_2Cl_2 after excitation of the ν_8 mode with calculated equilibrium values. The lower data points show the effect of collisional relaxation due to N_2 buffer gas circles: 13 kPa; triangles: 26 kPa.

molecule is not in equilibrium after the excitation. Also, from Fig. 3.8 it can be seen that, as one would expect, the energy distribution approaches the thermal one as buffer gas is added to the sample.

When we changed the CO_2 laser to 9*R*24 line, the ν_1 mode became the pumped mode. The intramolecular energy distribution is shown in Fig. 3.9. Again, a nonequilibrium distribution is observed. The ν_1 mode, which is also the pumped mode, has the highest energy.

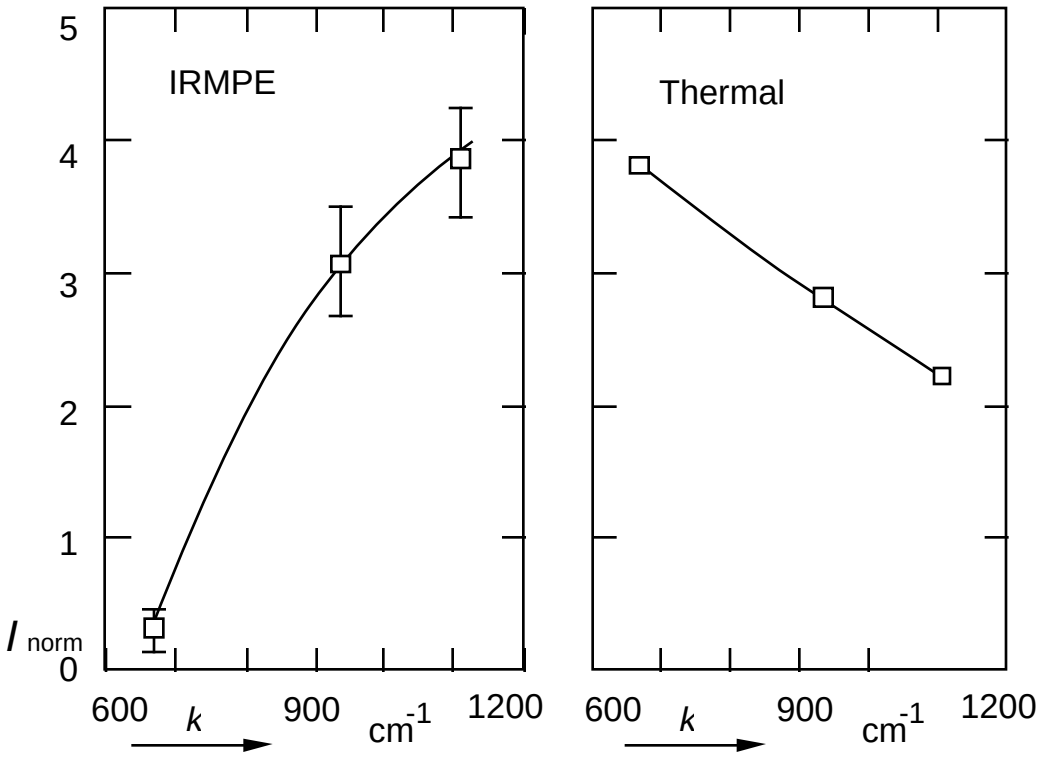

Fig. 3.9. Comparison of the observed normalized anti-Stokes signals of CF_2Cl_2 after excitation of the ν_1 mode with calculated equilibrium values.

As described in Ref. 2, in contrast to the nearly linear fluence dependence of SF_6, CF_2Cl_2 shows an exponential dependence. The exponential rate of increase rate of the Raman signals with respect to the increase of the pumping fluence are about the same for the ν_8 and ν_1 modes and significantly lower for the ν_2 mode.

3.5 Conclusion

This chapter summarizes results obtained from spontaneous Raman scattering experiments on infrared multiphoton excited SF_6 and CF_2Cl_2. The intramolecular vibrational energy distributions after infrared multiphoton excitation were obtained by comparing the normalized anti-Stokes intensities of different Raman active modes. These normalized intensities are direct measure of the energy in the modes.

For SF_6, the results present strong evidence that an intramolecular equilibrium among the various vibrational modes is achieved within the 20 ns experimental time resolution. In contrast, the results for CF_2Cl_2 show a non-thermal energy distribution among the observed Raman active modes of infrared multiphoton excited CF_2Cl_2 which tends toward equilibrium as an increasing amount of buffer gas is added. The observed anti-Stokes signals show that even at high excitation the intramolecular vibrational energy distribution is nonequilibrium, with an excess of energy in the pumped mode.

The spontaneous Raman technique was also applied to other molecules such as CH_3CHF_2 and CF_2HCl. The results of these measurements can be found in 6

In addition to the energy distributions among different Raman modes obtained from these measurements, it is necessary to obtain information of the energy distributions among individual vibrational states to better understand the excitation mechanism. State-specific information can be obtained with the coherent anti-Stokes Raman spectroscopy technique

described in chapter two. The next three chapters presents results of a CARS study of infrared multiphoton excited molecules both in bulk and in a supersonic beam.

References

1 Jyhpyng Wang, Kuei-Hsien Chen and Eric Mazur, *Phys. Rev.* A, **34**, 3892 (1986)

2 K.H. Chen, J. Wang, and E. Mazur, *Phys. Rev. Lett.* **59**, 2728 (1987)

3 G. Herzberg, *Molecular spectra and molecular structure*, Vol. 2 (Van Nostrand Reinhold, New York, 1979)

4 J.G. Black, P. Kolodner, M.J. Shultz, E. Yablonovitch, and N. Bloembergen, Phys. Rev. **A19**, 704 (1979)

5 Charles A. Bradley, JR. *Phys. Rev.* **40**, 908 (1932)

T. Shimanouchi, *J. Phys. Chem. Ref. Data* **6**, 993 (1977)

6 J. Wang, K.H. Chen, and E. Mazur, *Laser Chem.* **8**, 97 (1988)

CHAPTER 4

COHERENT ANTI-STOKES RAMAN SPECTROSCOPY EXPERIMENTS

4.1 Introduction

The spontaneous Raman experiments described in the previous chapter provide data on the average number of vibrational quanta in the probed Raman modes. From this, the intramolecular energy distribution can be deduced and information is obtained on the excitation and relaxation processes. The technique does not provide detailed information on the population distribution *within* each vibrational mode—information that is crucial for a complete understanding of the excitation mechanism. To achieve this goal, one needs state-specific information such as provided by coherent anti-Stokes Raman spectroscopy as described in chapter 2. This chapter presents the results from bulk coherent anti-Stokes Raman experiments on infrared multiphoton excited molecules. An extension of this technique to a supersonic molecular beam system follows in the next two chapters.

4.2 Experimental setup

A schematic view of the setup is shown in Fig. 4.1. The infrared radiation is generated by a grating-tuned CO_2 laser with a 250-ns pulse duration and a maximum

energy of 200 mJ. The infrared beam is focused into the interaction cell by a cylindrical lens with a 15-cm focal length. The CARS laser beams are derived from the output of a

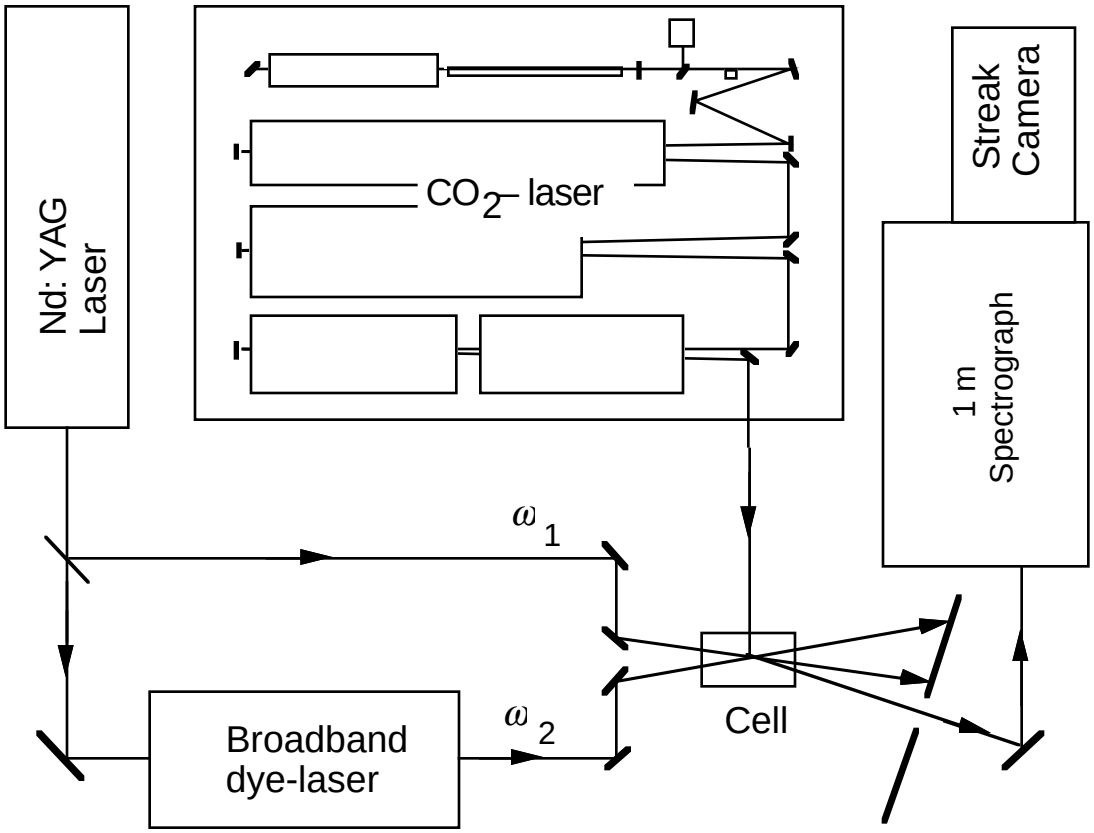

Fig. 4.1. Setup for coherent anti-Stokes Raman spectroscopy of infrared multiphoton excited molecules. Sample molecules are excited by a picosecond CO_2 laser, and probed by coherent anti-Stokes Raman scattering. The coherent anti-Stokes Raman probe consists of an etalon-narrowed frequency-doubled Nd:YAG laser and a broadband dye laser pumped by the Nd:YAG laser. See chapter 3 for details on the CO_2 laser system.

Quantel YG471C Nd:YAG laser with a 10-ns pulse duration and a 200-mJ average second-harmonic output at 532 nm. A line-narrowing etalon has been installed inside the cavity to

reduce the linewidth to 0.05 cm^{-1}. About 50 mJ of the second harmonic is used for the two ω_1 beams (25 mJ each), while the remainder serves to pump a broad band dye laser-amplifier system at ω_2. The prism-tuned broadband dye laser, operating on Fluorescein 548 dye around 550 nm, produces 2-mJ pulses of 6-ns pulse duration, and 60-cm^{-1} linewidth. These pulses are amplified to 20 mJ in two stages. The ω_1 and ω_2 beams are vertically polarized, and are aligned parallel to one another before being focussed into the scattering cell with a 25-cm focal length lens. The infrared laser beam and the CARS laser beams cross at right angles inside the scattering cell. The beam waist and the interaction length of the CARS beams are 80 μm and 200 μm, respectively. The dimensions of the infrared pump beam in the interaction region are 110 μm and 18 mm, respectively.

The CARS beam generated in the interaction cell passes through an aperture which spatially rejects the ω_1 and ω_2 beams as shown in Fig. 4.1. The signal is then dispersed using a Jarrel Ash 78-420 1-m f/6.2 monochromator with a 0.05-Å resolution in second order. Instead of using the output slit of the monochromator, the dispersed CARS signal is recorded on the (horizontal) entrance slit of a Hamamatsu C1587 streak camera system with a 512 by 512 detector array. The resulting spectral resolution of the entire system is 0.12 Å. The dispersion of the monochromator was calibrated with the 6-Å separation of the two Na *D*-lines. For each spectrum an average over 50 laser shots is taken to obtain a good signal-to-noise ratio.

Because of the difficulty in accurate synchronization of the CO_2 and Nd:YAG lasers and the streak camera, the measurements presented in this thesis do not make use of the temporal resolution of the streak camera. Instead, time-resolution was obtained by varying the delay between the pump and the probe pulses. The synchronization of the lasers is achieved electronically by controlling the timing between the *Q*-switch of the Nd:YAG laser and the voltage drop of the high voltage discharge plates of the CO_2 laser. The time-delay

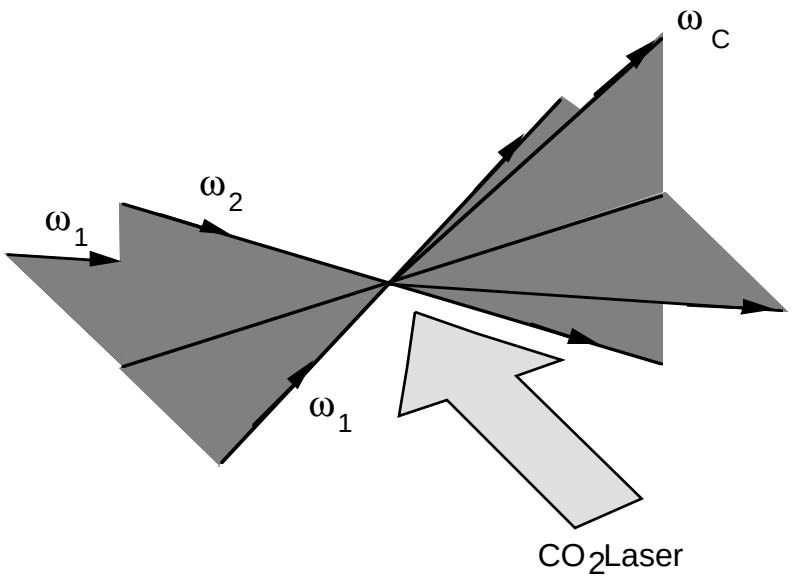

Fig. 4.2. Beam configuration for folded BOXCARS. The CARS beam is in a different direction from all other beams, allowing spatial rejection of the other laser beams.

can be varied from 0 to 6 μs with a 20-ns jitter. In the near future we plan to improve this by making use of shorter (subnanosecond) infrared pulses and obtaining the timing information from the streak camera. In that case both spectral and time dependence of the CARS signal can be obtained in a single shot.

A number of consistency checks were performed. First, it was verified that the signal only occurs in the presence of all three input laser beams. Second, by varying the pressure of the gas sample, it was shown that the CARS signal depends quadratically on the sample pressure as expected from the ΔN^2 dependence in Eqs. (1) and (2). However, when the intensity of the ω_1 or ω_2 beams was varied by putting neutral density filters in the laser beam paths, we could not obtain the expected relation between the CARS signal and intensities of the ω_1 and ω_2 beams as described in Eq. (1). This difficulty, which is

common in all nonlinear optical techniques, can be attributed to the fact that the beam overlap in the interaction region changes when filters are inserted in the laser beam paths.

4.3 OCS results

The OCS molecule has three widely separated fundamental modes (ν_1 = 859 cm^{-1}, ν_2 = 527 cm^{-1}, ν_3 = 2079 cm^{-1}) as shown in Fig. 4.3. The overtone of the ν_2 mode can be excited with CO_2 laser frequencies between the P(10) and P(26) lines of the 9.6 μm branch. Because of the wide separation of the vibrational modes of OCS, and also because of a low density of states, the intramolecular vibrational energy transfer is very inefficient.[1] In contrast, pumping and population redistribution within the ν_2 bending mode, excited by the CO_2 laser, is very efficient owing to the small anharmonicity. Thus, OCS is an ideal molecule for studying the interaction of a single anharmonic oscillator with an intense infrared laser field.[2]

As we have seen in chapter 1 the vibrational Raman spectra are determined by the vibrational energy. For OCS, Eq. (1.2) reduces to

$$\begin{aligned} E(v_1,v_2^{l},v_3) =& (v_1+\tfrac{1}{2})\, h\nu_1 + (v_2+1)\, h\nu_2 + (v_3+\tfrac{1}{2})\, h\nu_3 + \\ &+ x_{11}\,(v_1+\tfrac{1}{2})^2 + x_{22}\,(v_2+1)^2 + x_{33}\,(v_3+\tfrac{1}{2})^2 + \\ &+ x_{12}\,(v_1+\tfrac{1}{2})(v_2+1) + x_{13}\,(v_1+\tfrac{1}{2})(v_3+\tfrac{1}{2}) + x_{23}\,(v_2+1)(v_3+\tfrac{1}{2}) + h\, g_{22}\, l^2 + \ldots, \end{aligned} \tag{4.1}$$

where v_i is the vibrational quantum number of mode i, x_{ij} the (cross) anharmonicity, l the vibrational angular momentum for the two-fold degenerate ν_2 mode, and g_{22} the anharmonicity of the l states. The first line in the right hand side of Eq. (4.1) contains the harmonic contributions, the second line the anharmonic ones, and the third line cross-

anharmonic and vibrational angular momentum contributions. Measurement of the OCS spectra thus provides information on the cross anharmonicities and the population of the various vibrational states.

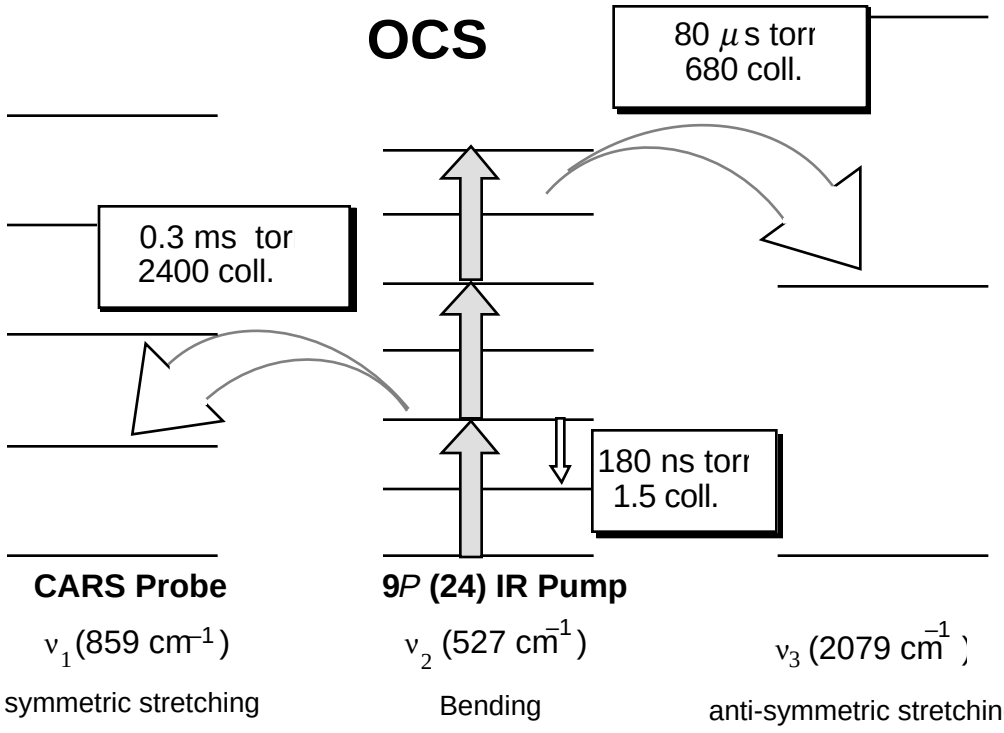

Fig. 4.3. Energy diagram of OCS. The overtone transition of the bending ν_2 mode is resonant with the 9*P*(22) line of the CO_2 laser. The symmetric stretch ν_1 mode is probed by coherent anti-Stokes Raman spectroscopy. The energy transfer rates between modes are from Ref. 1, and the collisional relaxation rate of the ν_2 mode is from the measurements reported in Chapter 6.

4.3.1 CARS spectrum

The CARS spectrum of OCS at room temperature is shown in Fig. 4.4. The peak most to the right in the figure is the ground state peak for the ν_2 mode, and corresponds to

the vibrational transition between the (v_1,v_2,v_3) = (0,0,0) and (1,0,0) states. The second peak from the right reflects the bending hot band (0,1,0) → (1,1,0), and the barely visible peak most to the left is due to the ground state of the ^{34}S isotope, which has a 4% natural

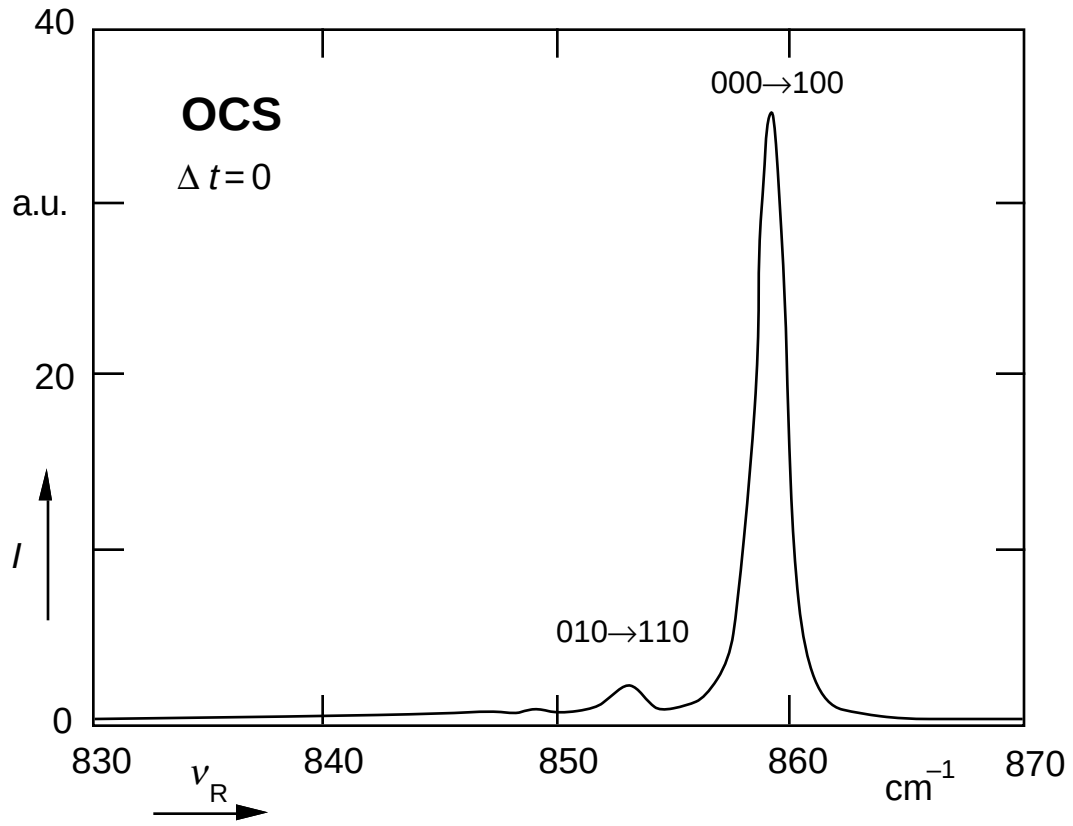

Fig. 4.4. CARS spectrum of OCS at p = 100 Torr and T = 300 K. The assignment (0,n,0) → (1,n,0) indicates the CARS transition between the (0,n,0) and (1,n,0) states.

abundance. This ^{34}S ground state peak is just at the limit of the sensitivity of our apparatus.

From the position of the peaks in the CARS spectra one can determine the value of the cross-anharmonicities. From Eq. (4.1) we see that the ν_2 hot band peaks of the ν_1

mode are displaced by multiples of the cross-anharmonicity x_{12}. The displacement between the $(000) \rightarrow (100)$ and the $(010) \rightarrow (110)$ peaks (as in Fig. 5) yield $x_{12} = -6.0$ cm^{-1}. A comparison of this result with published cross-anharmonicities[3,4,5] is shown in Table 4.1.

4.3.2 CARS spectra after IR excitation

After infrared excitation dramatic changes in the spectrum occur. Figure 4.5 shows a typical spectrum 200 ns after infrared excitation. A large decrease in the fundamental peak is observed (note the difference in vertical scale) and additional hot bands corresponding to excitation in the ν_2 ladder up to $v_2 = 4$ appear in the spectrum. The fourth overtone peak always appears to be split.

For longer delays the spectrum continues to change. Figure 4.6 shows the spectrum 4 μs after the infrared pump. A comparison of Figs. 4.5 and 4.6 shows that at longer time-delays additional small peaks appear between the ν_2 hot band peaks. These peaks are due to collisional transfer of population to the excited states of the ν_3 mode, and can be attributed to the ν_3 hot band, *i.e.* $(0,0,1) \rightarrow (1,0,1)$, $(0,1^1,1) \rightarrow (1,1^1,1)$, etc. In analogy to the ν_2 hot band, these ν_3 hot band peaks are displaced from the ν_2 hot band peaks by the anharmonicity x_{13}. From the position of the small peaks it follows that $x_{13} = -2.7$ cm^{-1}, which agrees well with literature values (see Table 4.1).

4.3.3 Time-evolution of CARS spectra

The overall time-evolution of the CARS spectrum at 50 Torr is shown in Fig. 4.7.

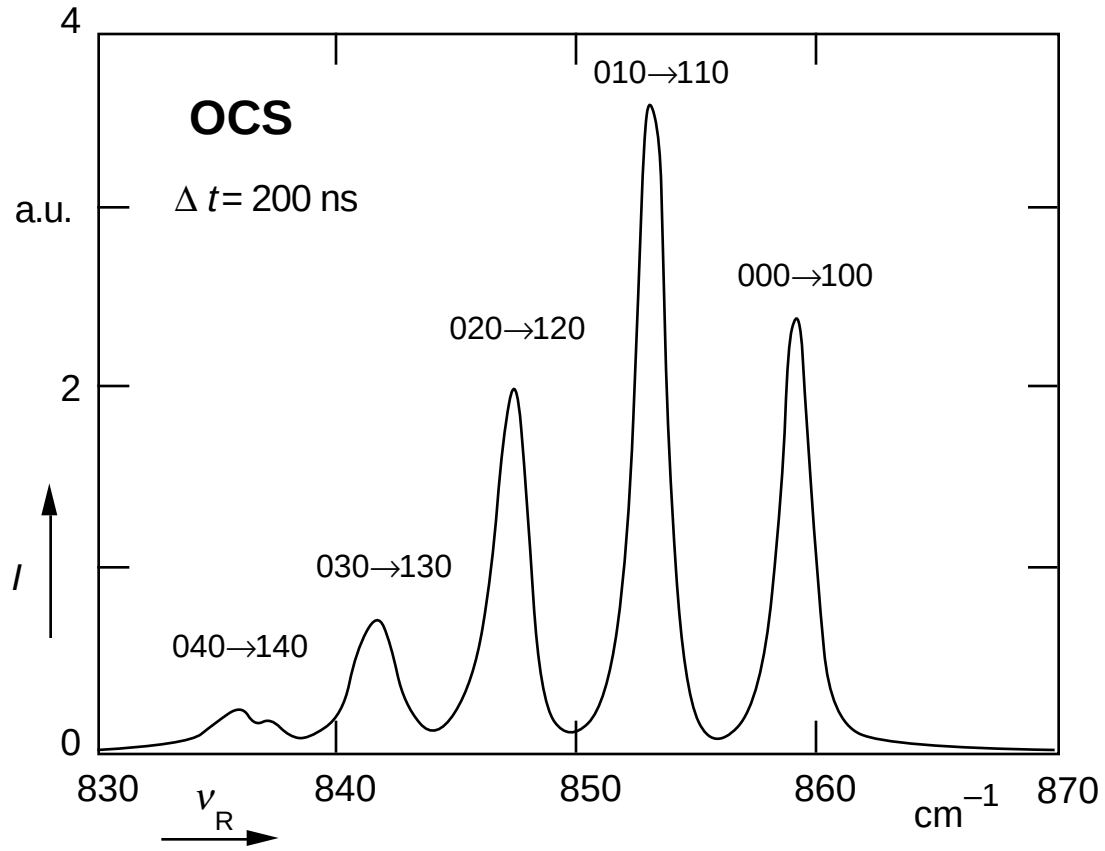

Fig. 4.5. CARS spectrum of OCS at p = 100 Torr, 200 ns after excitation with a CO_2 laser fluence of 9.2 J/cm^2. The peak for $\nu_2 = 3$ is broadened and the one for $\nu_2 = 4$ split. Because of the degeneracy factor ν_2+1, the fact that the $\nu_2 = 1$ peak is more intense than the one for $\nu_2 = 0$ does not necessarily imply a population inversion.

Note the strong ground state signal depletion for times $t < 1$ μs, and the slow recovery at longer time-delays. In contrast, the other peaks in the v_2 hot band grow and then decrease again. At the same time, the intensity of the additional small peaks in between the v_2 hot band peaks increases with time.

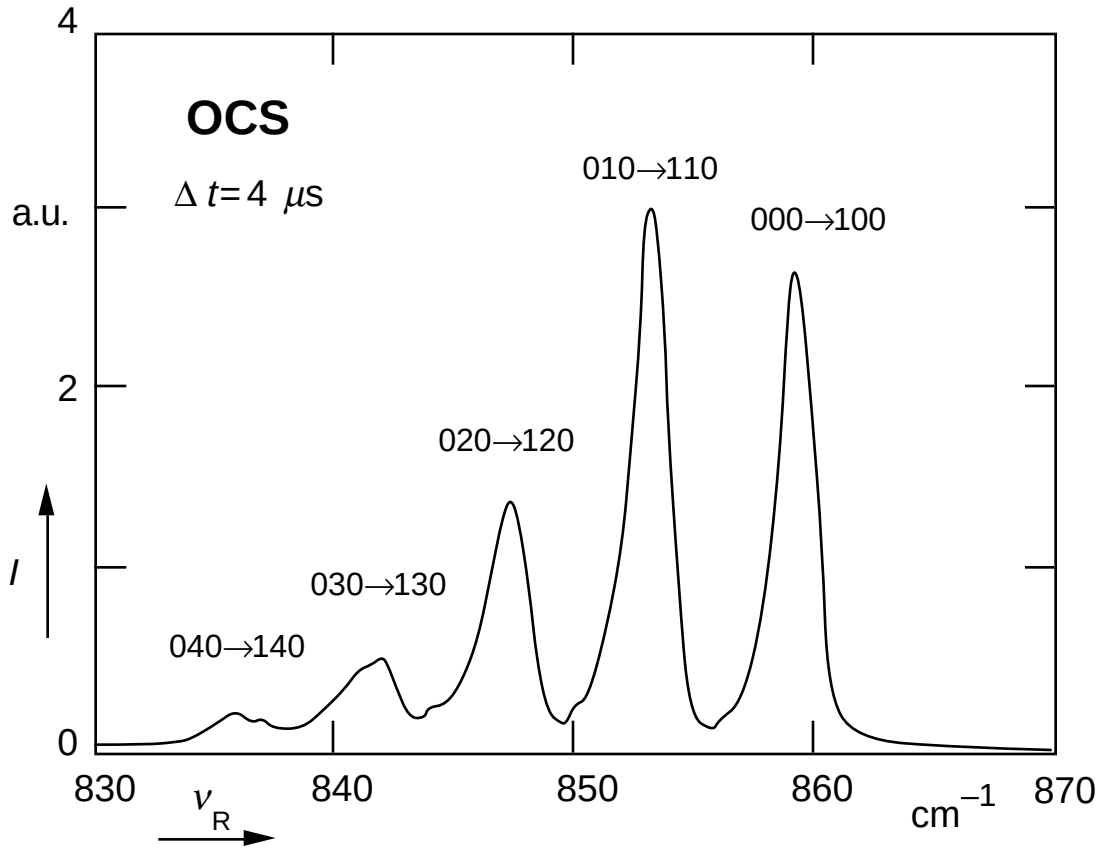

Fig. 4.6. CARS spectrum of OCS at p = 100 Torr, 4 μs after excitation. CO_2 laser fluence: 9.2 J/cm^2. Each peak is broadened and more asymmetric indicating that energy is transferred to the rotational degrees of freedom. The small peaks in between the peaks are from the ν_3 hot band.

	This work (cm^{-1})	Calculated Ref. 3	Measured Ref. 4	Measured Ref. 5
x_{12}	–6.0	–7.16	–7.0	–3.14
x_{13}	–2.7	–2.97	–	–2.53

TABLE 4.1. Comparison of the cross-anharmonicities of OCS obtained in this paper with calculated and measured values from literature. The data in Ref. 21** are from spontaneous Raman spectra of liquid OCS.

From the time-dependence of the spectra one can obtain information on the vibrational relaxation rates. The fast relaxation of energy within the ν_2 mode is most clearly reflected by the fact that even though the laser populates the $v_2 = 2$ state, the population of the $v_2 = 1$ state always exceeds the population of the $v_2 = 2$ state. In general, the large population in the odd states implies that the energy transfer rate to those states exceeds the excitation rate. The observed equilibration of energy on a time scale of 100 ns at 10 Torr provides a lower limit of $k_{\nu_2 \rightarrow \nu_2} \geq 1\ \mu s^{-1}\ \text{Torr}^{-1}$ for the collisional relaxation rate of the ν_2 mode. The measurements in a supersonic beam described in chapter 6 provide more accurate data on the collisional relaxation rate.

Energy transfer rates between the ν_2 and the other vibrational modes have been reported in the literature.[13] The reported rate constants are $k_{\nu_2 \rightarrow \nu_3} = 12\ \text{ms}^{-1}\ \text{Torr}^{-1}$, and $k_{\nu_2 \rightarrow \nu_1} = 3.3\ \text{ms}^{-1}\ \text{Torr}^{-1}$. The appearance of the ν_3 peaks and the signal depletion discussed below are consistent with these relaxation rates. Finally, comparing Figs. 5 and 6, one notices that the peaks in Fig. 6 are more asymmetric. This can be attributed to population of higher rotational states at longer delay times because of relaxation of vibrational energy to the rotational degrees of freedom.

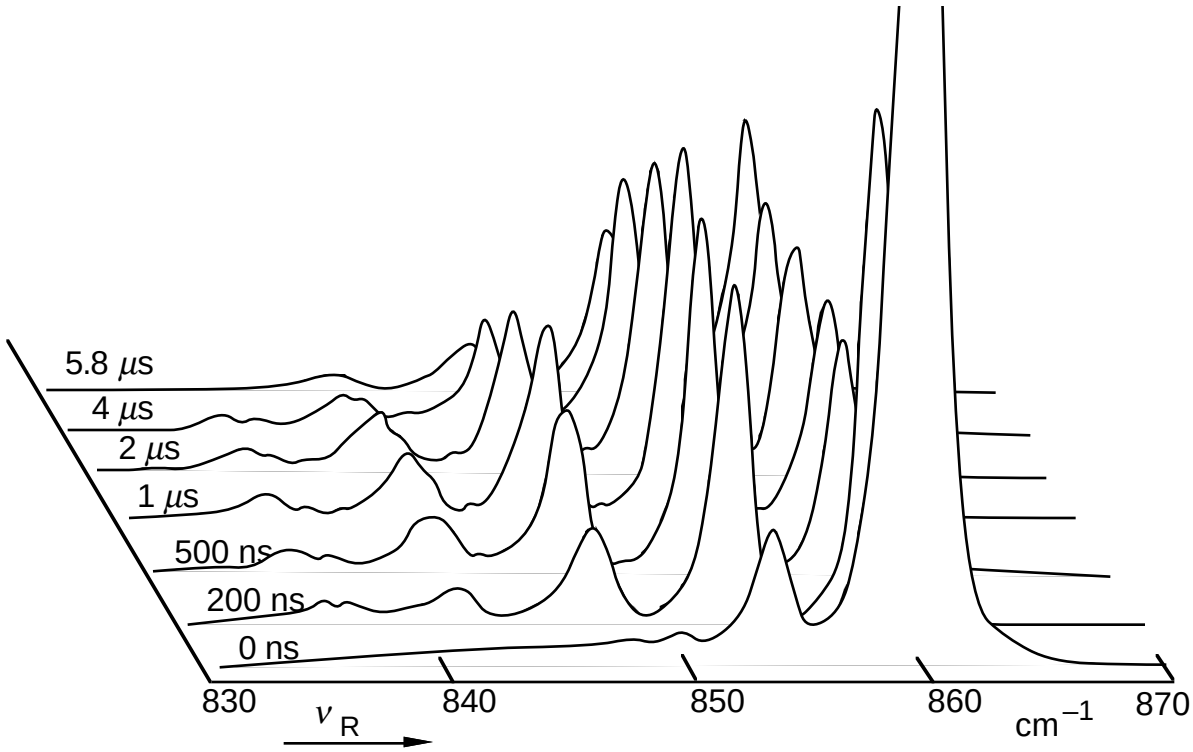

Fig.4.7. CARS spectrum for OCS at p = 50 Torr, for various delay times after excitation. CO_2 laser fluence: 9.2 J/cm^2.

4.3.4 IR Laser wavelength dependence

The dependence of the excitation on the CO_2 laser wavelength was also investigated by tuning the laser from the $P(10)$ to $P(26)$ line on the 9.6 μm branch. The experiment was performed at a pressure of 70 Torr, a delay of 1 μs, and an infrared fluence of 7.6 J/cm^2. For each run the population distribution and temperature of the ν_2 mode was determined as described above. Where deviations from a Boltzmann distributions occurred, the best fit value was taken. The results are summarized in Table 4.2, together with the CO_2 laser excitation wavelength, the closest rovibrational overtone transition,[19] the energy mismatch between them, as well as the room temperature population of the initial rotational state.

CO_2 line	Energy (cm^{-1})	Transition $(0,0,0) \rightarrow (0,2^0,0)$	cm^{-1}	N_J	mismatch (cm^{-1})	T_{v2} (K)
$P(26)$	1041.28	P_{14}	1041.48	0.85	0.20	750
$P(24)$	1043.16	P_{10}	1043.04	0.68	0.12	900
$P(22)$	1045.02	P_5	1045.03	0.38	0.01	1050
$P(20)$	1046.85	P_1	1046.64	0.11	0.21	500
$P(18)$	1048.66	R_3	1048.68	0.25	0.02	800
$P(16)$	1050.44	R_7	1050.33	0.51	0.11	500
$P(14)$	1052.20	R_{11}	1052.01	0.73	0.19	550
$P(12)$	1053.92	R_{16}	1054.13	0.92	0.21	450
$P(10)$	1055.63	R_{20}	1055.85	0.99	0.22	450

Table 4.2. Temperature of the v_2 mode after excitation at different CO_2 lines. Also given are the energy mismatch between the laser wavelength and the closest rovibrational transition from Ref. 6, and the population of the initial rotational state, N_J.

The data in the table clearly show that there is a correlation between the energy mismatch and the excitation temperature, T_{v2}. When the mismatch is small, the excitation is large. In addition, the population of the initial state also plays a role: the larger the population, the larger the fraction of excited molecules, and consequently the higher the excitation temperature. In addition to the mismatch listed in the table, the mismatch of higher lying transitions, such as the $(0,1,0)\rightarrow(0,3,0)$, and $(0,2,0)\rightarrow(0,4,0)$ transitions, also play a role.

4.3.5 Time-evolution of the energy distribution

The intensity distribution of the hot band peaks represents the square of the population distribution in the v_2 mode. Since CARS is a nonlinear technique, however, care must be exercised when determining the population distribution from the intensity distribution.[7] If the rotational lines are closely spaced, which is true for the *Q*-branch spectra of molecules with a small rotational constant, the population distribution $N(E)$ can be obtained by taking the square root of the area within the FWHM of each peak. For the room temperature spectrum shown in Fig. 4.4, the distribution obtained this way is in good agreement with a room temperature Boltzmann distribution. A comparison of the population distributions for infrared multiphoton excited OCS with Boltzmann distributions is shown in Fig. 4.8. The vertical axis plots the population N, obtained from the square root of the FWHM peak area as explained above, divided by the degeneracy $g = v_2 + 1$ of the corresponding level v_2. After a delay of 200 ns, the distribution is still in excellent agreement with a Boltzmann distribution at a temperature of 1200 K. At the highest excitation deviations from a Boltzmann distribution are observed; while the population of all but the ground state are still well described by a Boltzmann distribution at T = 1450 K, the $v_2 = 0$ state has a lower population than expected. Figure 4.9 shows the temperature evolution of the v_2 mode for sample pressures ranging from 10 to 100 Torr.

Figure 4.9 shows that the temperature of the v_2 mode continues to rise for 1 μs. This rise, which is relatively slow compared to the 250-ns FWHM duration of the CO_2 laser pulse, is due to the nitrogen tail of the CO_2 laser pulse or to the relaxation of molecules from highly excited states. In addition, Fig. 4.9 shows that a higher temperature is obtained at higher sample pressures. For short time-delays the temperature increase is nearly linear with pressure, which implies that the excitation is enhanced by collisional

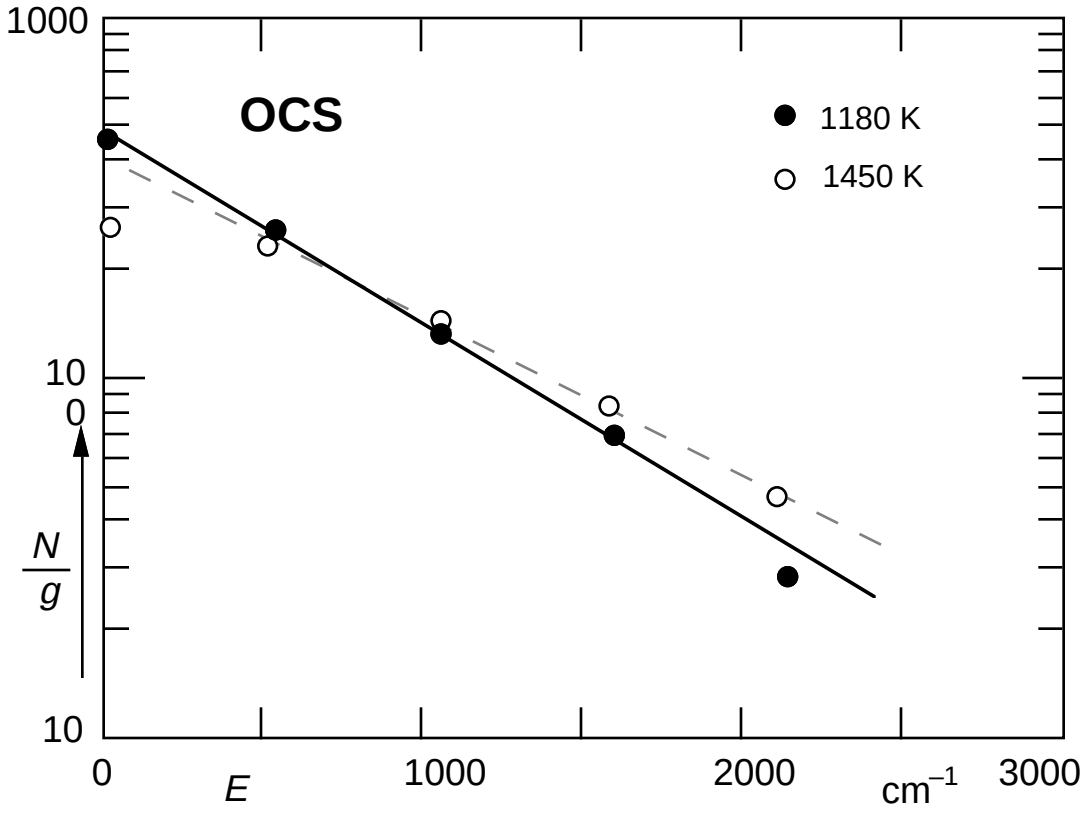

Fig. 4.8. Population distributions of the v_2 mode of OCS at p = 100 Torr, 200 ns (●) and 500 ns (○) after CO_2 laser excitation (9.2 J/cm^2). The closed circles are from the spectrum in Fig. 4.5. The lines show Boltzmann fits for T = 1200 (plain) and T = 1450 (dashed).

processes. This collision assisted excitation can be understood as follows. First, pressure broadening helps compensate for the anharmonicity. Second, because the CO_2 laser is resonant with a specific rovibrational transition, the excitation creates a hole in the rotational manifold.

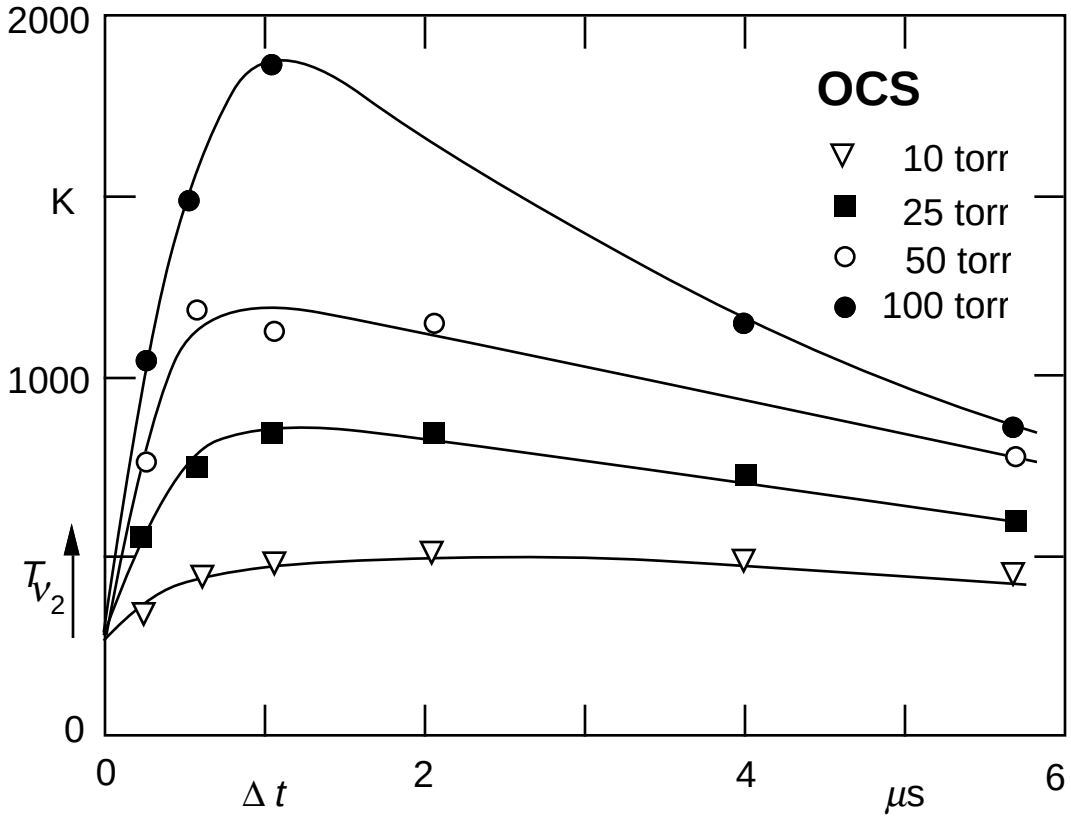

Fig. 4.9. Temperature of ν_2 mode versus delay time after a 9.2 J/cm^2 CO_2 laser excitation for different OCS pressures (▽ : 10 Torr, ■ : 25 Torr, ○ : 50 Torr, ● : 100 Torr).

Collisions redistribute the population in the rotational manifold, refilling the hole, thereby assisting the excitation and reducing saturation of the pumped transition. In addition to the collision assisted excitation, a faster decay in temperature is observed at high pressure, consistent with a collisional relaxation of the excitation energy to other modes and other degrees of freedom.

4.3.6 Missing fraction

In addition to the large decrease of the ground state peak intensity upon infrared irradiation, there is an overall depletion of the CARS signal. This depletion can be seen by analyzing the area of the peaks in the CARS spectra in more detail. According to eqs. (2.35) the square root of the area under each peak is proportional to the population difference between the $(0,v_2,0)$ and $(1,v_2,0)$ states. Fig. 4.10 shows the ΔN obtained by taking the sum of the square root of the areas under each peak. Clearly, there is a decrease in the population difference of the first two states of the ν_1 mode as either the delay time or the pressure increases. This overall signal depletion, which is not unique to OCS, and which has been observed previously also for other molecules,[8,9] can be caused by a number of processes: dissociation, thermal lensing,[10,11] transfer of population to other modes, or to levels above $v_2 = 4$.

Dissociation will result in signal depletion because of a reduced number of molecules in the probed region. Because of contradictory reports in the literature,[12,13] the possible occurrence of dissociation was investigated. Since maximum depletion is observed at high pressure, a 100-Torr sample was irradiated with 1.5×10^5 CO_2-laser pulses (irradiation volume: 10^{-3} cm^3; cell volume: 10 cm^3; fluence: 9.2 J/cm^2; laser line: 9*P*(24)). Subsequent FTIR analysis, with a sensitivity of 100 ppm, showed no trace of CO, one of the dissociation products. This rules out dissociation as one of the possible causes for the observed signal depletion. Thermal lensing can also be ruled out, since the response time for this effect is the same as that for V-T relaxation (0.4 ms Torr) which is significantly longer than the observed signal depletion rate.

The appearance of the ν_3 hot band peaks in Fig. 4.6, shows that the $(v_1,v_2,v_3=1)$ states are populated. Since the CARS signal from the ν_2 hot band is proportional to $(N_{0,v_2,0} - N_{1,v_2,0})^2$, any energy transfer to states other than $(0,v_2,0)$ will diminish the

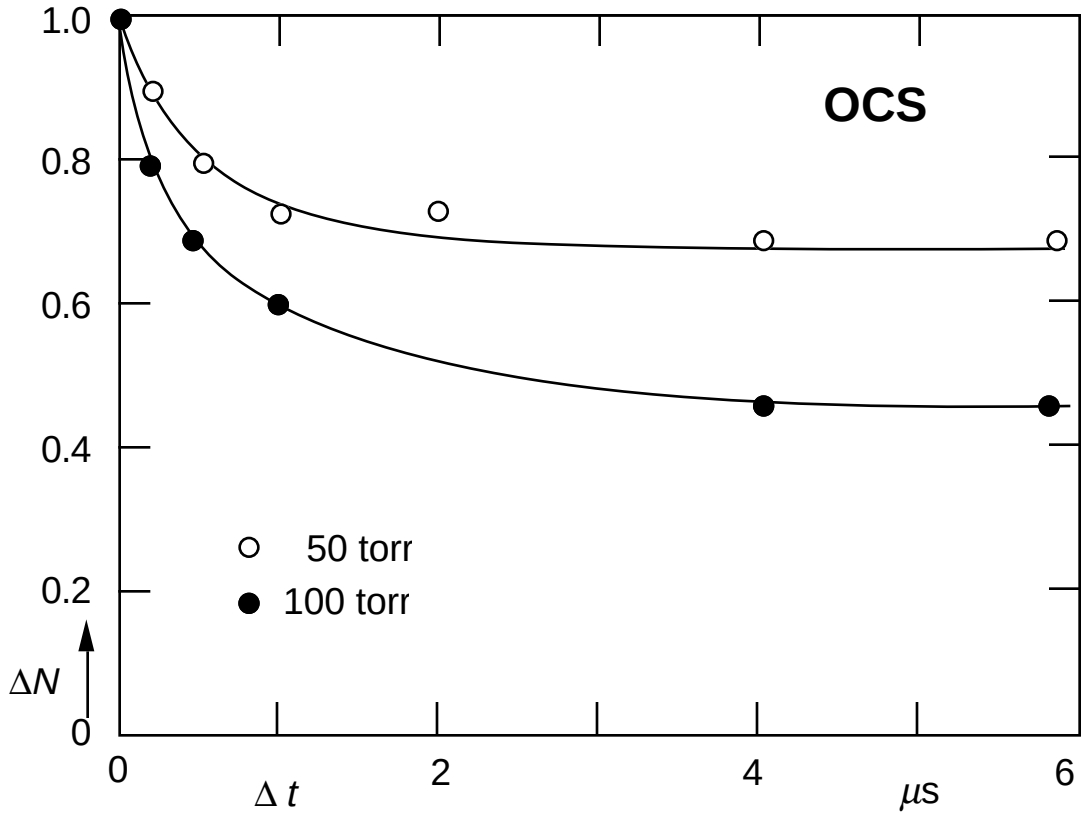

Fig. 4.10. The total population difference ΔN between the $(0,v_2,0)$ and $(1,v_2,0)$ states for $v_2 = (0,\ldots,4)$ versus delay time after a 9.2 J/cm^2 CO_2 laser excitation for different OCS pressures (○ : 50 Torr, ● : 100 Torr).

CARS signal. In addition, population of levels above $v_2 = 4$ is not included in the calculation of ΔN in Fig. 4.10, because the corresponding peaks are not visible in the CARS spectra. The signal depletion in Fig. 4.10 must therefore be attributed to population of states above the $v_2 = 4$ level, and to transfer of energy to the v_1 and v_3 modes.

4.4. SO_2 results

SO_2 is a molecule is similar to OCS except that it is not linear. The SO_2 molecule has three vibrational modes at 1151.3, 517.6, and 1361.7 cm^{-1}. In contrast to the ν_2 mode of OCS, which is two-fold degenerate, the ν_2 mode of SO_2 has no degeneracy. Infrared multiphoton excitation of SO_2 by a CO_2 laser has been reported in the literature.[10,14] Fluorescence due to inverse electronic relaxation after infrared excitation also has been reported.[15] Since the anharmonicities are known (x_{11}=–4.1, x_{12}=–3.1, and x_{13}=–13.2 cm^{-1}),[16] one can resolve the hot band and obtain detailed information about the excitation using coherent anti-Stokes Raman measurements.

SO_2 is interesting because the 9*R*22 line of the CO_2 laser at 1079.85 cm^{-1} lies in between the $0\rightarrow\nu_1$ and $0\rightarrow 2\nu_2$ transition frequencies. Therefore excitation could occur either in the wings of the rotational distribution of the ν_1 mode (with a 71 cm^{-1} detuning), or due to the overtone excitation of the ν_2 bending mode (with a 45 cm^{-1} detuning). Since the symmetric stretch ν_1 mode of SO_2 is Raman active, CARS measurements after infrared excitation can directly determine which of the modes is pumped by the CO_2 laser.

The CARS spectrum of SO_2 obtained at a pressure of 100 Torr and room temperature is shown in Fig. 4.11. The peak at a 3.0 cm^{-1} shift from the ν_1 fundamental can be assigned to the ν_2 hot band in excellent agreement with date published in the literature. The second peak at a 7.3 cm^{-1} shift is attributed in the literature to the fundamental ν_1 mode of the S^{34} isotope.[17]

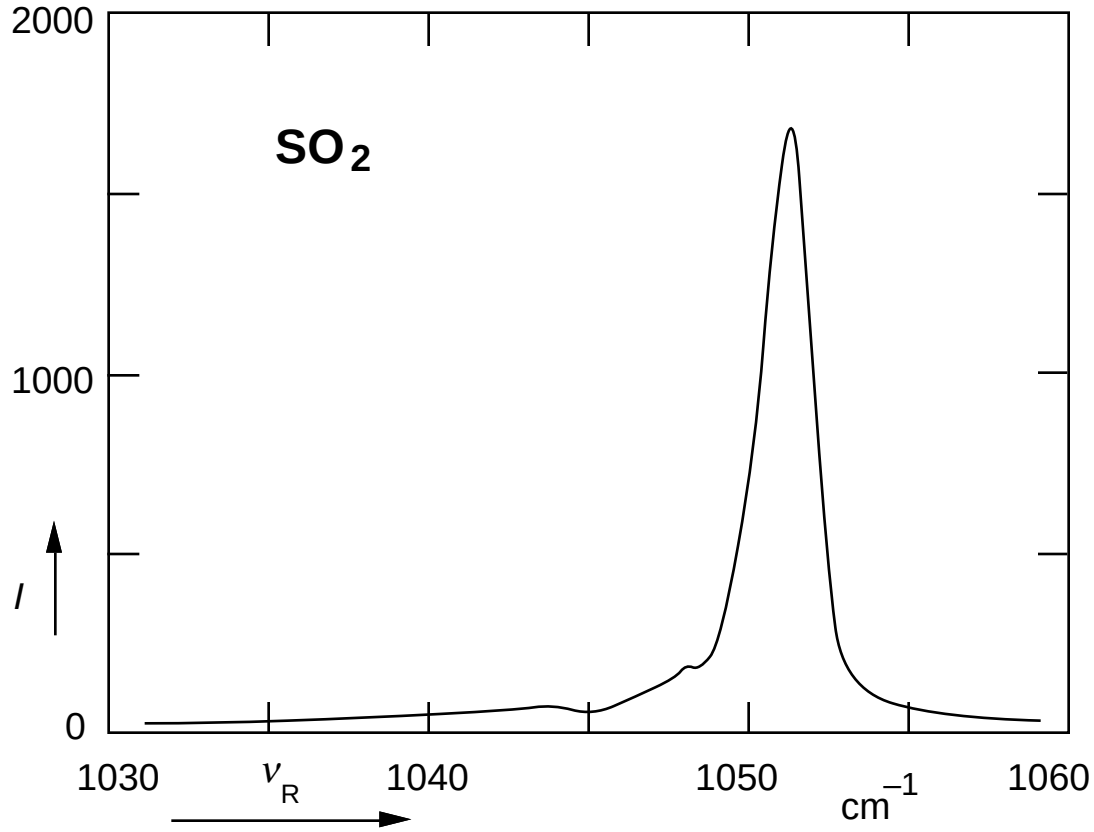

Fig. 4.11. CARS spectrum of the ν_1 mode of SO_2 at p = 100 Torr and T = 300 K. The small peak at a 3.0 cm^{-1} Raman shift from the fundamental is the ν_2 hot band, x_{12} = 3.0 cm^{-1}.

After excitation with a 9R22 CO_2 laser pulse of 9.2 J/cm^2 a decrease of the fundamental peak is observed as shown in Fig. 4.12. The ν_2 hot band increases due to the excitation. Surprisingly, the peak attributed to the ν_1 fundamental of the $^{34}SO_2$ molecule also has a pronounced increase after infrared excitation. In addition there is no trace of a peak at a 4.1 cm^{-1} shift, which is attributed to the x_{11} anharmonicity in the literature.[16]

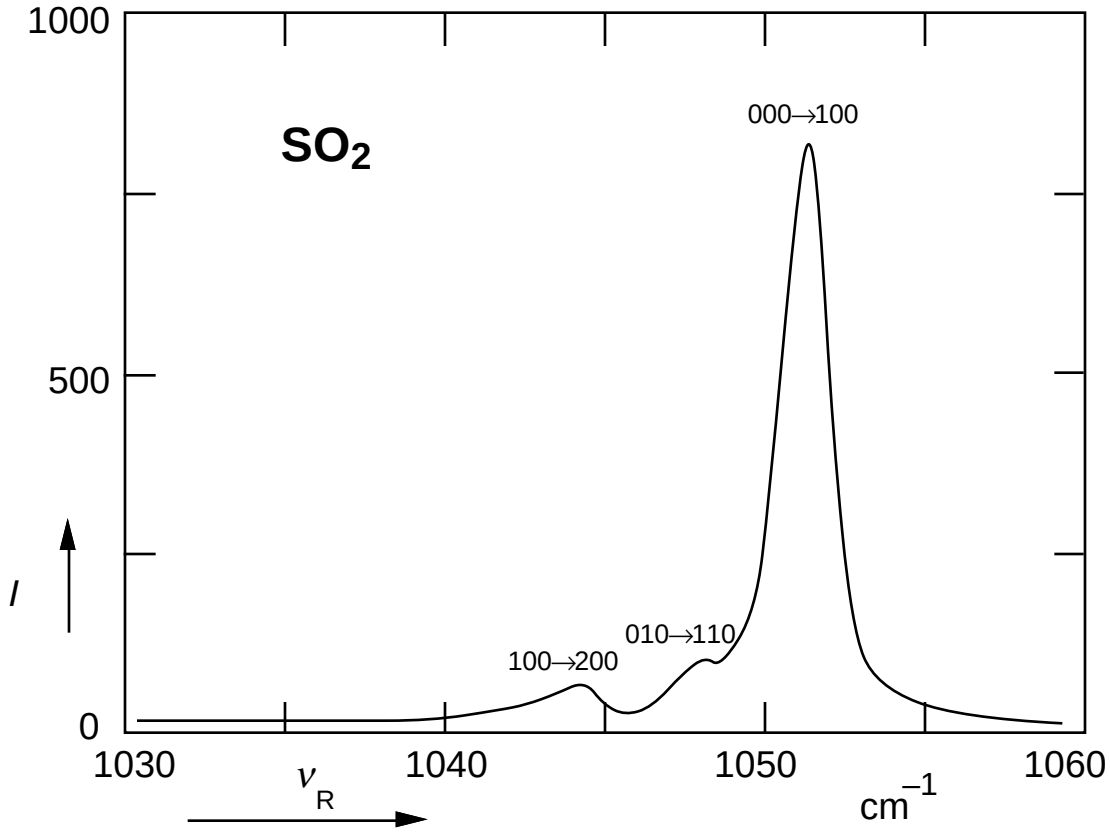

Fig. 4.12. CARS spectrum of the ν_1 mode of SO_2 200 ns after a 9.2 J/cm^2 CO_2 laser excitation. Both peaks at a 3.0 cm^{-1} and 7.3 cm^{-1} shift from the fundamental line increase due to the infrared excitation. See discussion for the assignment of the peaks.

Figure 4.13 shows the spectrum 2 μs after the infrared excitation. The 7.3 cm^{-1} peak is now relatively more intense than other hot bands. Since the calibration of the vertical scales in Figs. 4.11 through 4.13 is not very accurate, there are two possible interpretations of the relative increase of the peak at 7.3 cm^{-1}. One possibility is that the intensity of the 7.3 cm^{-1} peak stays the same while all other peaks decrease after CO_2 laser excitation. The other possibility is that the 7.3 cm^{-1} peak actually increases in intensity. This would be possible, for instance, if it is the hot band of the pump mode, contrary to the

assignment given in the literature. This would lead to a new value for the anharmonicity x_{11} = –7.3 cm^{-1}. As shown in the figure, another peak appears at a –14.6 cm^{-1} shift from the fundamental peak, which seems to support the second interpretation. The results, however, are still preliminary and a more detailed study on infrared multiphoton excited SO_2 is needed for a conclusive interpretation.

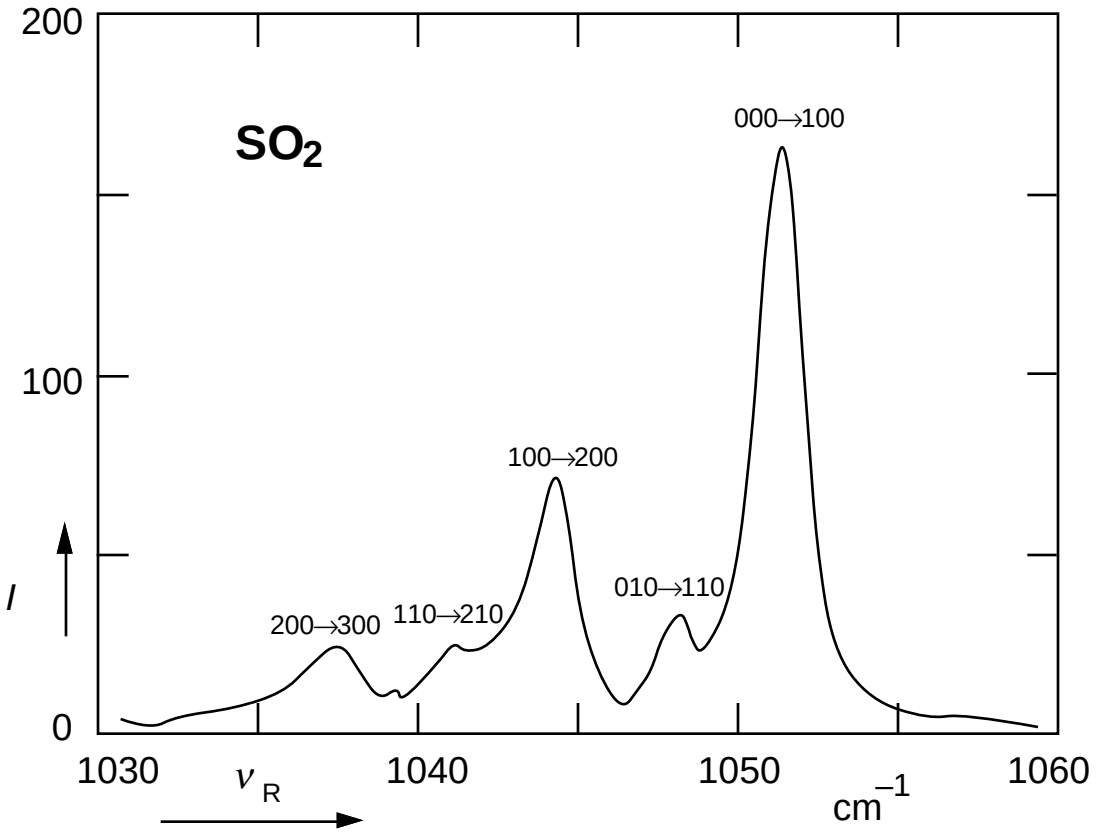

Fig. 4.13. CARS spectrum of the ν_1 mode of SO_2 2 μs after a 9.2 J/cm^2 CO_2 laser excitation. See discussion for the assignment of the peaks.

4.5. Conclusions

This chapter presents a detailed study of the intramolecular vibrational energy distributions in infrared multiphoton excited OCS and SO_2 in the collisional regime using time-resolved multiplex coherent anti-Stokes spectroscopy.

For OCS the anharmonicities and the vibrational relaxation of the excitation energy to other degrees of freedom reported in this chapter are consistent with values reported in the literature. The evolution of the spectra shows that the excitation energy rapidly equilibrates within the pumped ν_2 mode ($k_{\nu_2 \rightarrow \nu_1} \geq 1\ \mu s^{-1}\ Torr^{-1}$), and that at all but the highest excitation the population in the ν_2 mode is well described by a Boltzmann distribution.

The preliminary results of the CARS spectra of the infrared multiphoton excited SO_2 indicate another possible interpretation of the assignment of the hot bands. Further studies are required to verify the excitation process.

The measurements presented in this chapter show that coherent anti-Stokes Raman spectroscopy is a powerful tool for the study of infrared multiphoton excitation. Before applying the technique to other molecular systems a number of improvements to the apparatus were applied. First, a pulsed supersonic beam was used to provide cooled and nearly collisionless molecules. Second, the pure rotational CARS scheme was used to monitor the rotational distribution after infrared excitation. The next two chapters show how vibrational and rotational CARS studies of molecules in a supersonic beam provides even more detailed information on infrared multiphoton excitation.

References

1 M.L. Mandich and G.W. Flynn, *J. Chem. Phys.* **73**(3), 1265 (1980)

2 K.H. Chen, C.Z. Lu, L. Aviles, E Mazur, N. Bloembergen, and M.J. Shultz, *J. Chem. Phys.* **91**, 1462 (1989)

3 A. Foord, J. G. Smith, and D.H. Whiffen, *Mol. Phys.* **29**, 1685 (1975)

4 B. Hegemann and J. Jonas, *J. Chem. Phys.* **79**, 4683 (1983)

5 Y. Morino, and T. Nakagawa, *J. Molec. Spectrosc.* **26**, 496 (1968)

6 E.A. Triaille, *J. Mol. Spectroc.* **18**, 118 (1965)

7 Alan C. Eckbreth, Gregory M. Dobbs, John H. Stufflebeam, and Peter A. Tellex, *Applied Optics.* **23**, 1328 (1984)

8 E.L. Schweitzer and J.I. Steinfeld, *Chem. Phys.* **108**, 343 (1986)

9 M.J. Shultz, L.M. Yam, and S.L. Berets, *Spectrochimica Acta*, **45A,** 1 (1989)

10 D.R. Siebert, F.R. Gradiner, and G.W. Flynn, *J. Chem. Phys.* **60**, 1564 (1974)

11 K.M. Beck, A. Ringwelski, R.J. Gordon, *Chem. Phys. Lett.* **121**, 529 (1985)

12 D. Proch and H. Schröder, *Chem. Phys. Lett.* **61**, 426 (1979)

13 T.B. Simpson and N. Bloembergen, *Optics Comm.* **37**, 256 (1981)

14 N. Bloembergen, I. Burak, E. Mazur, and T. Simpson, *Isreal J. of Chem.*, **24**, 179 (1984)

15 T. Simpson and N. Bloembergen, *Chem. Phys. Lett.*, **100**, 325 (1983)

16 M.H. Brooker and H.H. Wysel, *J. of Raman Spectroscopy*, **11**, 322 (1981)

17 R.D. Shelton, A.H. Nielson, and W.H. Fletcher, *J. Chem. Phys.* **21**, 2178 (1953)

CHAPTER 5

PULSED SUPERSONIC MOLECULAR BEAM SYSTEM

5.1 Introduction

Atomic and molecular beam methods play an important role in the history of quantum mechanics and chemical physics. Shortly after the first implementation of a molecular beam, Stern and Gerlach performed their famous experiment with a beam of silver atoms and demonstrated the existence of the electron spin in 1921. Since then, many more experiments have been performed in molecular beams to verify various aspects of quantum mechanics. Rabi used molecular beams to study magnetic resonance,[1] while Lamb used them to study the fine structure of the hydrogen atom and discovered the isotope and Lamb shifts.[2] Ramsey performed a series of experiments to study nuclear interactions in molecular beams.[3]

In 1951 Kantrowitz and Grey used a nozzle source and a skimmer to produce a supersonic beam.[4] This allowed them to improve the density in the beam by several orders of magnitude with respect to conventional effusive sources. A further advantage is the reduction of the random thermal molecular velocities, resulting in a narrower velocity distribution. In addition the internal degrees of freedom are cooled by collisions during the expansion. It has been shown that the excited rotational and vibrational states of molecules

are almost completely depopulated. Supersonic beams thus provide a high-density of molecules in a collision-free environment and in a well-defined distribution of internal states — an ideal system for scientific study.

In the past two decades, the progress in crossed molecular beam techniques has contributed to the study of chemical reactions.[5] Recent developments in molecular beam epitaxy (MBE) make possible deposition of complex multilayer thin films with monolayer resolution. This has opened up a new field of study involving artificial superlattices and multilayer semiconductor devices. All these progresses can be found in reviews[6,7] that provide details of theoretical and experimental studies, as well as applications of molecular beams.

In the section, fundamental aspects of supersonic beams are discussed. The design and calibration of a pulsed supersonic beam for the study of IRMPE is given in sections 5.3 and 5.4. Experimental results of CARS measurements on infrared multiphoton excited molecules in a pulsed supersonic beam are reported in the following chapter.

5.2 Thermodynamical description of a molecular beam expansion

The physics of the expansion of a gas in a molecular beam is best understood from a pV-diagram of isothermal and adiabatic processes as shown in Fig. 5.1. As the gas expands adiabatically from an initial state A at a high pressure p_o to a final state B at a much lower pressure $p_o/20$, the volume of the gas increases 20 times while the temperature decreases dramatically. For an ideal gas the adiabatic process intersects two isothermals at points A and B, yielding an effective cooling from 300 K to 12 K. This adiabatic cooling is the basic operating mechanism of compressors in refrigerators and air conditioners. For adiabatic process, the relation between the volume V and the temperature T is given by

$$V^{\gamma-1}T = \text{constant} . \tag{5.1}$$

Now, since $\gamma > 1$, T will decrease as the system expands.

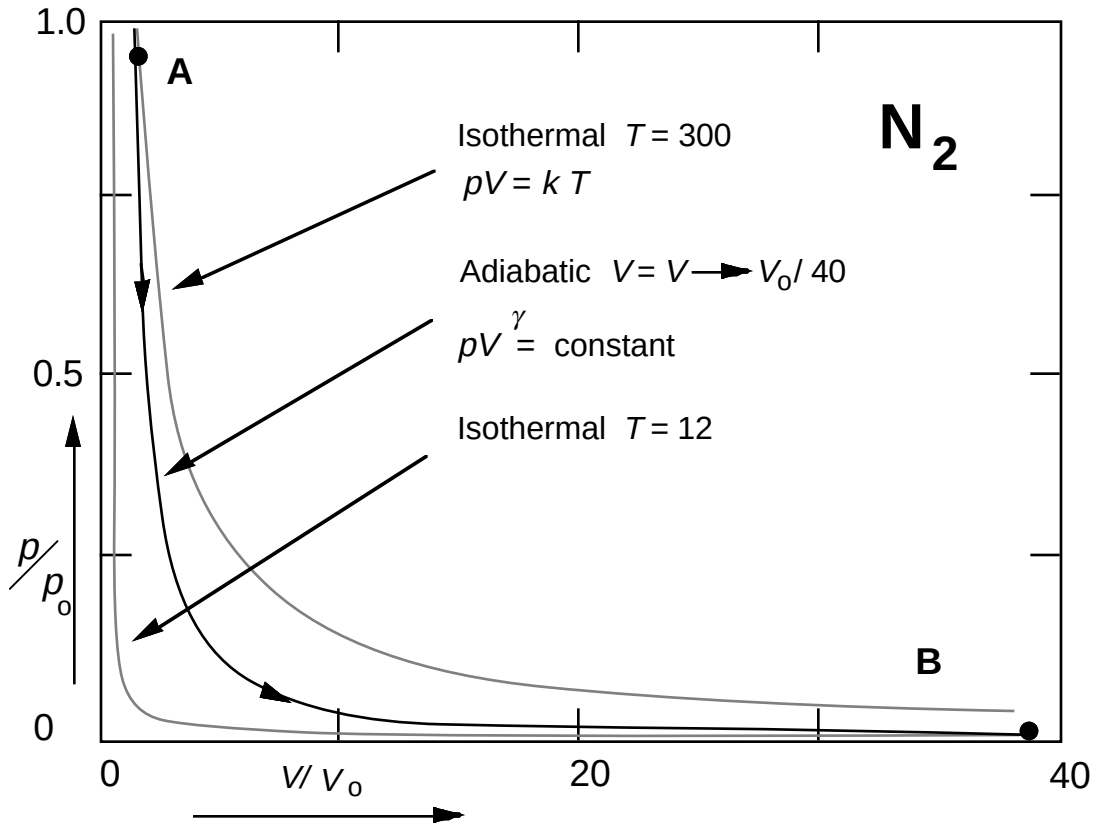

Fig 5.1. pV–diagram of adiabatic cooling. The dashed lines represent isothermal processes. The solid line is an adiabatic process in which the volume expands 20 times in going from state A to B. This results in a decrease in temperature from 300 to 12 K.

A schematic diagram of a molecular beam source is shown in Fig. 5.2. It consists of a high pressure reservoir at temperature T_o and pressure p_o, and an aperture leading to a low pressure region kept at a back pressure p_b. Depending on the values of the pressure p_o

and the diameter of the aperture D one distinguishes between *effusive* and *supersonic* beams. For an effusive beam,

$$D << l_o, \tag{5.2}$$

where l_o is the gas kinetic mean free path of molecules inside the reservoir. This condition ensures that there are no collisions in or beyond the pinhole and molecules inside the pinhole are not disturbed by the opening. As a result molecules in an effusive beam have nearly the same velocity distribution as inside the pinhole except that they can be skimmed into a beam by apertures down stream.

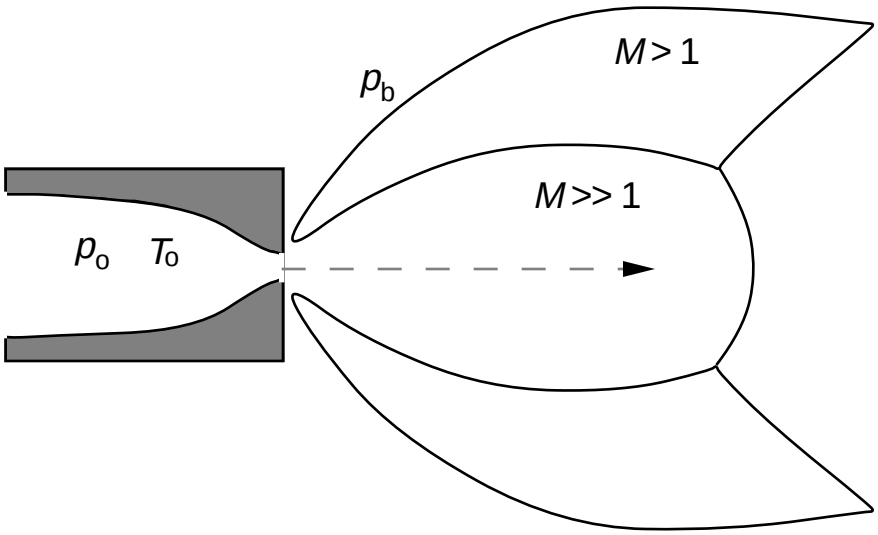

Fig. 5.2. Free expansion of a molecular beam from a nozzle. M is the Mach number, p_o the pressure and T_o the temperature in the reservoir, and p_b the back pressure.

For a supersonic beam, p_o is usually much higher and therefore the gas kinetic mean free path is much smaller, so that

$$D >> l_o, \tag{5.3}$$

and the expansion becomes a hydrodynamic flow. Not only is the beam highly directional but the width of the velocity distribution is much reduced. The term 'supersonic' is somewhat misleading because one associates it with molecules travelling much faster after the expansion. In reality, the gain in speed druing the expansion is not more than a factor of two. On the other hand the velocity of sound decreases dramatically due to the decrease in translational temperature. Therefore the speed of molecules exceeds the sound velocity in the beam and becomes *supersonic at the reduced temperature*.

The expansion and cooling mechanism of a supersonic beam can be described quantitatively as follows. We ignore viscosity and heat conduction effects to the wall and assume that the expansion of the gas is adiabatic, *i.e.*

$$đQ = T\,dS = 0, \tag{5.3}$$

where $đQ$ is the heat added to the system and S the entropy of the system. From (5.3) and the first law of thermodynamics,

$$dU = đQ - dW, \tag{5.4}$$

one has

$$dU = -dW = -pdV\,. \tag{5.5}$$

Thus it follows that the total enthalpy $H = U + pV$ is conserved during the adiabatic expansion process

$$U_f + p_f V_f = U_i + p_i V_i \,, \tag{5.6}$$

During the expansion, part of the initial enthalpy H_o of the molecules is converted into kinetic energy of the directed mass flow $mu^2/2$, where u is the average velocity of molecules in the direction of expansion (u_o= 0 in the high pressure stagnation region). The remaining enthalpy H is attributed to the enthalpy of molecules in the center of mass frame moving along with the beam at velocity u. Thus one can write

$$H_o = H + mu^2/2. \tag{5.7}$$

On the other hand one has

$$dH = C_p \, dT, \tag{5.8}$$

where C_p the specific heat at constant pressure. For an ideal gas, the specific heat can be expressed as

$$C_p = \frac{\gamma}{(\gamma - 1)} R \,, \tag{5.9}$$

with $\gamma = C_p/C_v$, and R the molar gas constant. Equations (5.7) and (5.8) allow us to obtain a relation between the velocity and the translational temperature of the gas before and after expansion

$$mu^2 = 2\,(H - H_o) = 2 \int_T^{T_o} C_p \, dT \,. \tag{5.10}$$

Assuming that C_p is constant over the range of interest, one obtains

$$u = \sqrt{2C_p(T_o - T)/m} \,. \tag{5.11}$$

This equation provides a relation between the average velocity of the mass flow and the temperature decrease due to the expansion.

Conventionally supersonic expansions are described in terms of the Mach number

$$M = \frac{u}{v_s}, \tag{5.12}$$

with $v_s = \sqrt{\gamma RT/m}$ the sound velocity. Expressing the translational temperature T in (5.11) in terms of M, one obtains

$$\frac{T}{T_o} = \left\{ 1 + \frac{\gamma - 1}{2} M^2 \right\}^{-1}. \tag{5.13}$$

Typically the Mach number M ranges from 10 to 100 for helium in a supersonic beam. Thus a dramatic decrease in the translational temperature occurs. In a similar fashion the pressure can be expressed as

$$\frac{p}{p_o} = \left\{ 1 + \frac{\gamma - 1}{2} M^2 \right\}^{-\gamma/(\gamma-1)}. \tag{5.14}$$

Equations (5.13) and (5.14) show the cooling and expansion in a supersonic beam under the assumption of an adiabatic process and constant C_p and γ.

To obtain the Mach number for an expansion as a function of the distance x to the nozzle one can use the following empirical relation valid for $x/D > 2$,[8]

$$M = A(\gamma) \left\{ \frac{x - x_o}{D} \right\}^{\gamma-1} - \frac{\frac{1}{2}(\gamma+1)/(\gamma-1)}{A(\gamma) \left\{ \frac{x - x_o}{D} \right\}^{\gamma-1}}, \tag{5.15}$$

where the parameters A and x_o depend on γ. Experimentally determined values for these parameters are listed in Table 5.1.

γ	x_0/D	A
1.40	0.40	3.65
1.30	0.70	3.90
1.28	0.85	3.96
1.20	1.00	4.29
1.10	1.60	5.25
1.05	1.80	6.44

TABLE 5.1 Values of supersonic beam parameters A and x_0/D taken from Ref. 8.

The reduction in translational temperature will transfer to rotational and vibrational degrees of freedom via inelastic collisions during and after the expansion. Since vibrational cooling requires a much larger energy exchange than rotational cooling, the cross-section for vibrational energy transfer during a collision is much smaller than the one for rotational energy transfer. So, while the translational temperature can be around 1 K after expansion, typical values for the vibrational and rotational temperature are 100 K and 10 K, respectively.

To illustrate the effect of the internal degrees of freedom on the cooling of a supersonic beam, the translational temperature is plotted as a function of x/D in Fig. 5.3 using Eqs. (5.13) and (5.15) for N_2 and for SF_6. Since SF_6 has 15 more internal degrees of freedom than N_2, the cooling is much more pronounced for the smaller N_2 molecules.

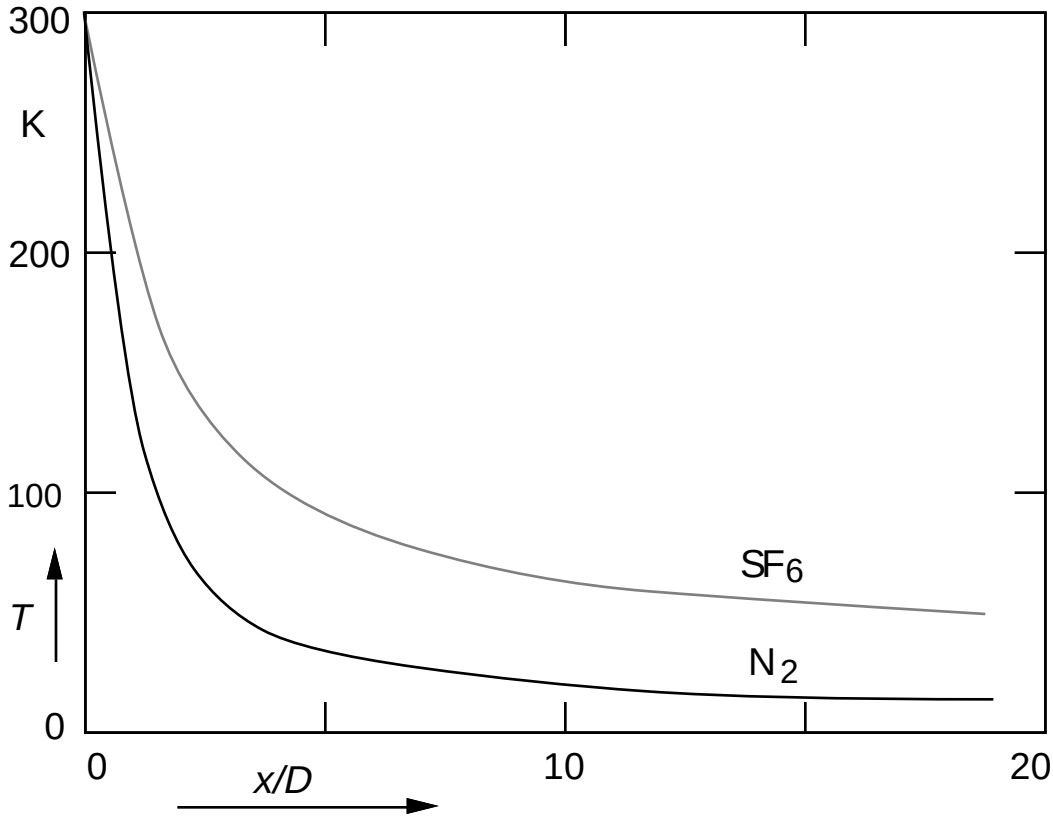

Fig. 5.3. Decrease in translational temperature during a supersonic expansion as calculated from Eqs. (5.13) and (5.15) with $\gamma = 1.4$ and $\gamma = 1.1$ for N_2 and SF_6.

The decrease in translational temperature will result in a reduction in the number of collisions between molecules in the beam. For an isentropic flow, the collision rate in a supersonic beam is[9]

$$R = \sqrt{2}\, n_o \sigma v_o \left\{ 1 + \frac{\gamma - 1}{2} M^2 \right\}^{-(1/2)(\gamma+1)/(\gamma-1)}, \qquad (5.16)$$

where n_o is the density of molecules in the reservoir, σ the gas-kinetic collisional cross section, and v_o the mean velocity of the molecules in the reservoir. Since $R_o = \sqrt{2}\, n_o \sigma v_o$ is

the collision rate in the reservoir, Eq. (5.16) shows the evident decrease in collision rate after expansion.

The ideal-gas description of the adiabatic expansion given above is only an approximation of the situation for a real molecular beam. For instance, due to the internal degrees of freedom, C_p and γ depend on the temperature. This makes it difficult to derive analytical expressions for the temperature and density. Therefore one usually resorts to empirical methods such as the method of characteristics,[10] which goes beyond the scope of this section. The basic mechanism of the adiabatic cooling of a real gas in a supersonic molecular beam, however, is the same as for an ideal gas and the equations given above provide a reasonable first order approximation to the real situation.

The cooling is greatly reduced for large molecules with many internal degrees of freedom and a value of γ close to 1. If $\gamma = 1$ the curves for adiabatic and isothermal process in Fig. 5.1 overlap and no cooling occurs, as can also be seen from Eq. (5.13). This problem can be overcome by *seeding* the beam with helium or argon. The translationally cooled seeding gas atoms then collide with the larger molecules and effectively cool them down. Even without seeding, however, a certain cooling is observed for large molecules. This occurs because most vibrational modes and even some rotational modes have a negligible excited state population at the initial temperature. Therefore these modes do not play a role in the cooling process and the molecule behaves more like an ideal gas. For SF_6, for example, the specific heat ratio γ has been reported to range between 1.1 and 1.3 depending on the experimental conditions.[11]

A final remark regarding the molecular density is in order. In the beam the density of molecules is much smaller than typical bulk densities, which can lead to low signal for spectroscopic studies. However, the effective cooling in the internal degrees of freedom increases the population of individual states, thereby increasing the signal level. This is

especially important in CARS studies, where the signal is proportional to the square of population difference as was shown in chapter 2.

5.3 Setup

The pulsed supersonic molecular beam apparatus consists of a nozzle mounted on an *XYZ* translational manipulator and a high vacuum chamber. The nozzle, shown in Fig. 5.4, is a modified Toyota cold start fuel injector (model No. 23260-79055). The modification consists of machining off the fuel injection nozzle to a thickness of about 2 mm. The diameter of the output aperture is 0.9 mm. The pressure in the reservoir is between 1 and 3 atm. The nozzle is driven by a custom built electronic driver at a rate of 10 Hz with a variable openening time of 0.1 to 1 ms. Details of the driver circuit can be found in Appendix A.

The beam chamber pumping system consists of an Edwards E2M12 rotary pump and an Edwards MK2 700-liter/s diffusion pump. With the molecular beam off, the beam chamber pressure is 4×10^{-7} Torr; with a reservoir pressure of about 3 atm and 1-ms molecular pulses at a 10-Hz repetition rate, the chamber pressure increases to 7×10^{-4} Torr.

The beam expands vertically downward into the high vacuum chamber, which has four windows allowing CARS probing and infrared laser pumping for the study of infrared multiphoton excitation. The *XYZ* translational manipulator allows one to overlap the molecular beam with laser beams and to adjust the distance *x* between the nozzle and the interaction region.

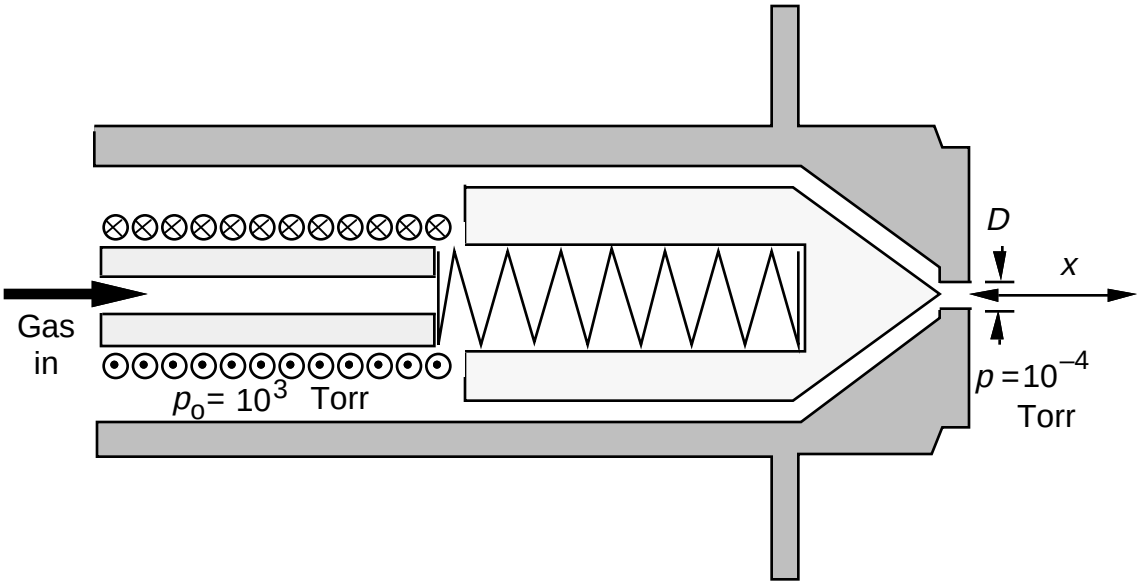

Fig. 5.4. Configuration of the pulsed supersonic nozzle. The diameter *D* of the aperture is 0.94 mm.

5.4 Calibrations

The calibration of the temperature and density in the supersonic beam can be performed easily using the pure rotational CARS technique described in section 2.6. The pure rotational CARS spectrum of nitrogen at room temperature is shown in Fig. 5.5. The number *J* represents the Raman transition between *J* and (*J*+2) rotational state, where *J* is the rotational quantum number, and the $\Delta J = 2$ stems from the rotational Raman selection rules. The CARS signal is related to the square of the population difference between the *J* and *J*+*2* states[12]

$$\frac{Ng_J(2J+1)}{Z_R}\left\{e^{-J(J+1)B/kT} - e^{-(J+2)(J+3)B/kT}\right\}, \qquad (5.11)$$

where N is the number density of Raman active molecules, g_J the nuclear spin statistical weight, Z_R the rotational partition function, and B the rotational constant. Equation (5.11)

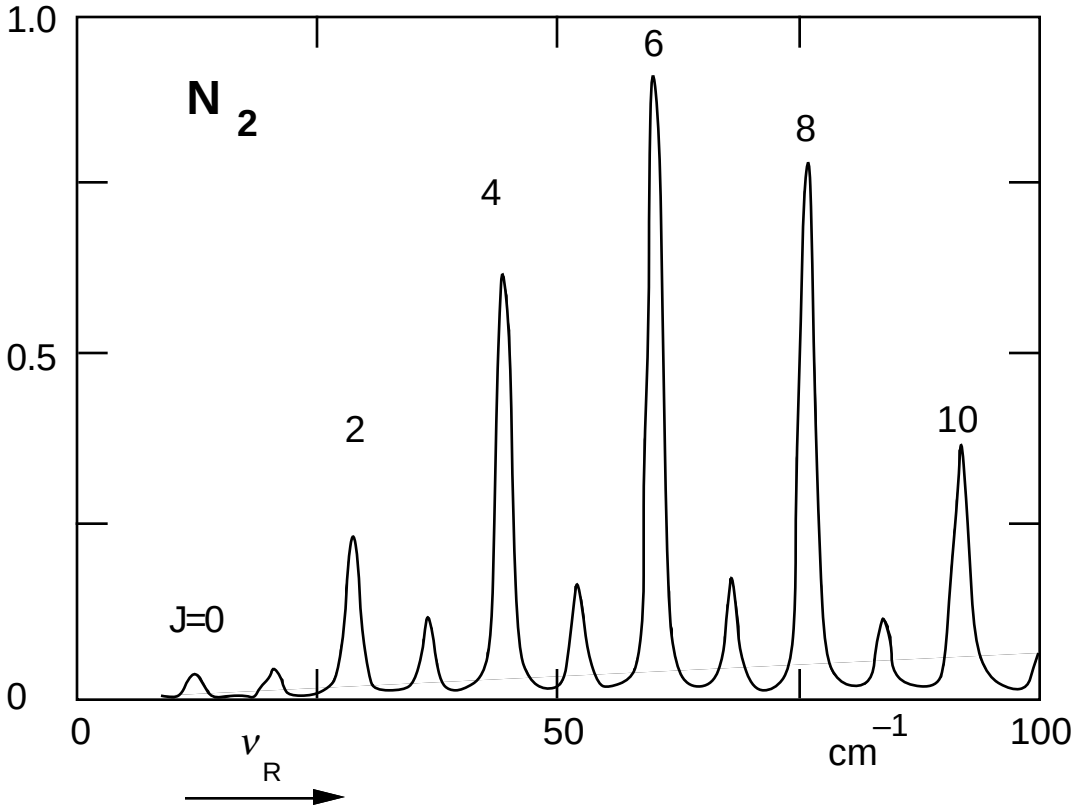

Fig. 5.5. Pure rotational CARS spectrum of N_2 at room temperature. The label J labels the rotational quantum number of the initial Raman transition. Because the population of even and odd J states have a nuclear spin weight ratio of 2, the spectrum shows an alternating intensity distribution.

can be used to evaluate the rotational temperature of the molecules from measured pure rotational spectra such as the one shown in Fig. 5.5. Since the rotational constant of

nitrogen is well known (B = 2.010 cm^{-1}), the nitrogen rotational CARS spectrum can be used to calibrate the Raman shift of other spectra.

In the pulsed supersonic beam, the distribution of rotational states reduces dramatically. As shown in Fig. 5.6, at a distance x/D = 5.2 from the nozzle, only states with $J \leq 4$ are populated. This corresponds to a rotational temperature of 30 K.

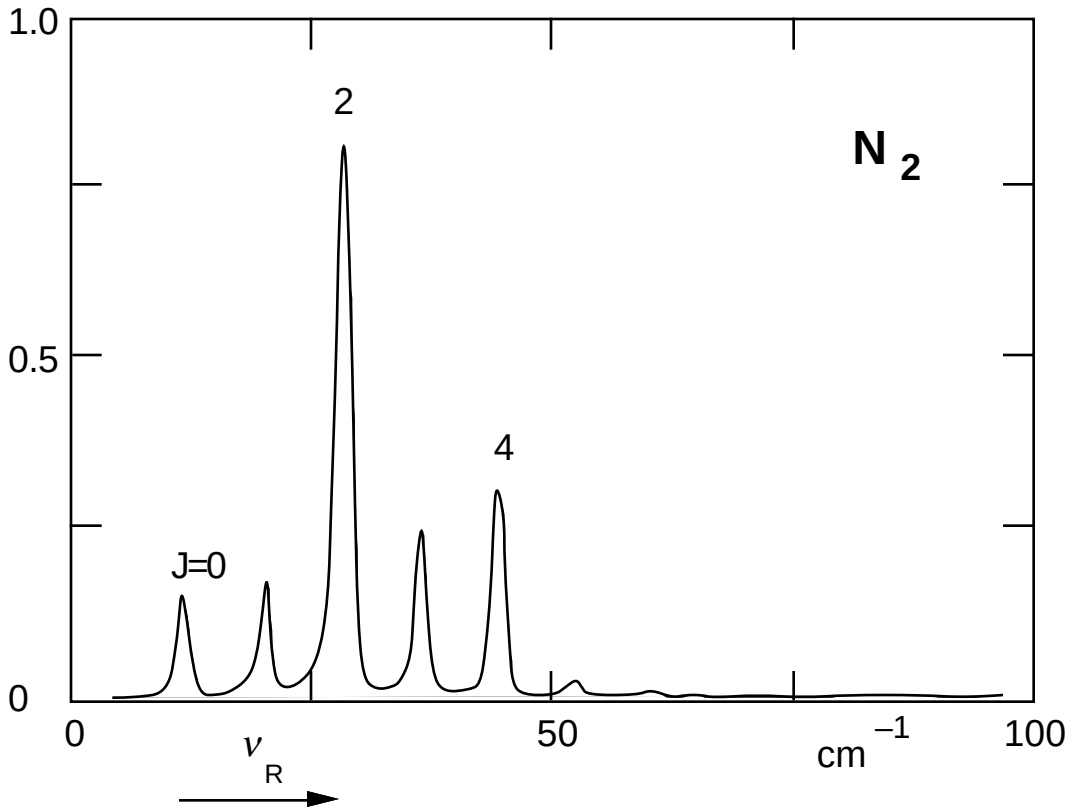

Fig. 5.6 Pure rotational CARS spectrum of N_2 in a pulsed supersonic beam at x/D = 5.2. This spectrum corresponds to a rotational temperature of 30 K.

Still further away from the nozzle, at x/D = 11.6, the cooling is even stronger and only states with $J \leq 2$ appear, see Fig. 5.7. A fit according to Eq. (5.1) indicates a rotational temperature of 10K. Notice that even at 0 K the J = 1 state still would have a 33% population due to the ortho and para modifications of N_2.[13]

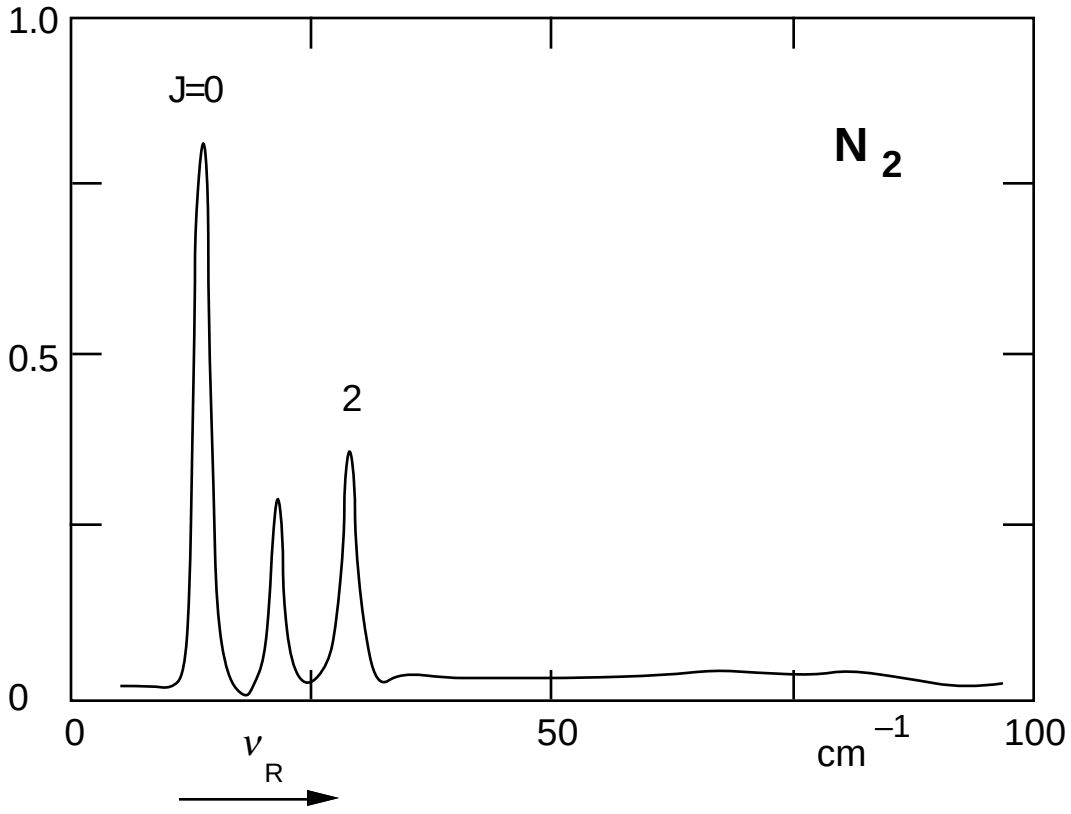

Fig. 5.7. Pure rotational CARS spectrum of N_2 in a pulsed supersonic beam at x/D = 11.6. This spectrum corresponds to a rotational temperature of 10 K.

The density in the supersonic beam was determined by comparing the pure rotational CARS spectra from molecules in the bulk with the one obtained in the beam. Taking the square root of each line J in the spectrum one obtains $C\Delta N_J$, a quantity

proportional to the population difference between the J and J+2 states. From the sum of CN_J over all rotational states J, one obtains CN, which is proportional to the total number of molecules in the interaction region. If one switches witching between sample gases in the bulk and in the beam without changing the alignment or gain of the detector array, the proportionality constant C remains the same. This allows one to determine the density in the beam by comparing CN obtained in the beam with the CN* obtained in the bulk at a number of pressures. For nitrogen, at x/D = 4.5, the density in the jet was found to be 6×10^{23} m^{-3} equivalent to a bulk density at 2 Torr.

For molecules with a rotational constant B smaller than 0.1 cm^{-1} the rotational CARS spectrum is not resolvable in the current apparatus. In this case the method described above cannot be applied. Instead, one can use vibrational CARS and compare the integrated intensity of the ground state peaks. However, for identical molecular densities in beam and bulk, the signal obtained in the beam will be of higher intensity than the one in the bulk. This is so because the molecules in the beam have narrower rotational distribution than those in the bulk. Thus with the vibrational CARS method one can only obtain an upper limit for the density in the beam .

5.5 Conclusion

The fundamental aspects of a supersonic expansion and the setup and calibration methods for a pulsed supersonic beam were discussed in this chapter. Using the pure rotational CARS technique, we demonstrated the effective rotational cooling during the expansion of N_2 in the beam. The translational degree of freedom is cooled more strongly than the rotational one. This decrease in temperature and density results in a dramatic reduction of the collision rate in the beam.

With this supersonic beam aparatus, one can study molecules at lower temperatures and with fewer collisions. This is a key factor for the study of infrared multiphoton excitation.

References

1 I. Rabi, S. Millman, and P. Kush, *Phys. Rev.* **55**, 526 (1939)

2 W.E. Lamb, JR. and R.C. Retherdord, *Phys. Rev.* **79**, 549 (1950); **81**, 333 (1951); **85**, 259 (1952); **89**, 98 (1953)

3 N.F. Ramsey, *Molecular Beams.* (Oxford Press 1956)

4 A. Kantrowitz and J. Grey, *Rev. Sci. Instr.* **22**, 333 (1951)

5 Y.T. Lee and B. Bunsenges, *Phys. Chem.*, **86**, 378 (1982)

6 J.B. Anderson, in *Molecular Beams and Low Density Gas Dynamics*, P.P. Wegener Ed., (Dekker, New York 1974)

7 G. Scoles, D Bassi, U. Buck, and D. Laine Edits, *Atomic and Molecular Beam Method*, Vol I, (Oxford Press, New York, 1988)

8 J.B. Anderson, *AIAA Journal*, **10**, 112 (1969)

9 D.M. Lubman, C.T. Rettner, and R.N. Zare, *J. Phys. Chem.*, **86**, 1129 (1982)

10 E. Bectke, *Gas Dynamics*, (Academic Press, New York, 1968)

11 P.N. Bajaj and P.K. Chakraborti, *Chem. Phys.*, **104**, 41 (1986)

12 J.A. Shirley, R.J. Hall, and A.C. Eckbreth, *Opt. Lett.*, **5**, 380 (1980)

13 G. Herzberg, *Spectra of Diatomic Molecules*, Vol. 1 (Van Nostrand Reinhold, New York, 1950)

CHAPTER 6

INFRARED MULTIPHOTON EXCITATION IN A SUPERSONIC MOLECULAR BEAM

6.1 Introduction

The experiments on OCS and SO_2 reported in chapter four provide information on the dynamics of infrared multiphoton excitation and relaxation in these molecules. The CARS technique used in those experiments has a high resolution, a strong signal level, and allows one to obtain state-specific information on the infrared multiphoton excitation process. As described in chapter five, the supersonic beam method provides molecules which are internally cooled and which undergo virtually no collisions. Both of these points considerably facilitate the interpretation of the infrared multiphoton excitation experiments. This chapter reports the results of a combination of the CARS and supersonic beam techniques applied to the study of infrared multiphoton excitation.

The measurements described in this chapter were carried out with the molecular beam apparatus described in section 5.3. The CARS spectrograph used is the one described in the preceding chapters. A Laser Science Model PRF-150 CO_2 laser was employed to generate 250-mJ pulses with 10-Hz repetition rate and synchronized with the CARS laser pulses. The CO_2 laser pulses have a 150-ns FWHM pulse duration with a microsecond

long tail due to energy transfer from metastable nitrogen. This tail, which is common to CO_2 lasers, causes difficulty in the interpretation of the experimental results such as the slow rise of the OCS temperature reported in chapter four. To avoid this problem the tail of the infrared pulse was cut off with a self-triggered plasma shutter. The resulting CO_2 laser pulses have a slow 20-ns rise time and a fast picosecond fall time. The overall duration of the pulses does not exceed 60 ns. Measurements were carried out on C_2H_4, OCS and SF_6.

6.2 Pure rotational CARS of ethylene

Each vibrational line in the CARS spectra shown in chapter four comprises many rotational lines that carry information about the rotational degrees of freedom. Because the rotational lines in a *Q*-branch Raman peak lie extremely close to one another, the rotational structure cannot be resolved using the standard multiplex vibrational CARS technique. It may be possible to resolve this structure using a scanning narrow band dye laser. Another more convenient way to obtain rotational information is the pure rotational CARS technique described in chapters two and five. Since the separation between peaks in rotational CARS spectra is 4*B*, the spectra are not as congested and can be resolved for molecules for which $B > 0.1\ \text{cm}^{-1}$.

To study the role of rotational states in infrared multiphoton excitation, one needs a molecule that absorbs radiation on one of the CO_2 lines and that has a rotational spectrum that can be resolved by the multiplex CARS apparatus. One such molecule is C_2H_4. In this section changes in the rotational spectrum of ethylene after infrared multiphoton excitation are studied by pure rotational CARS.

Ethylene is an asymmetric top molecule that is nearly symmetric top. In general the rotational Raman spectra of asymmetric top molecules are difficult to analyze because of the many rotational degrees of freedom that cause large numbers of overlapping lines to appear

in the spectrum. The selection rules for rotational Raman transitions of asymmetric top molecules are[1]

$$\Delta J = 0, \pm 1, \pm 2, \quad \Delta K = 0, \tag{6.1}$$

where J and K are the rotational quantum numbers corresponding to the angular momentum vector $\boldsymbol{J}$ and its projection on the figure axis of the molecule.

Ethylene has three rotational degrees of freedom. The rotation along the C=C axis has the largest rotational constant, but a small Raman cross section. The other two rotational degrees of freedom have nearly identical rotational constants, making it difficult to resolve the spectrum by conventional Raman spectroscopy. There are four branches in the rotational Stokes spectrum[2] as listed in Table 6.1.

Branch	Transition	Specification
R	$\Delta J = 1$	Symmetric top part
S	$\Delta J = 2$	Symmetric top part
R^*	$\Delta J = 1$	Contribution from deviation from symmetric top
S^*	$\Delta J = 2$	Contribution from deviation from symmetric top

Table 6.1 Specification of the four branches in the rotational Raman spectrum of ethylene.

The pure rotational CARS spectrum of ethylene in the bulk is shown in Fig. 6.1. The individual lines are clearly resolved and can be assigned to the four branches listed in table 6.1. By blocking the strong laser background at zero Raman shift using a thin wire placed in front of the detector array, one can easily observe both CARS and CSRS spectra. Fig. 6.2 shows such a spectrum for ethylene after expansion in the supersonic beam at x/D = 5.7. As can be seen, the rotational distribution of ethylene reduces to low J

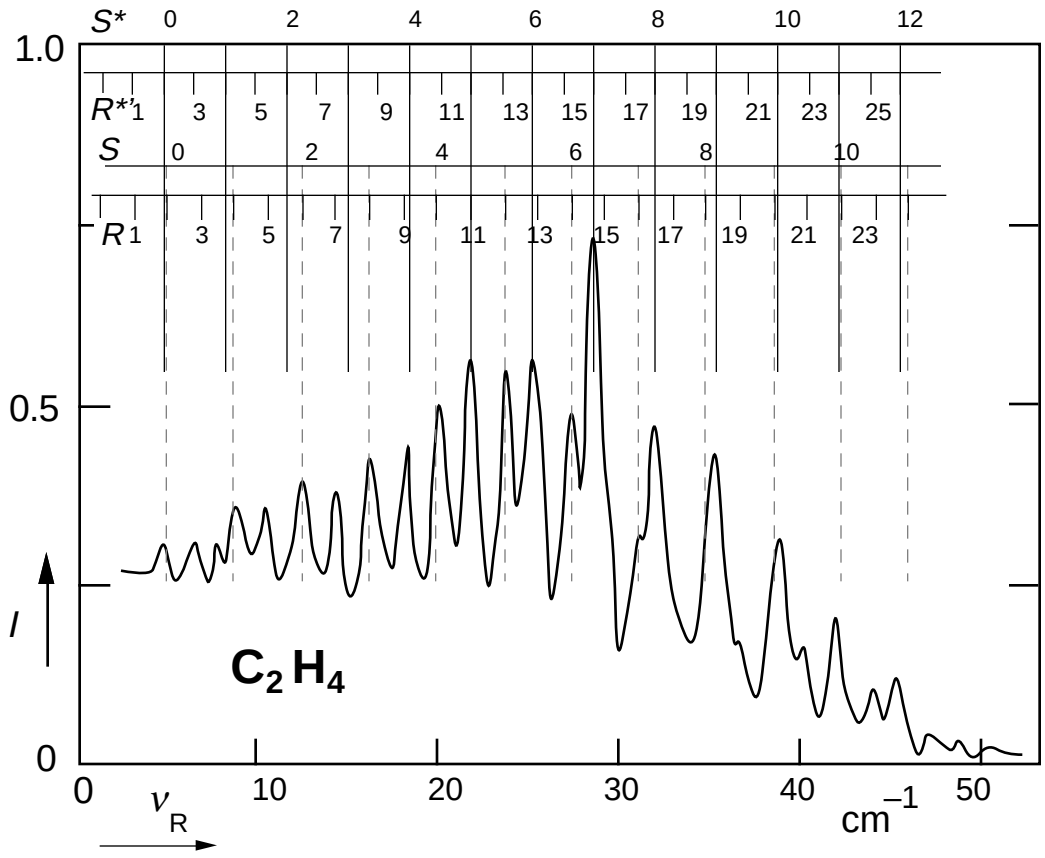

Fig. 6.1. Pure rotational CARS of ethylene in the bulk with a pressure of 30 Torr. The assignment of *S*, *R*, *S'*, and *R'* branches are described in Table 6.1.

values. The spectrum becomes easier to assign because one can directly compare the Stokes and anti-Stokes lines instead of using the position of the laser frequency to determine the Raman shift. This allows one to determine the rotational constants for ethylene in a straight forward fashion.

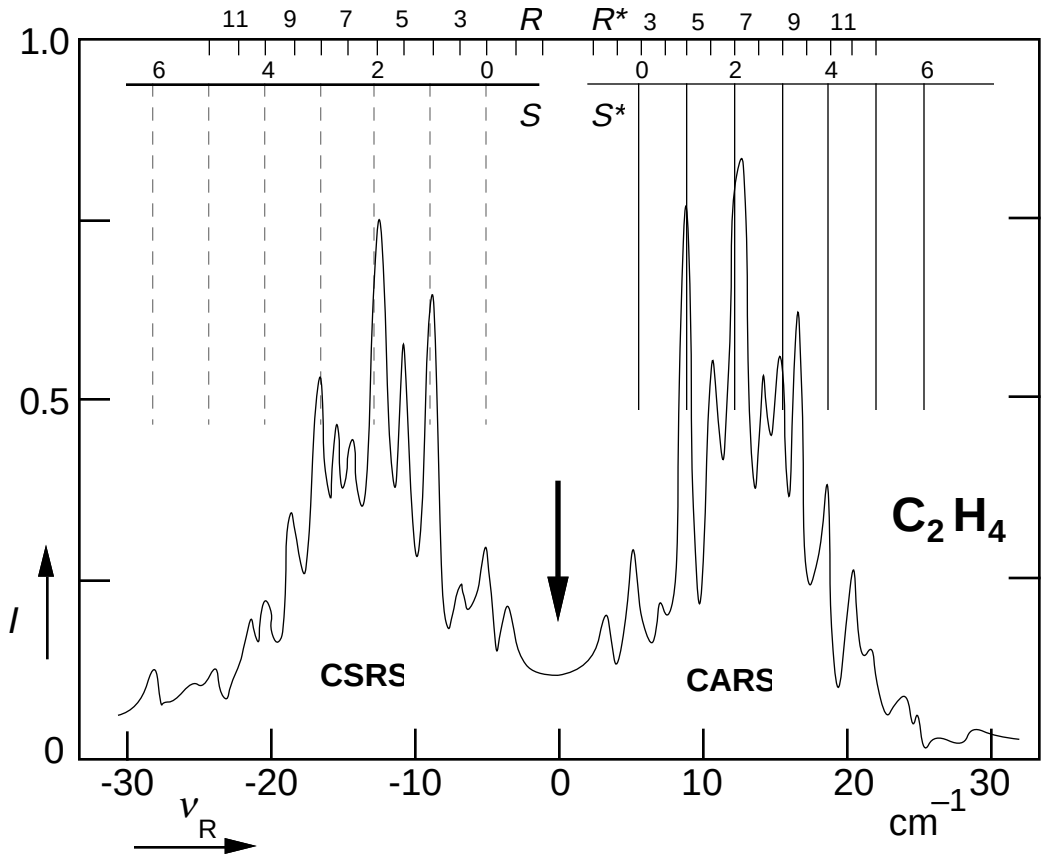

Fig. 6.2. Pure rotational CARS and CSRS of ethylene in the beam at x/D = 5.7. The arrow indicates the laser wavelength. Notice that all four S, R, S^*, R^* branches appear in each of the CARS and CSRS spectra. In this figure, S and R branches are assigned in the CSRS spectrum while S^* and R^* branches are assigned in the CARS spectrum to avoid difficulty in reading.

The rotational constants obtained from the spectra in Figs. 6.1 and 6.2 are $\tilde{B} = \frac{1}{2}(B+C) = 0.92 \pm 0.01$ cm^{-1} and $C = 0.83 \pm 0.01$ cm^{-1}. For planar molecules the moments of inertia I about the three principal axes of rotation satisfy the relation[1]

$$I_C = I_A + I_B \,, \tag{6.2}$$

where the subscript A labels the figure axis. The rotational constants are related to the moments of inertia by

$$A_i = \frac{h}{8\pi^2 I_{A_i}} \qquad (A_i = A, B, C). \tag{6.3}$$

Equations (6.2) and (6.3) allow one to determine the three rotational constants from the values of $\tilde{B}$ and C. The resulting values listed in table 6.2 are in excellent agreement with published values.[3]

	A (cm^{-1})	B (cm^{-1})	C (cm^{-1})
This work	4.66 ± 0.02	1.01 ± 0.01	0.83 ± 0.01
Ref. 3	4.828	1.0012	0.8282

Table 6.2. Comparison of the obtained C_2H_4 rotational constants with published values.

To study the effect of infrared excitation on the rotational spectrum, the ν_4 mode of the ethylene molecules was pumped with the 9P14 CO_2 laser line. The result is shown in

Fig 6.3, where the dashed line shows the spectrum without infrared pumping and the solid one the spectrum 250 ns after an infrared pulse of 6.3 J/cm^2. The lines corresponding to the $J = 1$ and $J = 2$ states are strongly reduced in intensity by the CO_2 laser, indicating a strong depletion in the corresponding rotational states.

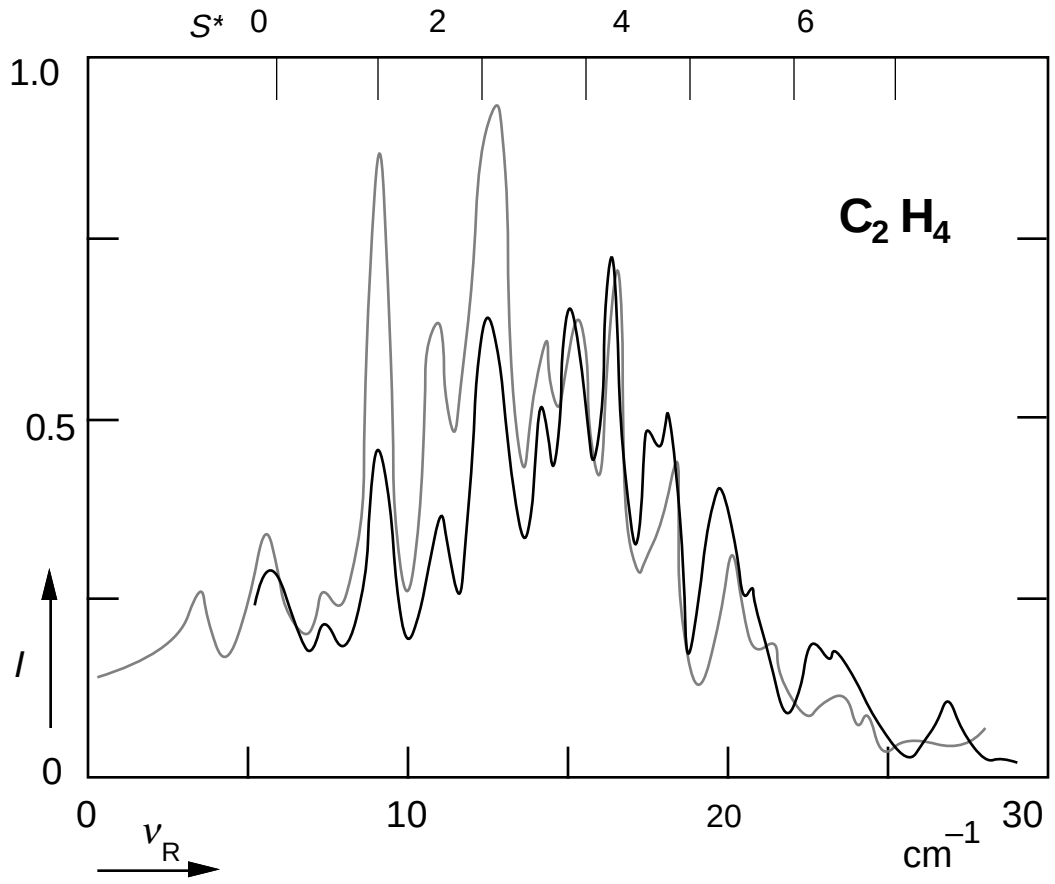

Fig 6.3. Pure rotational CARS spectra of ethylene in the beam at x/D = 5.7, without infrared excitation (dashed line) and with 9P14 CO_2 laser excitation (solid line).

For excitation at a different CO_2 laser lines, one expects to observe a change in the rotational lines that are depleted. Indeed, as the laser is switched to the 9P10 line, the

spectrum changes to the one shown in Fig. 6.4. Now the $J = 2$ and $J = 3$ states are considerably depleted, indicating infrared pumping of these rotational states.

Note that the measurements shown in Figs. 6.2 and 6.3 show a population depletion of more than one rotational level. This is a strong indication that rotational hole filling still occurs in the beam.

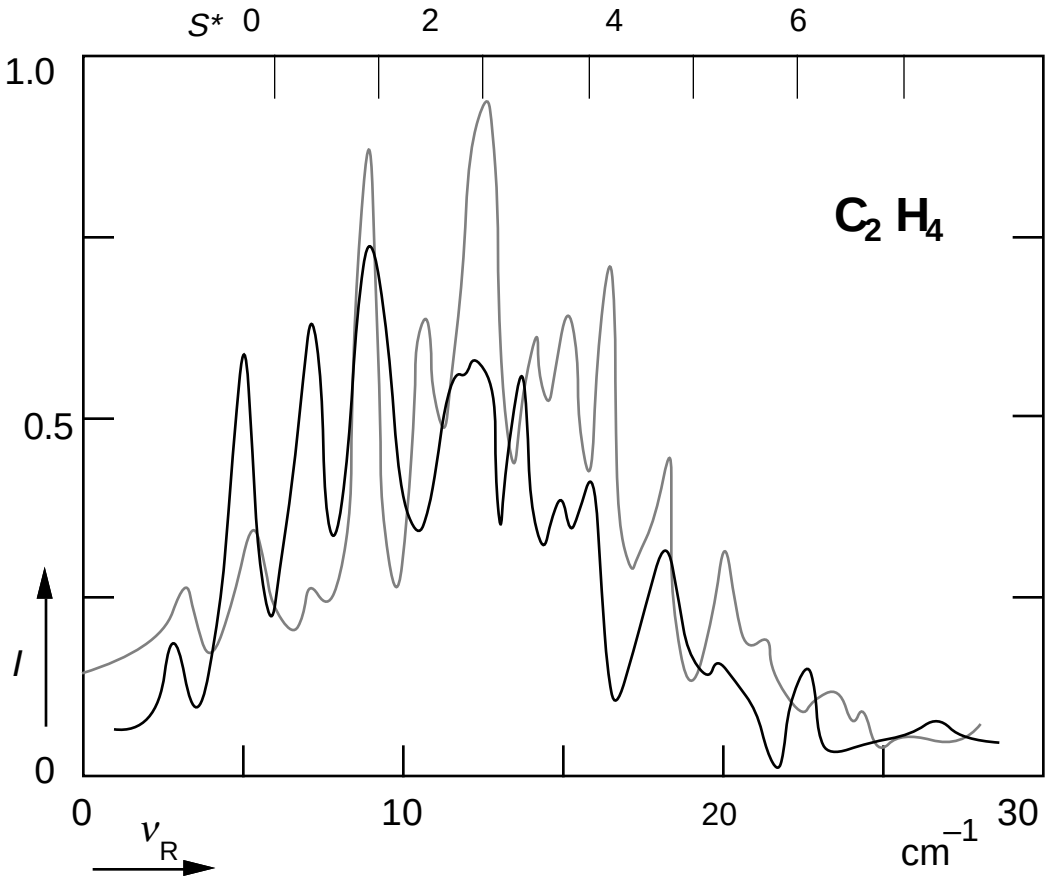

Fig 6.4. Pure rotational CARS spectra of ethylene in the beam at $x/D = 5.7$, without infrared excitation (dashed line) and with 9*P*10 line CO_2 laser excitation (solid line).

6.3 IRMPE of OCS in the beam

As was shown in chapter four, the distribution among the ν_2 vibrational states of infrared multiphoton excited OCS is always nearly Boltzmann even though the CO_2 laser excites only the even overtone states. This is a result of a fast collisional relaxation which quickly redistributes and equilibrates the energy absorbed by the even states. In a supersonic beam the collision rate is much reduced allowing one to observe the distribution immediately after infrared excitation *before* collisions determine the distribution.

A spectrum obtained in the beam at a distance x/D = 2.6 and 200 ns after a 7.2 J/cm^2 9P22 CO_2 laser line excitation is shown in Fig. 6.5. At this distance the estimated density is about 10 Torr. Compared with the spectra obtained in the bulk (see Fig. 4.5), the peaks in Fig 6.5 are narrower indicating cooling of the rotational degrees of freedom. Fewer rotational states being populated results in more population in each individual state. Since the CARS intensity of proportional to the square of the population difference in each state, rotational cooling contributes to the higher signal level in the beam than in the bulk of the same density. Also, the overall excitation is reduced because of the reduction in collisionally assisted excitation. Nevertheless, odd-numbered states are still populated. This is so because even at a distance x/D = 2.6 in the beam collisions still occur.

To investigate the role of collisions in the excitation of OCS in the beam, the fraction f of excited molecules was measured as a function of distance x. This fraction is defined as

$$f = 1 - \frac{N_o}{N}, \tag{6.2}$$

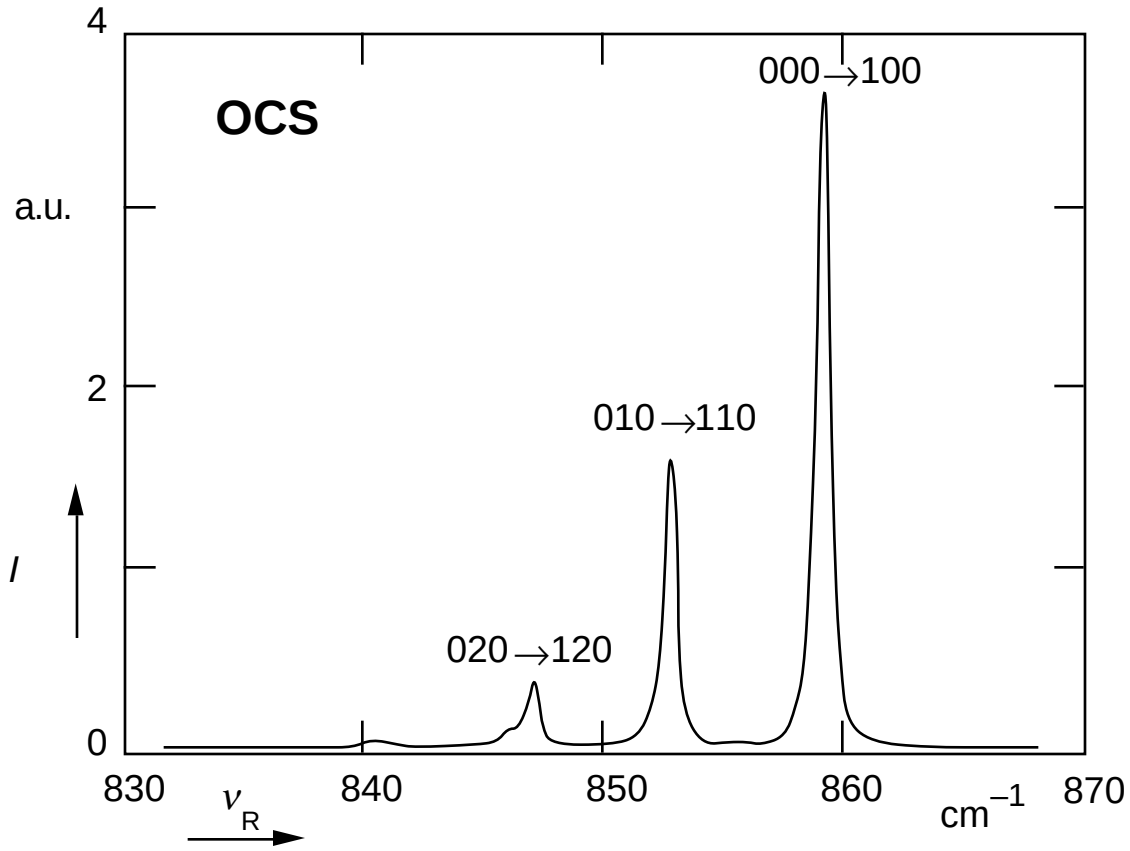

Fig. 6.5. Vibrational CARS spectrum of OCS in a supersonic beam at x/D = 2.6, 200 ns after 7.2-J/cm^2 9P22 CO_2 laser line excitation .

where N_0/N is the fraction of molecules remaining in the ground vibrational state, which can be determined from the intensity of the fundamental peak in the CARS spectrum. Measured values of f versus x/D are plotted in Fig. 6.6. As the distance x to the nozzle is increased, the excitation decreases because of the reduced collision rate. Clearly, for distances x/D < 3.8 collisions still contribute to the excitation even in a supersonic expansion. At larger distances, however, the excitation no longer decreases and levels off at about 10%. In this regime collisions no longer contribute to the excitation and the remaining 10% of excited molecules are excited under true *collisionless* conditions.

A spectrum obtained under these conditions (x/D = 3.8) at a delay of 30 ns is shown in Fig. 6.7. As expected, the spectrum only shows a single peak corresponding to the excited overtone transition. The population of the excited overtone state (020 → 120) is

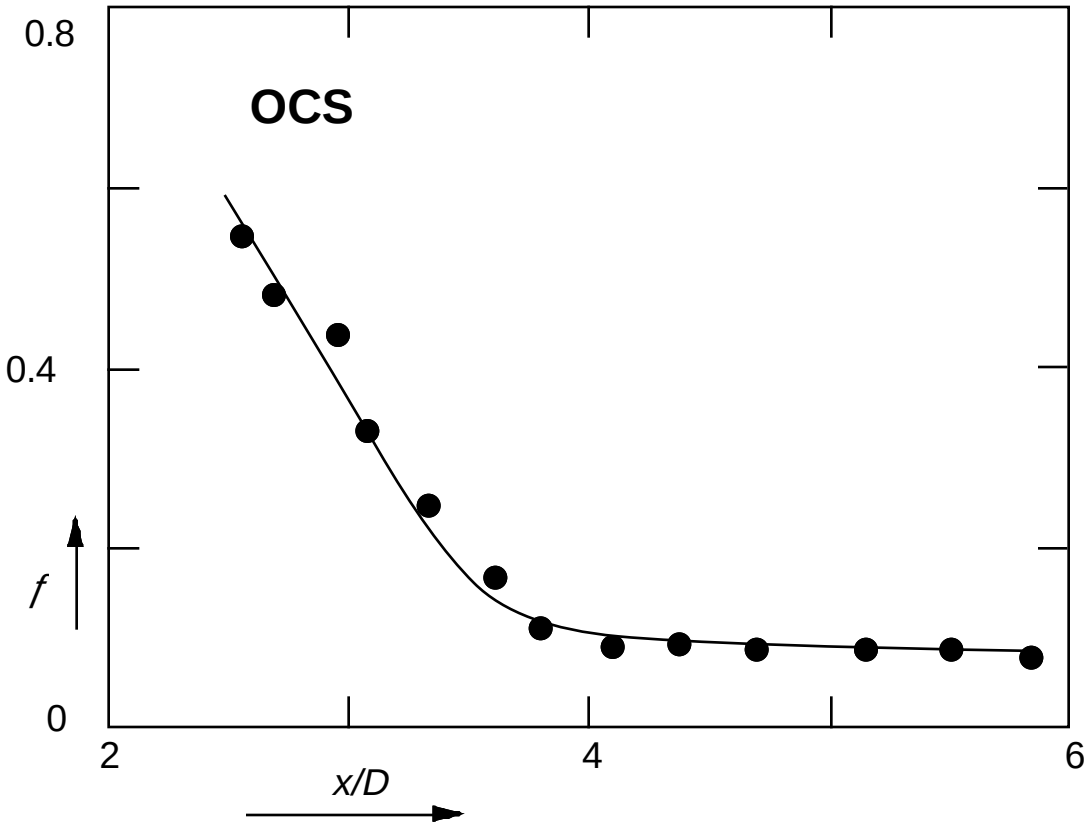

Fig. 6.6. Decrease in infrared excitation as x/D increases. In this figure $f = 1 - \frac{N_0}{N}$ as defined in Eq. 6.2. At $x/D > 3.8$, the excitation remains constant, indicating that in this region collisions no longer contribute to the excitation

much smaller than the ground state population (000 → 100), which is moved off the right edge of the detector array to prevent saturation.

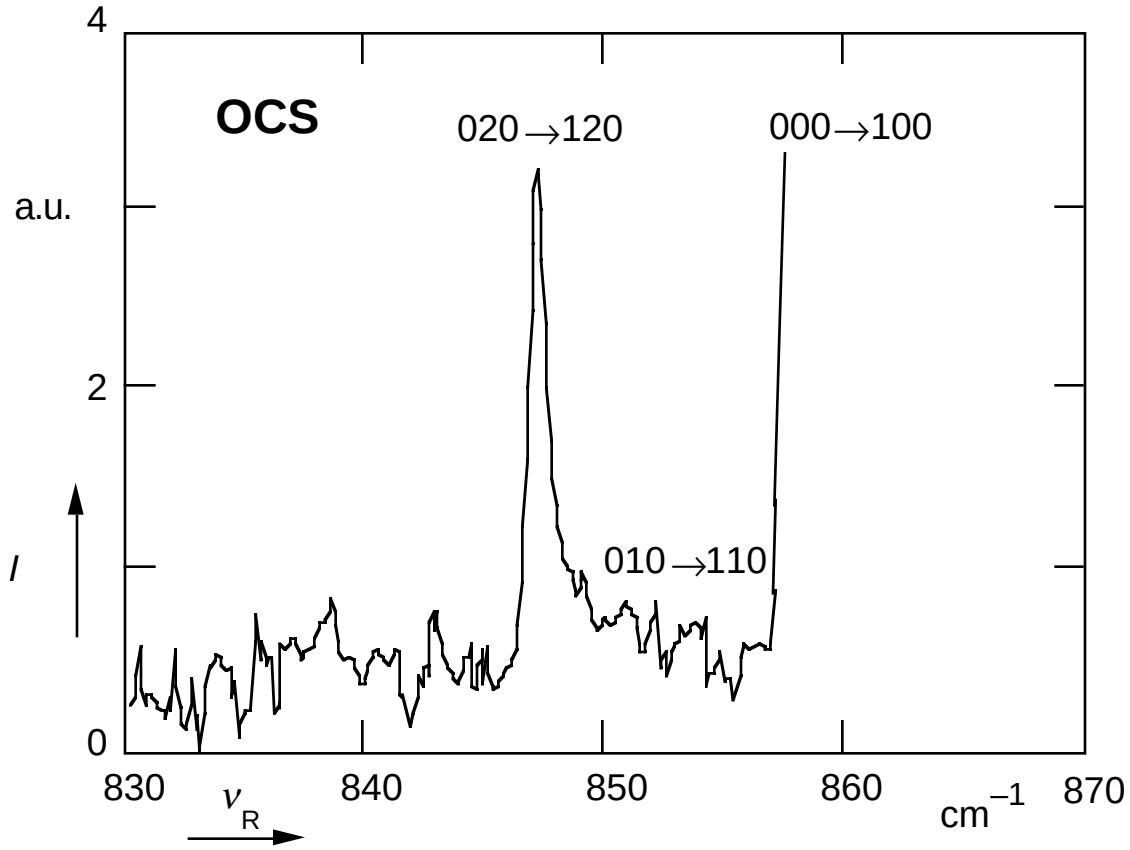

Fig. 6.7. CARS spectrum of OCS in a supersonic beam at 30 ns after 7.2-J/cm^2 infrared excitation, at x/D = 3.8.

The time-evolution of this spectrum is shown in Figs. 6.7 through 6.9. At a delay of 60 ns the v_2=1 state begins to be populated because of collisional relaxation. For longer times the intensity of the (010)→(110) peak continues to grow and the population of the odd states continues to grow toward equilibrium.

The observation of collisional relaxation within the ν_2 mode allows one to determine the energy transfer rate within this mode provided the collision rate is known. By comparing CARS measurements in the bulk with measurements in the beam at x/D = 3.8 the density in the beam was estimated to be 5×10^{22} m^{-3}. Assuming a translational

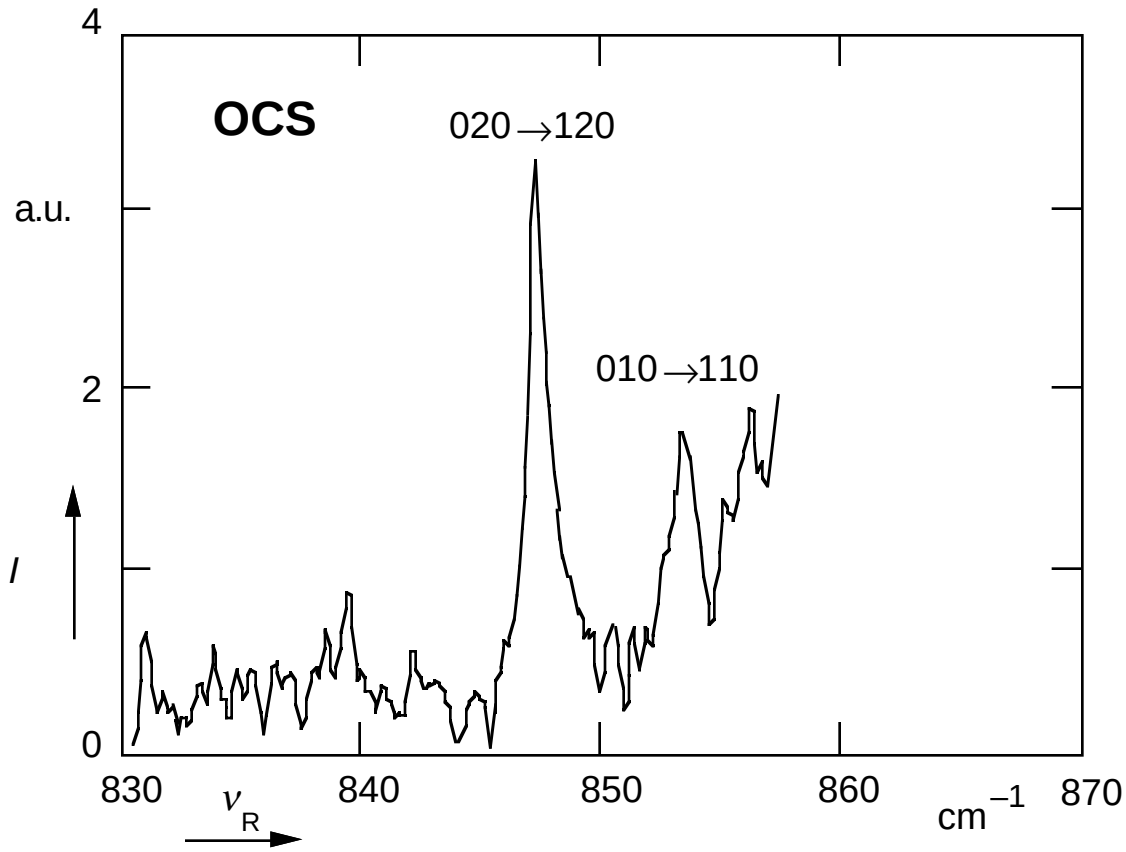

Fig. 6.8. CARS spectrum of OCS in a supersonic beam at 60 ns after 7.2-J/cm^2 infrared excitation, at x/D = 3.8.

temperature of 10 K, one obtains a gas-kinetic mean-free-time between collisions of 40 ns for OCS in the beam at x/D = 3.8. Collisional energy transfer in the beam thus occurs

within 1.5 gas-kinetic collisions, which corresponds to an energy transfer rate of $k_{v_2 \rightarrow v_2}$ = 5.4 μs^{-1} Torr^{-1} at room temperature, in agreement with the lower limit given in chapter 4.

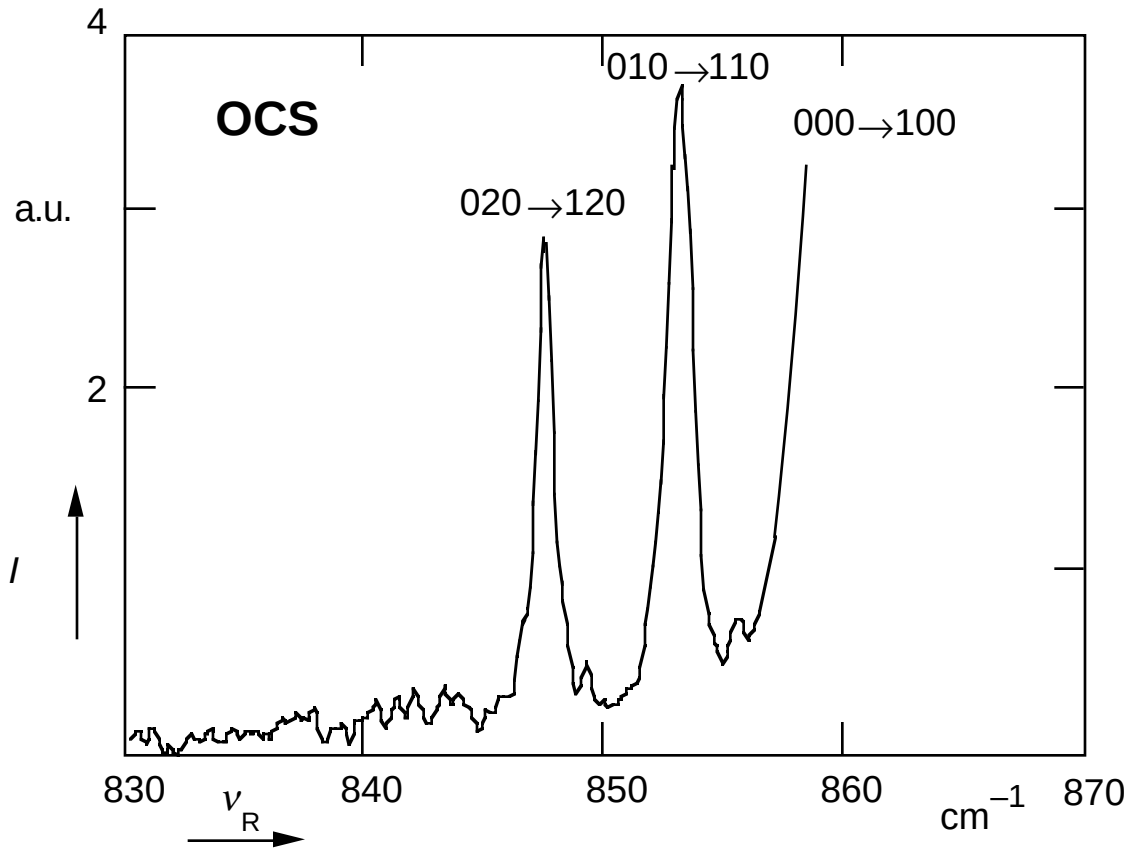

Fig. 6.9. CARS spectrum of OCS in a supersonic beam 150 ns after 7.2 J/cm^2 infrared excitation, at *x/D* = 3.8.

In the bulk excitation was observed for all CO_2 lines between the *P*(10) to *P*(26) lines of the 9.6 μm CO_2 laser branch (see Table 4.2), indicating a broad rotational distribution and rotational hole filling by collisions in the bulk. In the supersonic beam the OCS could only be vibrationally excited by the *P*(22) and *P*(18) lines of the 9.6 μm CO_2

laser branch. This is so because only a few rotational states are populated and there is virtually no collisional broadening. The only mechanism to overcome the frequency mismatch is power broadening. For OCS the Rabi frequency is $\omega_R = 1.3 \times 10^{-5} \sqrt{I}$, with ω_R in cm^{-1} and where I is the peak CO_2 laser intensity in W/cm^2. In this experiment one has $\omega_R = 0.08\ cm^{-1}$, so that indeed only the $P(22)$ and $P(18)$ CO_2 laser lines have a frequency mismatch below the Rabi frequency. These lines pump the P_5 and R_3 transitions of OCS, respectively. Because of the small B-value of OCS, this could not be confirmed by pure rotational CARS measurements.

The OCS measurements in the supersonic beam clearly show the overtone excitation of the OCS by the CO_2 laser. In addition, the measurements clearly show the importance of collisions in the excitation process. Even in the beam collisions do occur, albeit on at a much reduced rate. At $x/D > 3.8$ rotational hole refilling time is longer than the CO_2 pulse duration and thus collisions do not play a role in the excitation process. The supersonic beam thus allows one to distinguish between collisional and collisionless excitation and to determine the collisional relaxation rate of the vibrational excitation in the pumped ν_2 mode.

6.3 IRMPE of SF_6 in the beam

The spontaneous Raman results for SF_6 reported in chapter three show that intramolecular equilibrium is achieved within 20 ns after infrared multiphoton excitation. To study the excitation and equilibration process in more detail one can either improve the time resolution by using shorter pump and probe laser pulses or reduce the pressure to decrease the collisional relaxation rate. The supersonic beam machine and the 8-ns CARS spectrograph both contribute in this respect.

Back in 1982, Alimpiev *et al.* published results of a CARS study of infrared multiphoton excitation of SF_6.[4] The appearence of the hot band of the pumped ν_3 mode due to the CO_2 pumping has been reported. Surprisingly, the anharmonicity shown in the graphs of this paper differs by a factor of two from values published in the literature. Steinfeld *et al.* unsuccessfully tried to repeat the Soviet experiment.[5] The letter showed the depletion of the fundamental peak, but no hot bands associated with the infrared excitation.

This section reports on a study of infrared multiphoton excited SF_6 in a supersonic beam using multiplex CARS. The ν_1 symmetric breathing mode CARS spectrum of SF_6 in the beam at $x/D = 4.3$ is shown in Fig. 6.10. Although in this experiment SF_6 has not been seeded with any noble molecule, the spectrum shows a narrow ν_1 fundamental peak and no trace of excited vibrational states indicating considerable cooling during the supersonic expansion.

Because SF_6 is a strong absorber of the 10*P*20 CO_2 laser line, it can be highly excited at very low fluence. This means it is not necessary to focus the infrared beam and ensures homogeneous excitation of molecules in the probed region. To obtain better time resolution truncated CO_2 laser pulses with a fluence of 0.4 J/cm^2 were used.

As shown in Fig. 6.11, at 50 ns after the CO_2 laser excitation a second peak appears at a shift of 3.0 cm^{-1} from the fundamental peak. This is in good agreement with the hot band of the ν_3 pump mode which has an anharmonicity $x_{13} = -2.99$ cm^{-1}.[1] In addition, by comparing the intensity of the fundamental peak in spectra with and without infrared excitation, one can determine what fraction of molecules remain in the ground state. At a fluence of 0.4 J/cm^2, the decrease in the intensity of the fundamental peak

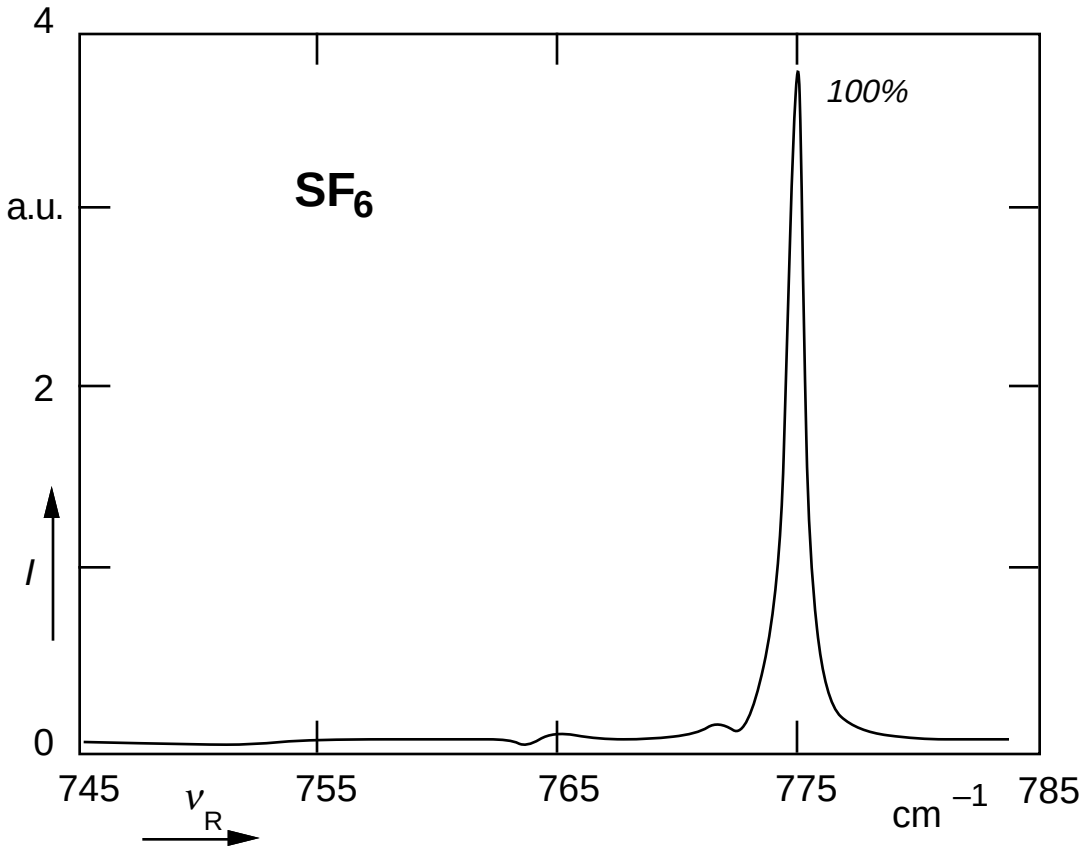

Fig. 6.10. The CARS spectrum of the ν_1 symmetric breathing mode of SF_6 at x/D = 4.3 in the beam.

corresponds to a 30% decrease in population. This decrease is due to the pumping of molecules from the ground state into highly excited states.

At longer delay time the intensities of the hot band peaks increase and the depletion of the ground state becomes more pronounced. Under these conditions (0.4 J/cm^2; x/D = 4.3), however, we did not observe a bump attributable to the quasicontinuum as reported by Alimpiev *et al.*[4] As shown in Fig. 6.12, at 200 ns all peaks including the hot bands

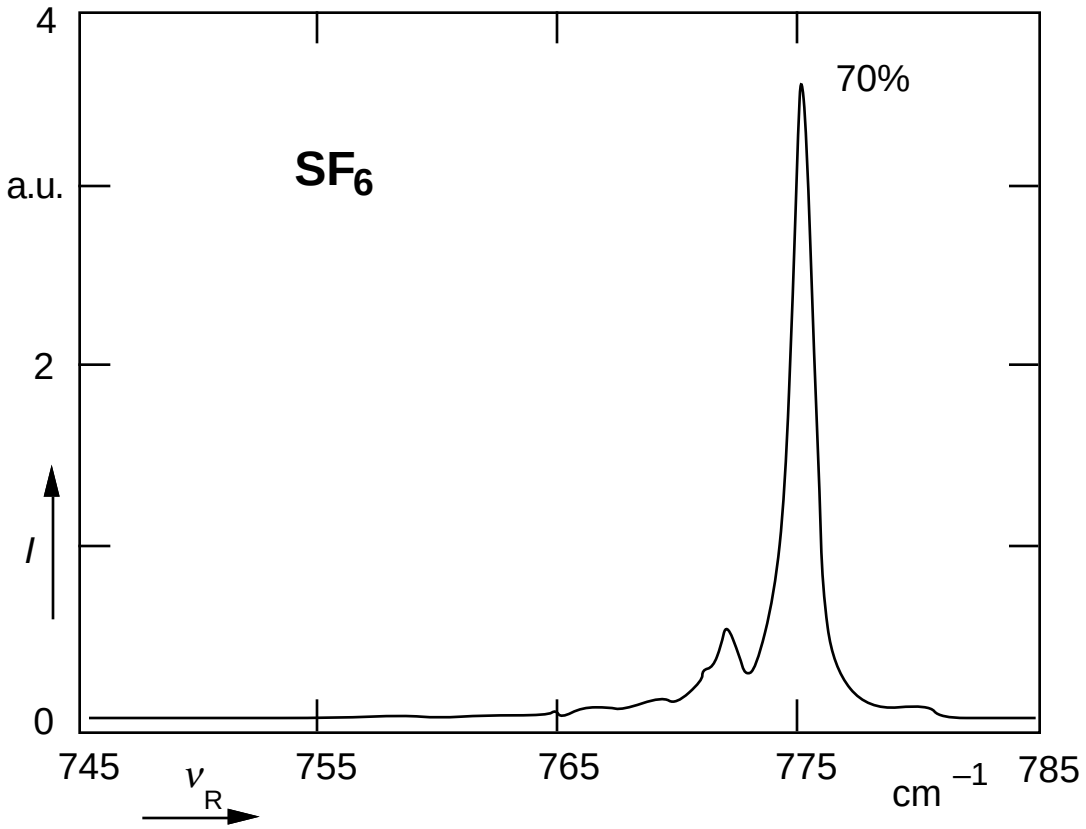

Fig. 6.11. CARS spectrum of SF_6 with $x/D = 4.3$ in the beam at 50 ns after the 0.4 J/cm^2 CO_2 laser excitation. The 70% indicates the percentage of molecules remains in the ground state.

have vanished within the 51-cm^{-1} spectral window monitored. For even longer delays of up to 2 μs, the spectrum remains identical without any peaks reappearing. At still longer delay times the transit time of the molecules through the laser beam interaction region becomes shorter than the delay time and the spectra show unexcited molecules reentering the interaction region.

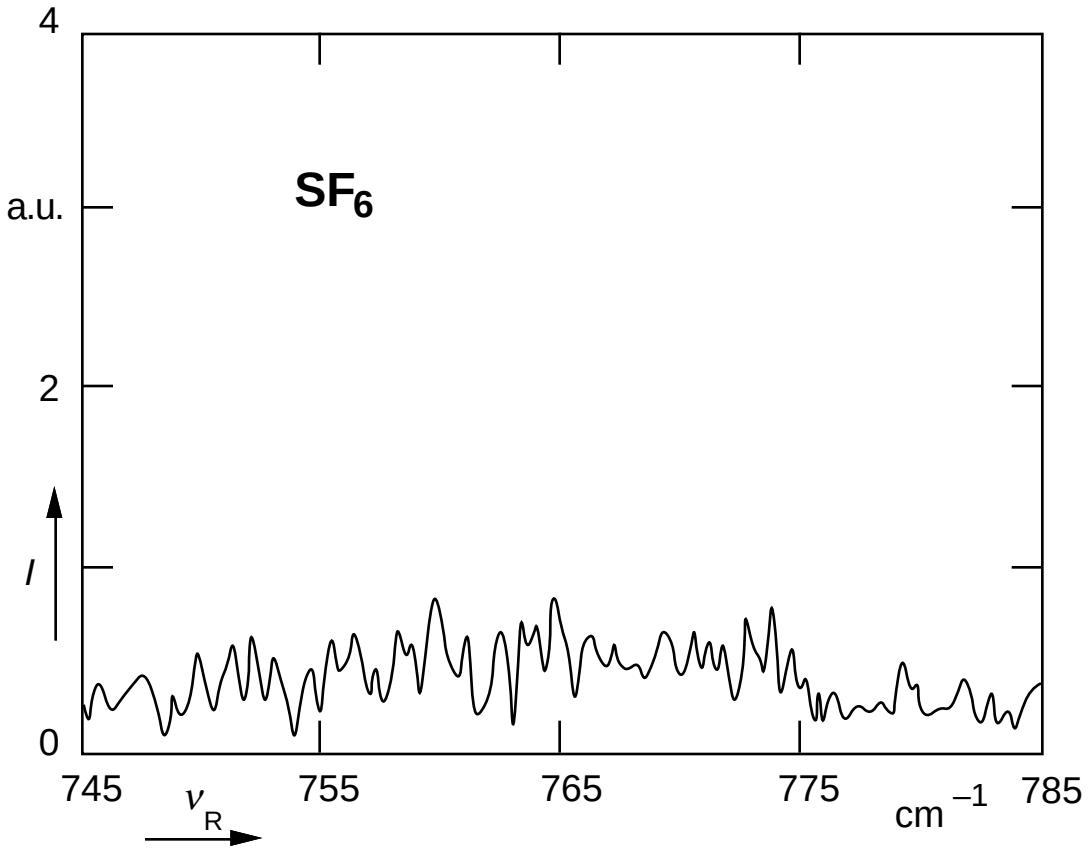

Fig. 6.12. CARS spectrum of SF_6 at x/D = 4.3 in the beam 200 ns after a 0.4-J/cm^2 CO_2 laser excitation.

This is dramatically different from spontaneous Raman or CARS studies of SF_6 in the bulk.[4,6] As reported in Refs. 4 and 6, a two-ensemble distribution was observed right after the CO_2 pulse. The authors attributed the second ('hot') ensemble to the population in the quasicontinuum. For longer delay, it was observed that the two ensembles merge into one and that the system reaches an equilibrium. The main difference between this experiment and the one reported here, is that one was carried out in bulk SF_6 and the other in a supersonic beam. This contributes to different initial distribution over the internal degrees of freedom, and more importantly, different collision rates.

In the beam the collision rate can be controlled by varying the parameter *x/D*. A spectrum obtained at *x/D* = 2.8 and a 50-ns delay is shown in Fig. 6.13. The spectrum is similar to the one obtained at *x/D* = 4.3 (Fig. 6.11), but the infrared excitation is more pronounced and v_3 hot bands up to $v_3 = 4$ are observed due to the increased collision rate.

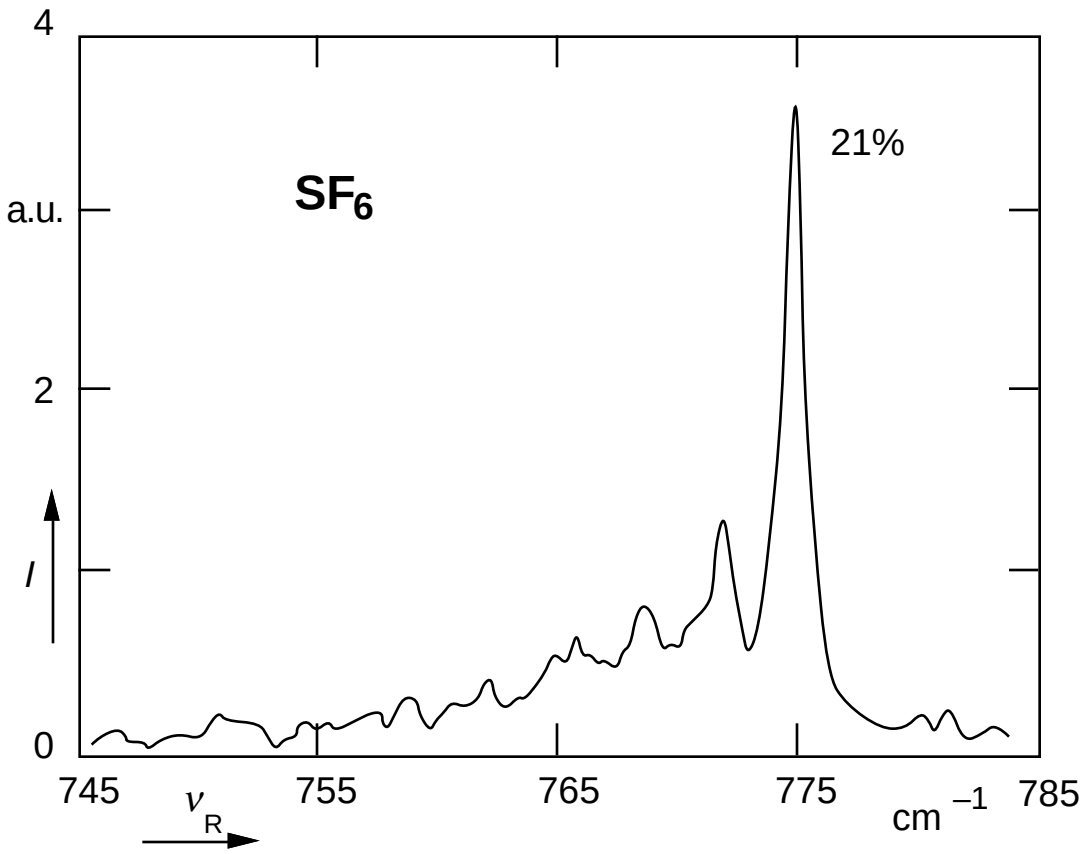

Fig. 6.13. CARS spectrum of SF_6 at *x/D* = 2.8 in the beam 50 ns after a 0.4-J/cm^2 CO_2 laser excitation.

At a delay of 100 ns (see Fig. 6.14), only 10% of the population remains in the ground state, while the peaks in the excited states increase and broaden. They lose their features and become a bump of 15 cm^{-1} width similar to the one reported in Ref. 4.

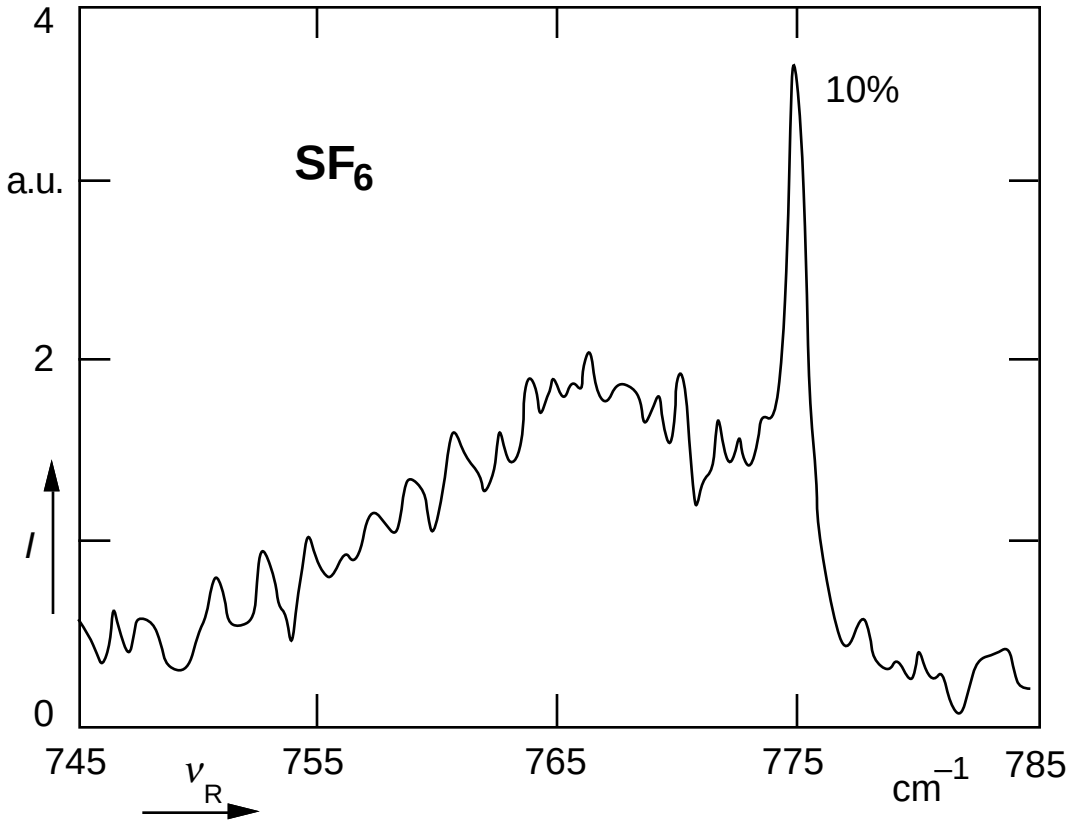

Fig. 6.14. CARS spectrum of SF_6 at $x/D = 2.8$ in the beam 100 ns after a 0.4-J/cm^2 CO_2 laser excitation.

Figure 6.15 shows the spectrum 500 ns after infrared excitation. The ground state population is now reduced to 1%, and the hot bands and fundamental peak are of comparable intensity and become inseparable. In Ref. 4 this was attributed to the merging of the hot and cold ensembles.

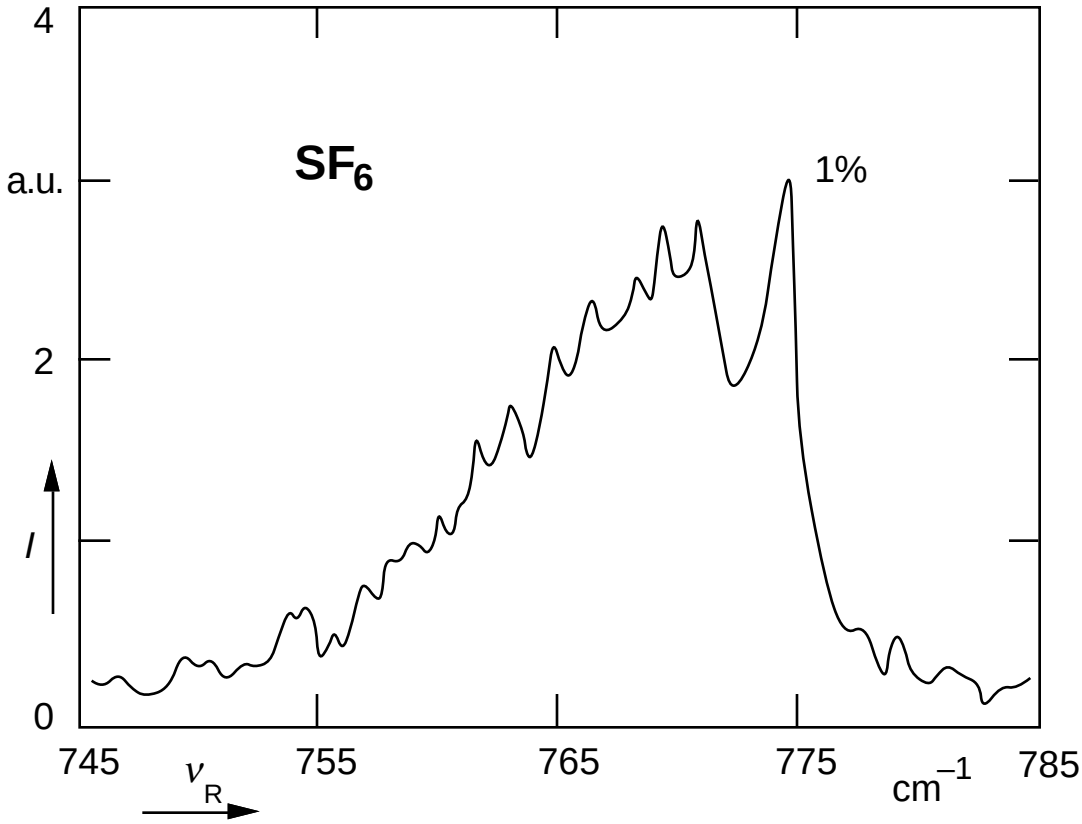

Fig. 6.15. CARS spectrum of SF_6 at x/D = 2.8 in the beam 500 ns after a 0.4-J/cm^2 CO_2 laser excitation. Only 1% of the population remains in the ground state.

These two sets of measurements carried out at x/D = 4.3 and x/D = 2.8 clearly show how collisions can affect the experimental results. Close to the nozzle x/D = 2.8, one observes a reduction of the ground state population and an increase in the hot bands. The hot bands gradually broaden until they become unresolvable and form a bump in agreement with the observations the bulk.

Further away from the nozzle at x/D = 4.3 the collision rate is much reduced. Here one observes ground state depletion and some excitation of the low lying vibrational states. The unresolvable bump seen close to the nozzle is never observed, not even when the fundamental peak is completely depleted. At longer time delays, the entire spectrum

falls below the noise. These observations suggest that the bump reflects a distribution *after* some collisional relaxation has taken place, and that before this relaxation the molecules are pumped to states not visible in the spectrum.

This raises interesting questions about what the real distribution is after excitation. One possibility is that the molecules are pumped to highly excited states beyond the 51 cm^{-1} spectral window monitored in the measurements. This possibility was examined by adjusting the spectrograph and tuning the dye laser to a longer wavelength to monitor the states beyond the normal spectral window. However, no peaks ever showed up in this region.

Another possibility is that the distribution after excitation is so broad that the population difference of adjacent states is small. Since the CARS signal is proportional to the square of the *population difference* of the probed states, a broad spread in distribution strongly diminishes the CARS signal. The broadening of the distribution can have two causes. First, the distribution of the pumped mode may broaden as the excitation increases. Second, as was shown in Fig. 1.2 the density of states ρ increases by six orders of magnitude when SF_6 is pumped from v_3=0 to v_3=10. If all these states become accessible, the population per state decreases dramatically and the CARS signal will disappear entirely.

The appearance of the bump therefore reflects collisional relaxation from highly excited vibrational states to intermediate states. We may then conclude that the determination of a excitation threshold for the onset of energy randomization (‘*stochastization energy’*) based on the appearance of this bump, as has been done previously,[6] is inappropriate. The fact that the bump is not resolvable indicates that hot bands from many modes contribute to it; there is therefore no reason to assume that the bump is due to quasicontinuum states.

6.4 Conclusion

The measurements presented in this chapter clearly show how the combination of the CARS and supersonic beam techniques simplifies the interpretation of measurements of infrared multiphoton excited molecules. In particular the results unambiguously prove that the generally accepted two-ensemble distribution often reported in the literature is not a direct result of the CO_2 laser excitation, but is created by a combination of inter- and intramolecular vibrational relaxation. Additional experiments are necessary to determine what the real vibrational distribution is after infrared multiphoton excitation.

References

1 G. Herzberg, *Infrared and Raman Spectra*, (Van Nostrand, New York, 1945)

2 J. Romanko, T. Feldman, E.J. Stansbury, and A. McKellar, *Canadian J. of Phys.*, **12**, 735 (1954)

3 G. Herzberg, *Electronic Spectra of Polyatomic Molecules*, (Van Nostrand, New York, 1966)

4 S.S. Alimpiev, S.I. Valyanskii, S.M. Nikiforov, V.V. Smirnov, B.G. Sartakov, V.I. Fabelindkii, and A.L. Shtarkov, *JETP Lett.* **35**, 361 (1982)

5 E.L. Schweitzer and J.I. Steinfeld, *Chem. Phys.* **108**, 343 (1986)

6 V.N. Bagratashvili, Yu.G. Vainer, V.S. Doljikov, V.S. Letokhov, A.A. Makarov, L.P. Malyavkin, E.A. Ryabov, and E.G. Sil'kis, *Opt. Lett*. **6**, 148 (1981)

CHAPTER 7

CONCLUSION

7.1 Summary of results

In this thesis, we have presented the results of quantitative studies of the infrared multiphoton excitation and relaxation of a number of polyatomic molecules. The results are briefly summarized below.

Using time-resolved spontaneous Raman spectroscopy, we have obtained information on the intramolecular energy distribution of energy over the different modes after infrared excitation. For SF_6, equilibration of energy from the pump mode to other vibrational modes occurs within the time resolution of the experiment. In contrast, for smaller molecules such as CF_2Cl_2, a nonthermal energy distribution is observed after excitation. This difference in behavior may be caused by the difference in density of vibrational states and intermode coupling, or by the symmetry of the molecule.

Because of the much higher spectral resolution, time-resolved multiplex CARS measurements make it possible to perform state-specific studies of the vibrational and rotational distribution, and provide additional information on the excitation dynamics and relaxation processes. From the CARS measurements on bulk OCS and SO_2, we obtained

information on the mode pumped by CO_2 laser, and obtained values for the anharmonicities, and the energy transfer rates between modes.

The pulsed supersonic molecular beam apparatus presented in chapter 5 opens up new possibilities in the field of infrared multiphoton excitation. Combined with the state-specific CARS technique, the collisionless and internally cooled molecules in the beam provide further insights into the excitation process. The overtone excitation of OCS by a CO_2 laser was verified, and the evolution of the overtone population into a thermal distribution was studied, providing new values for the intramode relaxation rate.

The study of SF_6 in the supersonic beam provided a new interpretation of the energy distribution in SF_6 after infrared multiphoton excitation. It was shown that the generally accepted two-ensemble population distribution[1,2] after infrared multiphoton excitation is actually a distribution that has already undergone considerable collisional relaxation. What the original distribution before collisional relaxation really is remains to be determined.

7.2 Suggestions for further research

The high excitation end of the energy distribution of infrared multiphoton excited molecules (before collisional relaxation) still needs to be investigated. The multiplex CARS technique presented in this thesis clearly is a powerful tool for studying the low-lying vibrational energy levels as well as the rotational distributions. However, because the CARS signal is proportional to the square of the *population difference per state*, CARS is not well suited to study molecules at the high excitation end. Spontaneous Raman spectroscopy does not suffer from this difficulty but has a very small signal level and a low spectral resolution. Another nonlinear optical technique, multiphoton ionization,[3] has a sensitivity and spectral resolution comparable to or even exceeding that of CARS, and is

directly proportional to the population. Therefore, multiphoton ionization may be a suitable technique for complementing the CARS studies presented in this thesis,[4] even though the assignment and interpretation of multiphoton ionization spectra is difficult in general.

Only very few spectra of highly vibrationally excited molecules, such as the ones shown in chapters 4 and 6, have been reported in the literature. With the setup used in this thesis one could obtain additional information on the $v_2 = 3$ and $v_2 = 4$ states of OCS, on the $v_2=4$ level splitting observed in OCS, and on the excited states of SO_2. Additionally one could study the dynamics of the energy transfer between Fermi-resonance states, for example the $v_2 = 4$ and $v_3 = 1$ states of OCS.

References

1 V.N. Bagratashvili, Yu.G. Vainer, V.S. Doljikov, V.S. Letokhov, A.A. Makarov, L.P. Malyavkin, E.A. Ryabov, and E.G. Sil'kis, *Opt. Lett*. **6**, 148 (1981)

2 S.S. Alimpiev, S.I. Valyanskii, S.M. Nikiforov, V.V. Smirnov, B.G. Sartakov, V.I. Fabelindkii, and A.L. Shtarkov, *JETP Lett.* **35**, 361 (1982)

3 G.S. Hurst, M.G. Payne, S.D. Kramer, and J.P. Young, *Rev. Modern Phys.*, **51**, 767 (1979)

4 Jian Wei and Mary J. Shultz, *Multiphoton Ionization Studies of Infrared Multiphoton Excited Ammonia*, in preparation.

APPENDIX A

PUBLICATIONS

1. "Time-resolved spontaneous Raman spectroscopy of infrared-multiphoton-excited SF_6,"

   Jyhpyng Wang, Kuei-Hsien Chen, and Eric Mazur, *Phys. Rev. A* **34**, 3892 (1986)

2. "Raman spectroscopy of infrared multiphoton excited molecules"

   Kuei-Hsien Chen, Jyhpyng Wang, and Eric Mazur, Technical Digest, *Int. Quantum Electronics Conf.*, San Francisco, June 1986

3. "The interaction of infrared radiation with isolated molecules: intramolecular nonequilibrium,"

   Eric Mazur, Kuei-Hsien Chen, and Jyhpyng Wang, *Proc. Int. Conf. on Lasers '86*, Orlando, November 1986, p. 359

4. "Non-thermal intramolecular vibrational energy distribution in infrared-multiphoton-excited CF_2Cl_2,"

   Kuei-Hsien Chen, Jyhpyng Wang, and Eric Mazur, *Phys. Rev. Lett*, **59**, 24 (1987) 2728

5. "Highly nonthermal intramolecular energy distribution in isolated infrared multiphoton excited CF_2Cl_2 molecules,"

   Eric Mazur, Kuei-Hsien Chen, and Jyhpyng Wang, *Laser Spectroscopy*, Ed. S. Svanberg (Springer, 1987)

6. "Raman spectroscopy of infrared multiphoton excited molecules,"
   Jyhpyng Wang, Kuei-Hsien Chen, and Eric Mazur, *Laser Chem.*, **8**, 97 (1988)
7. "Energy localization in infrared multiphoton excited CF_2Cl_2 studied by time resolved Raman spectroscopy,"
   Jyhpyng Wang, Kuei-Hsien Chen, and Eric Mazur, *Int. Conf. Quantum Electronics 1988*, Tokyo Japan.
8. "Multiplex coherent anti-Stokes Raman spectroscopy study of infrared-multiphoton-excited OCS,"
   Kuei-Hsien Chen, Cheng-Zai Lü, Luis Avilés , Eric Mazur, Nicolaas Bloembergen, and Mary J. Shultz, *J. Chem. Phys*. **91**, 1462 (1989)
9. "Multiplex CARS study of infrared-multiphoton-excited OCS,"
   Kuei-Hsien Chen, Cheng-Zai Lü, Eric Mazur, Nicolaas Bloembergen, and Mary J. Shultz,
   Proceeding of the Ninth International Conference on Laser Spectroscopy. 1989.

PAPERS PRESENTED

1. "Thermal and nonthermal intramolecular energy distributions in isolated infrared multiphoton excited molecules,"
   APS March Meeting 1987, New York.
2. "Raman studies of infrared-multiphoton-excited-molecules,"
   Gordon Conference Multiphoton Processes, poster session, New London, New Hampshire, June, 1988.
3. "Multiplex CARS study of infrared-multiphoton-excited OCS,"
   Institute of Atomic and Molecular Science, Taiwan, February 1989.
4. "Multiplex CARS study of infrared-multiphoton-excited OCS,"
   invited poster for the Ninth International Conference on Laser Spectroscopy, New Hampshire, June, 1989.
5. "Coherent anti-Stokes Raman spectroscopy study of infrared-multiphoton-excited Molecules,"
   General Electric Research Center, Schenectady, New York, August 8, 1989.

APPENDIX B

ELECTRONIC CONTROLLER FOR A PULSED SUPERSONIC MOLECULAR BEAM

The nozzle used in the pulsed supersonic beam reported in this thesis is driven by a electromagnetic coil as shown in Fig. 5.4. By opening the nozzle for 0.1 to 1 ms at 10 Hz, one needs less pumping capacity than for a cw nozzle. This appendix explains the electronic circuit that controls the pulsed nozzle.

A high voltage regulator LM317 HVK is used to provide a variable voltage source of 20 to 40 V. Because the electromagnetic coil in the nozzle has a very low impedance (4 Ω), it can only be driven by low output-impedance devices such as a model no. 2N 6284 Darlington power transistor.

The trigger signal is handled by a separate power circuit (the second LM317 HVK voltage regulator) to avoid noise pick-up from the output. A third regulator (LM317T) is used to lower the voltage from 40 to the 5 V TTL standard.

An external trigger pulse goes into a monostable multivibrator (96LS02), and produces a pulse of variable width t_w after a variable delay t_d with a 5V amplitude as shown in the diagram below.

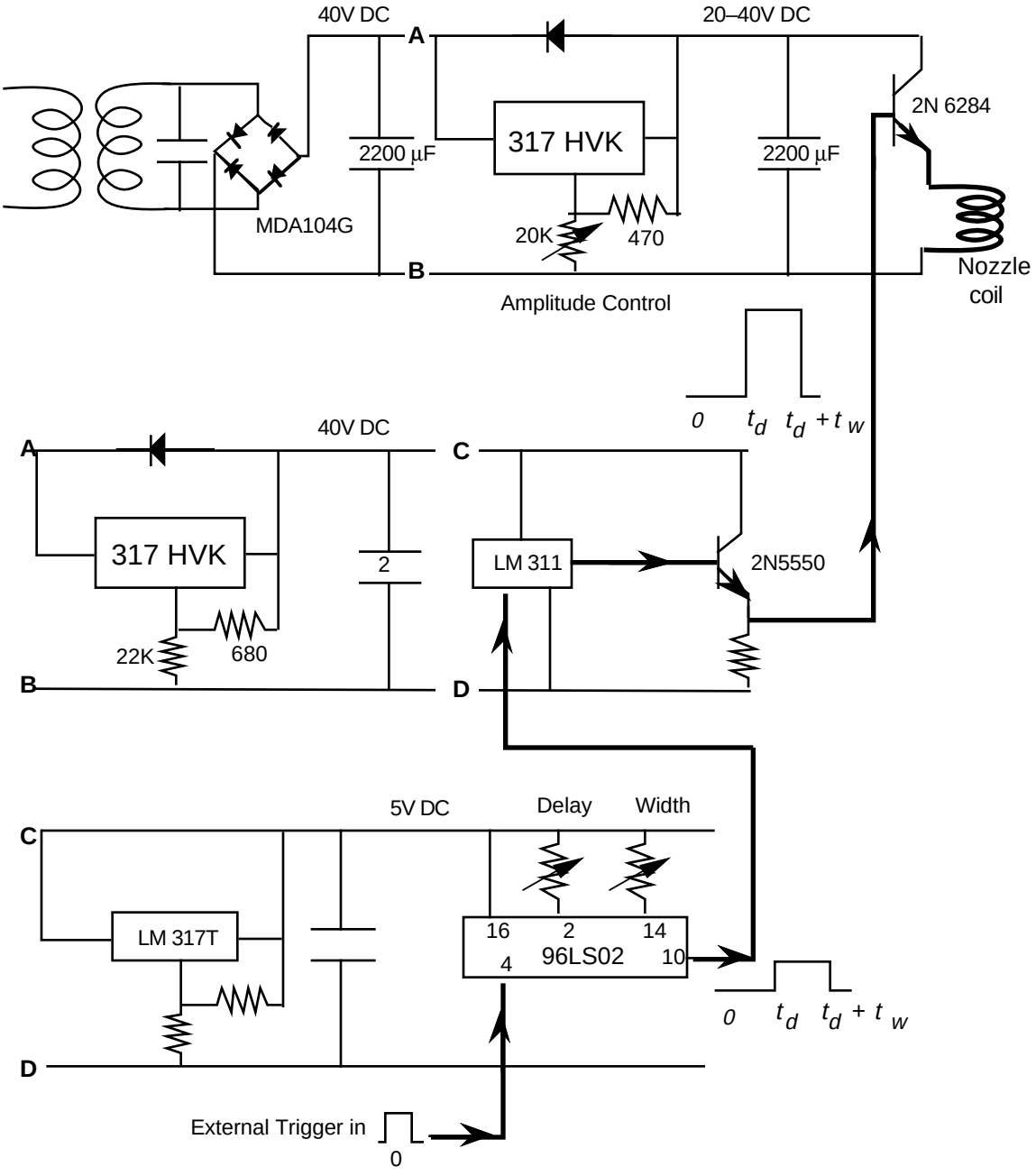

Fig. B.1. Schematic of the supersonic nozzle controller. The path of the trigger signal is indicated by the thick lines.

The pulse is then sent into an LM311 comparator, and amplified to 40 V while retaining the same time profile. Finally, the 40 V pulse goes into a Darlington power transistor (2N6284) which has a very low output impedance and is capable of driving the low impedance magnetic coil.